Fifth National Image-Guided Therapy Workshop

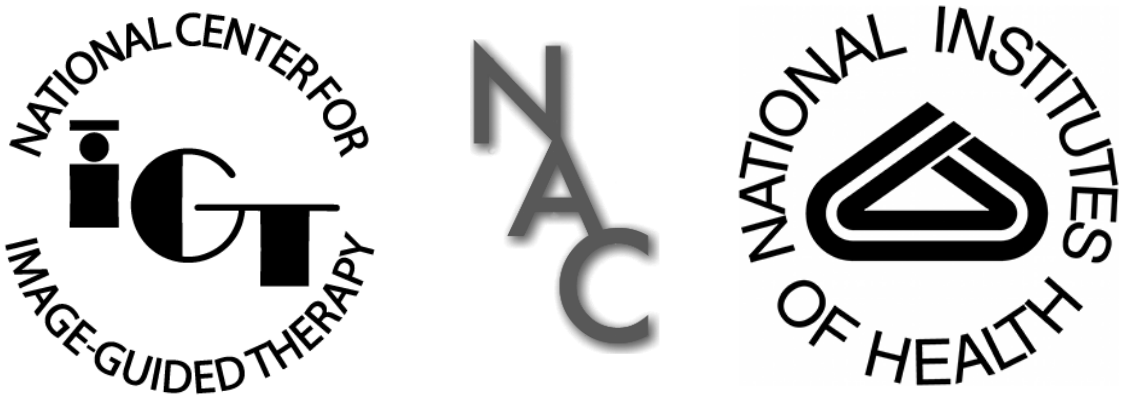

September 21, 2012
Boston, MA

www.ncigt.org

Symposium Chairs
Ferenc Jolesz, MD
Clare Tempany, MD

Program Chair
Tina Kapur, PhD

Table of Contents

Welcome

Welcome to the Fifth Image-Guided Therapy workshop sponsored by the National Center for Image Guided Therapy (NCIGT, P41EB015898), the Neuroimage Analysis Center (NAC, P41EB015902) and the National Institutes of Health (NIH). The overall goal of this workshop series is to assess the current needs and opportunities in the field of image-guided therapy and the role of NCIGT as a national center serving the greater IGT community. The focus for this year's workshop is Molecular and Ultrasound Image Guided Therapy.

The program for this workshop includes a single track of scientific talks, as well as a poster session. The talks are divided into sessions that focus on ultrasound guided therapy, histopathology and validation, and molecular imaging guided therapy.

Similar to previous workshops in this series, we are honored to have in attendance our colleagues from academia, industry, as well as the National Institutes of Health. We hope that you continue to contribute to the success of this workshop by your participation.

Sincerely,
Members of the Program and Organizing Committees

Program Committee

Ferenc Jolesz, MD, Chair

Clare Tempany, MD, Chair

Tina Kapur, PhD, Program Chair

Keyvan Farahani, PhD

Ron Kikinis, MD

Alexandra Golby, MD

William Wells, PhD

Nobuhiko Hata, PhD

Organizing Committee

Ferenc Jolesz, MD

Clare Tempany, MD

Tina Kapur, PhD

Danielle Chamberlain, BS, RT

Danielle Klette

Patti Goldberger, MBA

Marianna Jakab, MS

Zion Tse, PhD

Jan Egger, PhD, PhD

Neha Agrawal, MBBS

Guillaume Pernelle, BS

Oral Program

8:00 AM	**Breakfast**		
8:30-10:00 AM **Session I** **Ultrasound Guided Therapy**	8:30	4D Echocardiography - Derived LV Strain For Therapy Guidance And Response Assessment	**Jim Duncan, PhD** Yale University
	8:45	Slicer IGT: An Open Source Platform For Image-Guided Therapy	**Gabor Fichtinger, PhD** Queens University
	9:00	Understanding Tumor Micro-Environments: Targeting Biopsies	**Stephen Aylward, PhD** Kitware Inc
	9:15	Intra-Operative 3D Visualization & Needle Guidance For Live Ultrasound & Registered Pre-Operative Scans	**Andrei State, MSCS** InnerOptic Inc.
	9:30	Mixed Reality Guidance Of Intra Cardiac Beating Heart Surgery For Valve Repair	**Terry Peters, PhD** Robarts Research Institute
	9:45	Intraprocedure Acoustic Radiation Force Impulse Imaging Of Radiofrequency Ablation Lesions: Initial Clinical Results	**Tristram Bahnson, MD** Duke University
10:00-10:30 AM	**Break**		
10:30 AM-12:00 PM **Session II** **Histopathology Based Validation**	10:30	A Biomechanical Model-Based Approach To Correlative Pathology For Image Validation	**Kristy Brock, PhD** University of Toronto
	10:45	Mass Spectrometry Imaging Applications For Surgical Pathology	**Nathalie Agar, PhD** Harvard Medical School
	11:00	Imaging Tumor Margins With A Mobile Large Area Confocal Scanner: Initial Testing In The Pathology Department	**Sanjee Abeytunge, MS** Memorial Sloan-Kettering
	11:15	Imaging Of Vessel Patency In Thiel Embalmed Liver	**Matthew Pendleton, BSc** University of Dundee
	11:30	Adjustable Sleeve Template Assembly Device For Joint MR/US-Guided Diagnosis And Treatment Of Prostate Cancer: Initial Design And Feasibility Evaluation	**Andriy Fedorov, PhD** Harvard Medical School
	11:45	Validation Of THz Imaging For Burn Surgery Using MR	**Neha Bajwa, MS** UCLA
12:00-1:30 PM	**Lunch And Poster Session**		
1:30-2:30 PM **Session III** **Molecular Imaging Guided Therapy**	1:30	Clinical Translated Silica Nanoparticles As PET-Optical Probes For Image Guided Interventions	**Michelle Bradbury, MD, PhD** Memorial Sloan-Kettering
	1:45	Nanocolloids For Integrating Imaging Characterization With Targeted Therapy	**Gregory M. Lanza, MD** PhD, Washington University
	2:00	Nanotechnologies For Image-Guided Therapies	**Sri Sridhar, PhD** Northeastern University
	2:15	Feasibility Of Using Simultaneous PET/MR In The Evaluation Of Cervical Carcinoma	**Perry Grigsby, MD** Washington University
2:30-3:00 PM	**Break**		
3:00-5:15 PM **Session IV** **Mixed Topics**	3:00	Ultrasound-Guided Fast Robotic Catheters For Beating Heart Surgery	**Samuel Kesner, PhD** Harvard University
	3:15	MRIgRT Facility Design: Magnetic Field Decoupling Of An MRI-On-Rails From A Linear Accelerator	**Teo Stanescu, PhD** Princess Margaret Cancer Ctr
	3:30	Abdominal Surface Registration In Percutaneous Image-Guided Therapy	**James Stefansic, PhD** Pathfinder Therapeutics, Inc.
	3:45	New Developments In Gradient-Based Tracking For MRI	**Erez Nevo, MD, DSc** Robin Medical, Inc.
	4:00	Tracking Of 19F Labeled Interventional Devices By Means Of 3D Golden Angle Radial Sampling	**Tobias Hahn, MSc** ETH Zurich
	4:15	3D Slicer Based Real Time Registration For Planning Image Guided Laser Induced Thermal Therapy Interventions	**Erol Yeniaras, PhD** MD Anderson, U of Texas
	4:30	Deformation Compensation Strategies for Image Guided Surgery Using Sparse Data	**Michael Miga, PhD** Vanderbilt University
	4:45	MRI-Guided Fully Actuated Robotic Prostate Biopsy And Brachytherapy	**Hao Su, MS** Worcester Polytechnic Institute
	5:00	Patient Image Viewing For Facilitating Interventional Device Placement	**Andrew Holbrook, PhD** Stanford University
5:30 PM	**Shuttle Pick up at Conference Center, Destination Copley Marriott**		

Poster Program
12-1:30PM

GROUP A: INTERVENTIONAL CT/ULTRASOUND

1. Image-Guided Robotically-Steerable CT-Compatible Instrument for Multi-Adjacent-Point Targeting. Meysam Torabi, Andrew Harris, Alex Golden, Rajiv Gupta and Conor Walsh

2. Enhanced 3D Ultrasound Visualization for Guiding Beating Heart Procedures. Laura Brattain, Nikolay Vasilyev, Pedro Del Nido and Robert Howe

3. Ultrasound Volume Reconstruction: Open-Source Implementation with Hole Filling Functionality. Thomas Vaughan, Andras Lasso and Gabor Fichtinger

GROUP B: INTERVENTIONAL MRI

4. Interventional Magnetic Resonance Imaging with an In-room Interactive Touch Device. Martin Alexander Rube, Benjamin F. Cox, Andrew B. Holbrook, Leon Melzer and Andreas Melzer

5. Closed-Loop Commutator Control of an MRI-Powered Actuator. Christos Bergeles, Panagiotis Vartholomeos, Lei Qin and Pierre Dupont.

6. Magnetic Resonance Imaging for Episcleral Plaque Brachytherapy. Jacqueline Esthappan, Yanle Hu, Carol Bertelsman, Jose Garcia-Ramirez and Perry Grigsby

7. Compact, Patient-Mounted MRI-guided Robot for Accurate Positioning of Multiple Cryoablation Probes. Faye Wu, Meysam Torabi, Alex Golden, Michael Werner, Atsushi Yamada, Noby Hata, Hao Su, Greg Cole, Gerg Fischer, Dan Frey, Conor Walsh and Kemal Tuncali

8. 4D MRI for MRI-guided liver stereotactic body radiation therapy. Teo Stanescu, Tony Tadic and David Jaffray

9. Concurrent 12-Lead ECG & MRI Study of Acute Left Ventricular Ischemia Progressing to Death . Zion Tse, Charles Dumoulin, Ronald Watkins, Kim Butts-Pauly, Israel Byrd, Jeffrey Schweitzer, Raymond Kwong, Gregory Michaud, William Stevenson, Ferenc Jolesz and Ehud Schmidt

10. Swine Model Validation of Multimodality Cardiac Electrophysiology with an MRI-compatible Voltage-based Electroanatomic Mapping System. Zion Tse, Charles Dumoulin, Israel Byrd, Jeffrey Schweitzer, Ronald Watkins, Kim Butts-Pauly, Raymond Kwong, Gregory Michaud, William Stevenson, Ferenc Jolesz and Ehud Schmidt

11. A Performance Evaluation Study of a Motorized Needle Guidance Template for MRI-guided Targeted Prostate Biopsy. Sang-Eun Song, Junichi Tokuda, Kemal Tuncali, Clare Tempany and Nobuhiko Hata

12. Evaluation of Commonly Used Devices in the MR Environment. Ramon Martin, Karan Madan, Luigi Nascimben, Daniel Kacher, Chang-Sheng Mei, Lawrence Panych

13. Catheter Digitization on T2 MR for Interstitial Gynecologic Brachytherapy using a Hybrid MRI/CT Technique . Antonio Damato, Robert Cormack, Tina Kapur, Ehud Schmidt and Akila Viswanathan

GROUP C: MEDICAL IMAGING COMPUTING

14. Development of Real-time Intraoperative Image Fusion for Laparoscopic Surgery in Pediatrics. Xin Kang, Mahdi Azizian, Emmanuel Wilson, Timothy Kane, Craig Peters and Raj Shekhar

15. Pituitary Adenoma Segmentation Using the Medical Image Computing Platform 3D Slicer. Jan Egger, Tina Kapur, Christopher Nimsky and Ron Kikinis

16. Capability of the Medical Image Computing Platform 3D Slicer for Glioblastoma Multiforme Segmentation in Magnetic Resonance Imaging (MRI) Data. Jan Egger, Tina Kapur, Andriy Fedorov, Steve Pieper, James Miller, Harini Veeraraghavan, Bernd Freisleben, Alexandra Golby, Christopher Nimsky and Ron Kikinis

17. Intraoperative Endoscoping Margin Evaluation for Prostate Resection Robotic Surgery. Alex Hartov, John Seigne, John Heaney, Andrea Borsic, Yuqing Wan and Ryan Halter

18. Probabilistic deformation atlases for atlas-based registration and segmentation. John Onofrey, Lawrence Staib and Xenophon Papademetris

19. Image-based Tracking of Deflected Needle for Complex MR Images in MRI-guided Percutaneous Interventions . Atsushi Yamada, Junichi Tokuda and Nobuhiko Hata

20. Prostate Central Gland Segmentation Using a Spherical Template Driven Graph Approach. Jan Egger, Tobias Penzkofer, Tina Kapur and Clare Tempany

21. Graph-Based Vertebra Segmentation Using a Cubic Template. Robert Schwarzenberg, Tina Kapur, William Wells, Christopher Nimsky, Bernd Freisleben and Jan Egger

22. Segmentation of Pelvic Structures for Gynecologic Brachytherapy. Jan Egger, Neha Agrawal, Tyler Blevins, Nabgha Farhat, Guillaume Pernelle, Xiaojun Chen, Yi Gao, William Wells, Tobias Penzkofer, Tina Kapur and Akila Viswanathan

23. Linear Dynamic System Analysis for Segmenting Breast Carcinomas from DCE-MRI Jayender Jagadeesan, Eva Gombos, Tyler Blevins, Sona Chikarmane, Neha Agrawal and Ferenc Jolesz

24. Optimal Trajectory Selection for Segmenting Breast Carcinomas from DCE-MRI using A Statistical Learning Algorithm Jayender Jagadeesan, Vivek Narayan, Sona Chikarmane, Kirby Vosburgh, Ferenc Jolesz and Eva Gombos

25. Needle Labeling for Interstitial Gynecological Brachytherapy. Yi Gao, Nabgha Farhat, Neha Agrawal, Guillaume Pernelle, Xiaojun Chen, Jan Egger, Tyler Blevins, Sylvain Bouix, Allen Tannenbaum, William Wells, Ron Kikinis, Ehud Schmidt, Akila Viswanathan and Tina Kapur

26. A Software Prototype for Real-time Ablation Zone Planning Using Distance Transformation Calculated Isosurfaces. Jan Egger, Tina Kapur, Philipp Bruners, Tobias Penzkofer

27. Subminute nonrigid multimodality image registration for image-guided therapies. William Plishker, Wen Li, Nabile Safdar, Nobuhiko Hata and Raj Shekhar

28. A Novel Iterative Approach for Accounting for Non-Rigid Deformations in Image Guided Liver Surgery Using Sparse Surface Data. D. Caleb Rucker, Yifei Wu, Thomas S. Pheiffer, Amber L. Simpson, Michael I. Miga

GROUP D: IMAGING TECHNIQUES & OTHERS

29. Positive Contrast Ultrashort TE imaging with Ferumoxytol Contrast Agent. Codi Gharagouzloo, Saaussan Madi, Mukesh Harisinghani and Srinvas Sridhar

30. Interactive Real Time Inductively Coupled Catheter Coil Tracking Using a Transmit Array System. Ugur Yilmaz, Li Pan and Ergin Atalar

31. Quantitative Imaging to Establish Distribution Parameters of Timed Release of Drug Eluting Nanoparticles from Implantable Devices for Image Guided Chemobrachytherapy Rajiv Kumar, Stacey Markovic, Tej Jadhav, Mark Niedre, Paul Nguyen, Anthony D'Amico, Mike Makrigiorgos, Srinivas Sridhar and Robert Cormack

Hold the Date for Next Year

NCIGT/NIH 2013 Workshop
SMIT 25th Anniversary Meeting
Children's National Hospital Tour

21-23 March 2013 | Washington, DC, USA

You are cordially invited to the Sixth Image-Guided Therapy workshop organized by the National Center for Image Guided Therapy (NCIGT) at Brigham and Women's Hospital and the National Institutes of Health. This workshop will run concurrently with the 25th Anniversary meeting of the Society for Medical Innovation and Technology. This 3-day event will conclude with a visit to Children's National Medical Center for a special session on pediatrics, followed by a tour of the newly renovated operating rooms and the Sheikh Zayed Institute for Pediatric Surgical Innovation.

Workshop/Meeting Chairs

Ferenc Jolesz, MD, Brigham and Women's Hospital & Harvard Medical School
Clare Tempany, MD, Brigham and Women's Hospital & Harvard Medical School
Kevin Cleary, PhD, Children's National Medical Center
Andreas Melzer, MD, University of Dundee
Michael Marohn, MD, Johns Hopkins Medical Institutions

Program Chairs

Tina Kapur, PhD, Brigham and Women's Hospital & Harvard Medical School
Raj Shekhar, PhD, Children's National Medical Center

National Center for Image-Guided Therapy
Society for Medical Innovation and Technology

The call for abstracts will open on 15 November 2012 & abstracts will be due by 15 December 2012.
For further details see http://www.ncigt.org/pages/IGT_Workshop_2013

Select Oral Abstracts

Mixed reality guidance of intra-cardiac beating heart surgery for valve repair

John Moore[1], Michael Chu[1,2], Daniel Bainbridge[2,3], David McCarty[4], Gerard Guiraudon[2], Chris Wedlake[1], Maria Currie[1,2], Richard Daly[6], Bob Kiaii[1,2], Terry M. Peters[1,5],

Purpose: Recent developments in cardiac surgery have made it possible to repair the mitral valve without the need for open heart surgery using cardiopulmonary bypass[i]. However, since these technologies are limited to imaging modalities such as echocardiography (ultrasound) and fluoroscopy, it can be quite difficult for cardiac surgeons and cardiographers to safely perform repairs. We have developed and validated a mixed reality guidance platform (Figure 1) to assist with beating heart mitral valve repair.

Methods: In two animal studies, a total of six cardiac surgeons compared our mixed reality platform to standard of care echocardiography for navigating the NeoChord device[i] from the apex of the left ventricle to the mitral valve apparatus.

Results: Tracked tool path results demonstrate three-fold improved accuracy, five-fold shorter navigation times and overall improved safety with mixed reality image guidance.

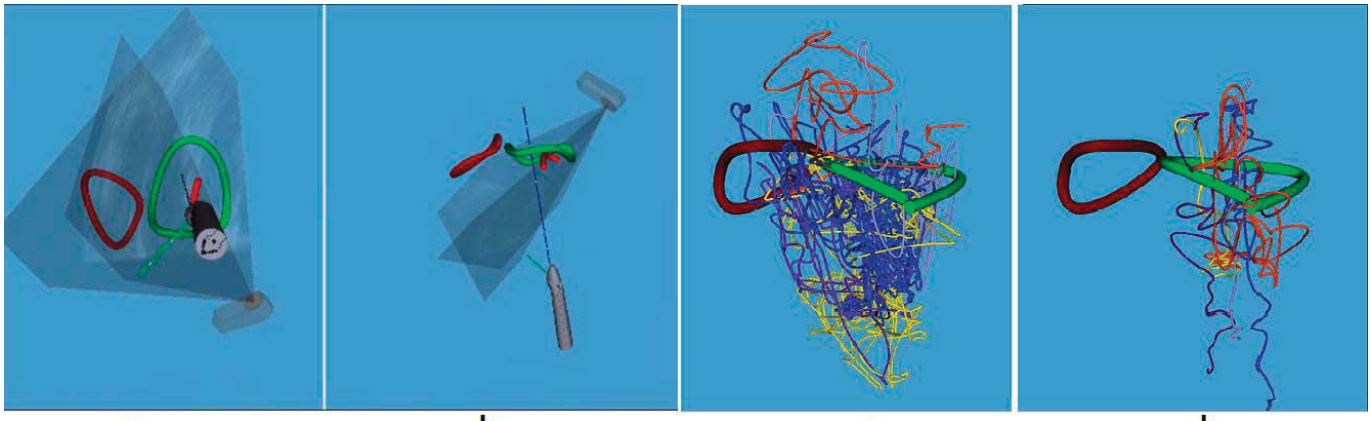

Figure 1, data from our first study. (a) and (b): mixed reality platform consisting of virtual representations of tracked tool, transducer and valve annuli; (c) tool path data from 5 surgeons using echo navigation; (d) the same surgeons using mixed reality navigation

Conclusions: Mixed reality image guidance can make intra-cardiac procedures considerably easier and safer. Current clinical practice relies on experienced proctors to ensure patient safety: AR guidance can greatly facilitate expanding the use of the NeoChord technology to a broader community of surgeons.

[1] Robarts Research Institute;, [2] Division of Cardiac Surgery, Department of Surgery, [3] Department of Anaesthesia, [4] Division of Cardiology, Department of Medicine, [5] Department of Medical Imaging, Western University, London, Ontario, Canada, [6] Mayo Clinic, Rochester, MN, USA. Funding for this work was provided by Canadian Foundation for Innovation (20994), the Ontario Research Fund (RE-02-038) and the Canadian Institutes of Health Research (179298). We received additional funding from NeoChord Inc to support the animal laboratory research.

[i] NeoChord: www.neochord.com; MitraClip: www.abbottvascular.com/int/mitraclip.html

Intraprocedure Acoustic Radiation Force Impulse Imaging of Radiofrequency Ablation Lesions: Initial Clinical Results

Tristram Bahnson, MD,[1,2] Stephanie Eyerly, MS,[3] Joshua Doherty, BS,[3] Douglas Dumont, PhD,[3] Gregg Trahey, PhD,[3,4] Patrick Wolf, PhD,[3]

[1]Center for Atrial Fibrillation, Duke Heart Center, Duke University Medical Center (DUMC); [2]Clinical Cardiac Electrophysiology, Division of Cardiovascular Medicine, DUMC [3]Dept of Biomedical Engineering, Duke University; [4]Dept of Radiology, DUMC

Purpose: We have previously shown *in vitro*[1] and *in vivo* in animal subjects[2] that acoustic radiation force impulse (ARFI) imaging can visualize myocardial stiffness changes induced by thermal-heating during radiofrequency ablation (RFA). This preliminary clinical study was conducted to determine if intracardiac echo (ICE) based 2D ARFI imaging could provide intraprocedure visualization of RFA treatment sites in human subjects receiving transcatheter ablation (TCA) for the treatment of atrial fibrillation (AF).

Methods: Three TCA patients were consented and underwent a double transseptal puncture for left atrial (LA) access. A software modified S2000 (Siemens Healthcare; Issaquah, WA) ultrasound scanner and 8 French AcuNav ICE probe (Biosense Webster; Diamond Bar, CA) were used to acquire diastolic-gated ARFI images before and after RFA delivery. The ICE position was maintained between acquisitions, and screen shots of the ablation catheter contact (ACC) were acquired to verify the intended RFA location. The clinician was blinded to the ARFI image results, and the ARFI images were processed off-line.

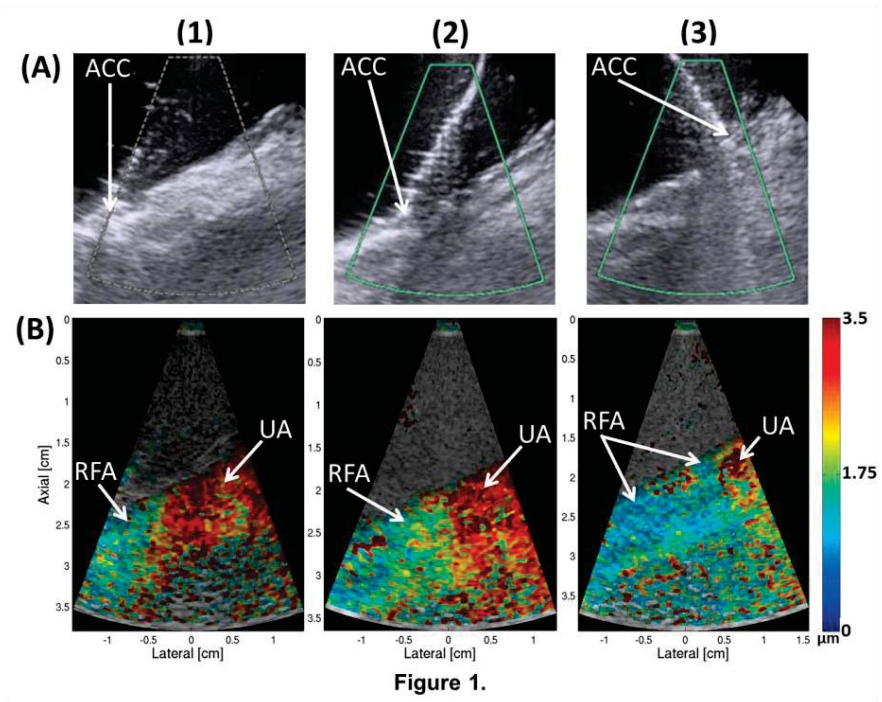

Figure 1.

Results: Overall, ARFI imaging was most successful when the myocardium was positioned at the imaging focus (between 1–2 cm for maximal acoustic energy delivery) and during normal sinus rhythm (NSR). Images acquired during AF frequently exhibited motion artifacts. Figure 1 shows the progress of a linear ablation along the LA roofline in a patient in NSR. Row B shows ARFI images acquired after RFA delivery at the ACC indicated in the B-mode images in row A. The color bar represents micrometers of tissue displacement away from the transducer. The ARFI-induced displacement of the RFA treated myocardium decreased relative to the unablated (UA) myocardium at the ACC point after RFA delivery, indicating increased myocardial stiffness.

Conclusions: Intraprocedure ARFI imaging visualized RFA treated myocardium as areas of increased tissue stiffness. This is the first demonstration of ARFI imaging in human patients, and these encouraging results demonstrate that intraprocedure ARFI imaging may prove useful for providing lesion visualization during cardiac ablation procedures.

References:

1. Eyerly SA, Hsu SJ, Agashe SH, Trahey GE, Li Y, Wolf PD: An in vitro assessment of acoustic radiation force impulse imaging for visualizing cardiac radiofrequency ablation lesions. J Cardiovasc Electrophysiol 2010; 21:557-563.
2. Eyerly SA, Bahnson TD, Koontz JI, Bradway DP, Dumont DM, Trahey GE, Wolf PD. Intracardiac Acoustic Radiation Force Impulse Imaging: A Novel Imaging Method for Intraprocedural Evaluation of Radiofrequency Ablation Lesions. Heart Rhythm 2012. In Press.

Imaging tumor margins with a mobile large area confocal scanner: Initial testing in the Pathology Department

Sanjee Abeytunge†, Yongbiao Li†, Bjorg Larson‡, Ricardo Toledo-Crow†, Milind Rajadhyaksha‡

Research Engineering Laboratory†, Dermatology Service‡

Memorial Sloan-Kettering Cancer Center, 1275 York Ave, New York, NY 10022

Purpose

In surgical oncology, the selective excision of tumors with minimal damage to the surrounding normal tissue is critical. Tumor removal is guided by examining pathology that is prepared during surgery. Preparation of pathology is labor intensive and time consuming. Typical preparation time is hours for frozen pathology during Mohs surgery and days for fixed pathology in head-and-neck, breast and other surgical sites. This often results in insufficient sampling of tissue and incomplete removal of tumor. For example, 20-70% of breast lumpectomy patients must subsequently undergo further resection. Confocal mosaicing microscopy offers a possible means to examine large areas of tissue with nuclear-level resolution directly on fresh excisions without the need for lengthy processing.

Recently, a method that creates mosaics by assembling individual confocal images of 1:1 aspect ratio and stitching them in post-process was reported. Although this mosaicing method has shown potential in diagnosing decease, it still takes too much time to be routinely implemented in surgical settings. To drastically reduce this time we developed a confocal microscope that scans strips of images with high aspect ratios and stitches the acquired strip-images simultaneously during acquisition.

Methods

We scan a line on the tissue (x-axis) with the microscope's polygon scanner and translate a stepper motor driven stage in the orthogonal (y-axis) direction to complete the scan of a strip. Each strip's x:y aspect ratio is approximately 1:25 for a 10-milimeter strip. Approximately ~20% overlap is maintained between any two strips (along x-axis) to reduce fall-off artifacts during stitching. A synchronizing mechanism was introduced to minimize the mismatch between any two strips along y-axis. An algorithm was developed to construct a seamless mosaic. The image strips are registered, fall-off artifacts corrected, overlap regions blended, and a seamless image is displayed in real time as the tissue is scanned. The instrument was constructed on a movable cart and taken to the Pathology Department to test on skin excision from Mohs surgery and breast tissue from lumpectomy and mastectomy surgery.

Results

Mosaics of skin excisions from Mohs surgery and tissue from breast surgery can be produced consistently showing cellular morphology. A 10 mm x 10 mm seamless mosaics can be produced in 75 seconds. A 3.5 cm x 3.5 cm breast tissue was also imaged.

Conclusions

Strip mosaicing confocal microscopy offers an imaging technology platform for real time detection of tumor margins directly in fresh tissue during surgery and from biopsies. Large amounts of tissue may be examined for tumor margins rapidly enough to be of practical use in surgical and clinical settings. The imaging can potentially be developed into an adjunct for pathology, to enable more complete and accurate removal of tumor.

Title: Imaging of Vessel Patency in Thiel Embalmed Liver
Authors: M Pendleton, BF Cox, T Saliev, M Rube, H McLeod, A Melzer
Affiliations: University of Dundee, Institute of Medical Sciences and Technology

Purpose: Anatomically correct models for training and testing purposes are in demand now more than ever where time, money and ethics are prohibitive. Advancements in surgical technology, imaging and preservation of specimens have all contributed to the pursuit towards a realistic and reproducible model. The University of Dundee is the first institution in the UK to offer soft tissue embalming developed in Graz, Austria. This relatively new embalming method preserves tissue colouring, flexibility and integrity including vessel structure. Our aim was to investigate the anatomic vessel characteristics of soft embalmed sheep liver by MR visualization. Knowledge of these behaviours will aide further in developing an accurate and reproducible liver phantom.
Methods - Several sheep livers were obtained from an abattoir (i.e. ethics are not an issue) and were freshly embalmed at IMSaT upon receipt, using Thiel fluid made up at CAHID at the University of Dundee. Prior to the imaging, the liver is flushed with 1litre of Thiel to flush any residual clots/debris and cool the tissue prior to gel injection. Various gel preparations were utilized which included Gelatine, Carrageenan and Polyacrylic Acid (PAA) in various combinations alone or together all gel preparation equalled less that 5% volume weight and were doped with a 1:50 concentration of Gadolinium (Magnevist, Schering). All images were obtained with a GE Signa HDct 1.5T MR unit. Image post processing was done with OSIRIX software (Pixmeo Sarl).

Results - The gel was successfully introduced into the venous portion of the hepatic vasculature resulting in Hepatic Vein and Vena Cava images obtained.

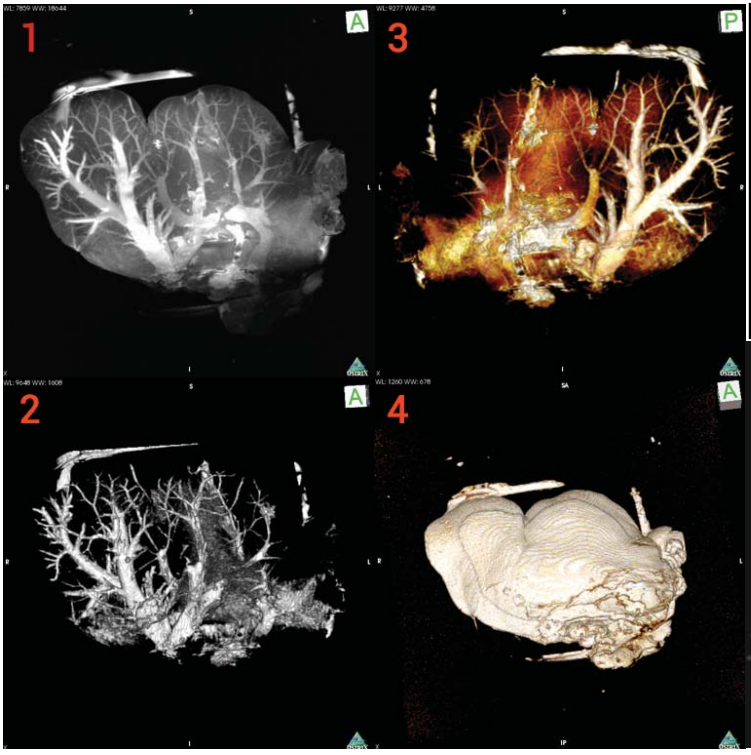

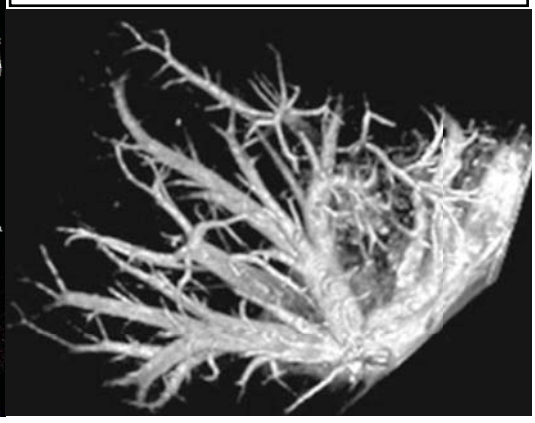

Figures **1-4**: **1.** Anterior view of liver, taken as a FIESTA sequence **2.** Anterior view of the liver, FIESTA image with post-3D reconstruction **3.** Posterior view of liver, FIESTA image with post 3D construction **4**. Anterior view of the liver, FIESTA image post-3D surface reconstruction **Below:** Close up 3D Volume rendering from FIESTA image.

Conclusions: We used soft embalmed explanted sheep liver to explore Thiel embalmed liver as a potential training and testing model in assessing liver vasculature. Using a more solid gel we were able to clearly see the patent vessels throughout the liver using MR imaging. The implications as such are that this opens a unique opportunity in developing image guided interventions on a reproducible and anatomical correct model. Research into the implications of vessel patency in the liver and other organs may yield exciting applications in establishing flow in an explanted organ. Furthermore emerging techniques such as sonication (FUS), needle guided biopsies and endovascular techniques may also benefit from such a model. Additionally isolated animal organ work will assist in developing Thiel soft-fix human cadavers as a viable interventional phantom for iMRI.

Adjustable Sleeve Template Assembly Device for Joint MR/US-guided Diagnosis and Treatment of Prostate Cancer: Initial Design and Feasibility Evaluation

Andriy Fedorov*[1], Sang-Eun Song*[1], Tina Kapur[1], Luciant Wolfsberger[1],
Robert Owen[2], Iris Elliott[3], William M. Wells[1], Clare Tempany[1]
[1]Brigham and Women's Hospital, Boston, MA [2]BK Medical, Peabody, MA [3]Hologic Inc, Bedford, MA

Purpose The independent value of both Magnetic Resonance Imaging (MRI) and transrectal Ultrasound (TRUS) for prostate cancer characterization and interventional guidance is widely recognized [1]. The combined use of these modalities is complicated by the significant deformation of the gland in between the imaging exams and differences in prostate appearance in MRI vs US. This typically requires deformable registration [2], which in turn is difficult to reliably validate. To facilitate characterization of prostate tissue using MRI and TRUS jointly, we propose the design and initial evaluation of a device assembly to facilitate identical configurations of the prostate gland in between MR and TRUS imaging.
Methods A device resembling a sleeve that can interchangeably accommodate MR or US imaging probe has been developed. Our design of the Adjustable Sleeve Template Assembly (ASTA) was intended to accommodate a rigid transrectal MR coil (Hologic Endo MRI Coil, Hologic Inc, Bedford, MA), and a rigid transrectal ultrasound transducer (BK 8848, BK Medical, Peabody, MA). Primary design considerations were: (C1) minimum profile of the device to minimize patient discomfort; (C2) diagnostic quality of the image; (C3) minimum/no disruption of the prostate anatomy while interchanging imaging probes; (C4) ease of repeat imaging. The scope of this study was feasibility assessment of bubble-free coupling between the imaged object and the TRUS transducer, and evaluation of imaging quality.
Results A rendering of the initial design consisting of a polymethylpentene (TPX) sleeve and a plastic spacer is shown in Fig.1. Diameter of the sleeve is 29 mm (layer thickness 1.8 mm). Upon experimental evaluation of the initial design using prostate TRUS phantom (CIRS, Norfolk, VA), practical difficulties of ensuring acoustic coupling of the phantom were encountered. The plastic spacer was substituted for a saline-filled endocavity balloon (Civco,Medical Solutions, Kalona, IA) that significantly improved image quality and reproducibility of the reliable acoustic coupling. Repeated TRUS imaging experiments of the phantom that included probe rotations and reinsertions (5 experiments total) were performed. Acoustic coupling and visually good quality of transverse and sagittal US images was confirmed.
Conclusions Device intended to maintain configuration of the prostate in between MR/TRUS acquisitions has been proposed and evaluated. Preliminary evaluation establishes comparable quality of TRUS imaging with and without the device. In contrast to similar approaches [3], the device id designed to accommodate MR imaging with the rigid endorectal coil. Future work will focus on evaluation of MR quality, reduction of the device profile and development of the patient evaluation protocol.

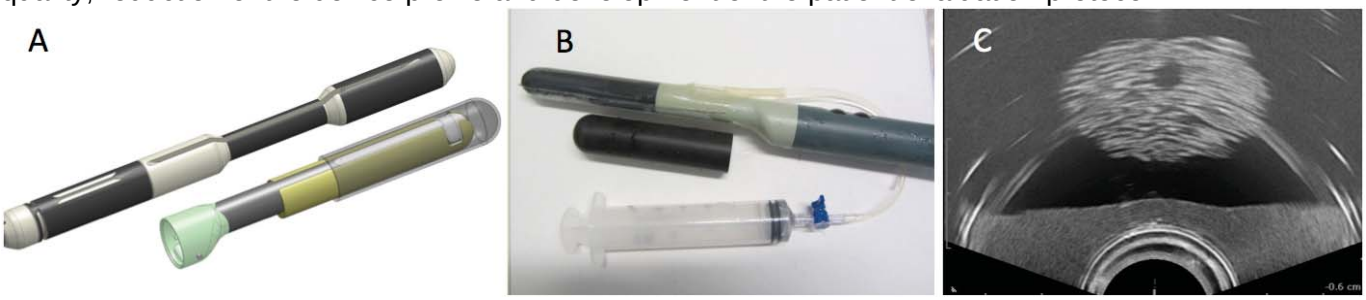

Fig.1: (A) Initial design of ASTA considered in this evaluation, together with the rendering of the Hologic MRI rigid coil and BK 8848 TRUS transducer; (B) BK 8848 TRUS probe with the saline-inflatable balloon placed over the transducer, and the manufactured ASTA sleeve; (C) prostate phantom transverse US image obtained through the ASTA/spacer assembly. Experiments confirmed the feasibility of obtaining artifact-free TRUS images.
References [1] Hou et al. Adv Urol. 2009 [2] Natarajan et al. Urol oncol. 2011. [3] Ukimura et al. Int J Urol. 2010.

Acknowledgments This work was supported by NIH grants R01CA111288 and P41RR019703.
**A.F. and S.-E.S. contributed equally to the presented study.*

Validation of THz Imaging for Burn Surgery Using MR

Neha Bajwa [1,3], Zachary Taylor [2,3], Bryan Nowroozi [1,3], Shijun Sung [2,3], Priyamvada Tewari [1,3], James Garritano[3], Ashkan Maccabi[1,3],Martin Culjat [1,3], Rahul Singh [2,3], Alexander Stojadinovic [5], Jeffry Alger [4], and Warren Grundfest [1,2,3]
[1] *Department of Bioengineering, University of California, Los Angeles, CA,* [2] *Department of Electrical Engineering, UCLA, CA ,* [3] *Center for Advanced Surgical and Interventional Technology (CASIT), Dept. of Surgery, UCLA*
[4] *Department of Neurology, UCLA, CA,* [5] *Walter Reed Army Medical Center, Department of Surgery, Washington, DC*

Purpose: Reflective terahertz (THz) medical imaging is a new modality with unparalleled sensitivity to changes in tissue water content. Previously reported *in vivo* studies demonstrate that spatially resolved hydration mapping with THz illumination rapidly and accurately detects fluid shifts following burn induction and provides highly resolved spatial and temporal characterization of edematous tissue. While hydration sensing methods based on optics and ultrasound have been studied, there is currently no standoff, wide-field, clinical imaging modality that utilizes hydration as the primary contrast mechanism, lending THz imaging as a potential image guidance tool for burn surgery. It is necessary to confirm the sensing mechanism of THz burn imaging using a diagnostic method that relies on tissue water content for contrast generation to support the translation of this technology to clinical application. The hydration contrast sensing capabilities of MRI are well established and are suitable markers to validate the hydration mapping capabilities of THz burn imaging.

Methods: *Ex vivo* porcine tissue phantoms were used to assess the feasibility of 7 T MRI of skin burns. Skin samples (25 mm x 50 mm sections, 2.5 mm thickness) were burned with a 18 mm x 6 mm brass brand heated to 300°C and 350°C. For MRI measurements, burned and control samples were immersed in a 50 ml centrifuge tube of Galden oil. T2-weighted multi slice multi echo (T2w MSME) images were then acquired for both pre and post burn samples. T2 relaxation times were determined by fitting equation **(1)** to the data where k is a function of the instrument's receiver gain, N(H) is proportional to the mobile proton density, T2 is the MR tissue relaxation time, and TE is the echo time.

$$S = kN(H)e^{-\frac{T_E}{T2}} \qquad (1)$$

Results: 7 T MR tissue characterization of *ex vivo* burns shows that T2 relaxation times and relative proton density behavior increase in post burn samples and with increasing burn wound temperature. T2 times and N(H) are closely related to tissue-water interactions, and thus change with burn application. Thermal injury of tissue results in cellular damage of the affected area and a loss in macromolecular-water interaction sites, increasing mobile water. This phenomenon is visualized as increased intensity of the burn region in MR generated images. **Fig. 1A** demonstrates that areas burned at 350°C are associated with a 2.4 fold intensity increase compared to surrounding normal tissue and pre burn samples. Mean T2 values of the burn region are 35.9 ms for 350°C and 30.2 ms for 300°C, where the characteristic T2 value of uninjured tissue is 24 ms. Proton density (N(H)) was increased in the burned epidermis in a temperature-related fashion (7.6% increase for 350°C and 2.4% for 300°C). Burn wound geometry, localization, and severity also correlate between MRI and histology **(Fig. 1B).** These MR results correlate well with THz imaging of *in vivo* partial thickness burns (**Fig. 1C**), which can accurately detect > 20% increases in THz reflectivity with respect to unburned skin in burn zones with a 0.5% sensitivity to water. Collectively, this data suggests that hydration gradients are responsible for the observed contrast in THz imaging.

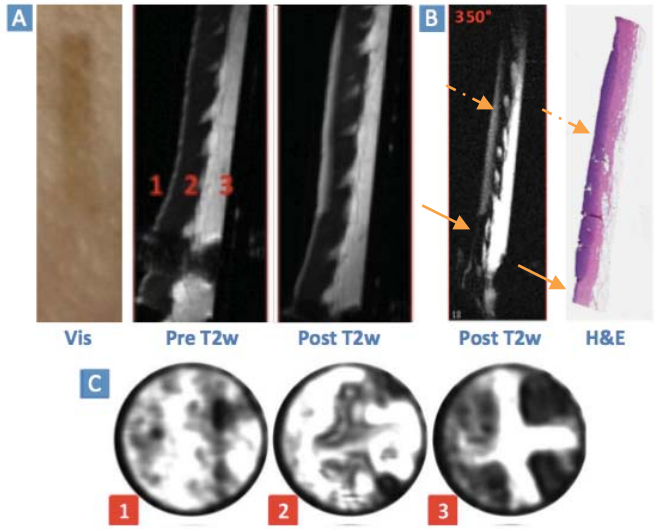

Fig 1. A) Visible image of burn and pre & post T2w MSME images of a 350°C burn. (1: epidermis, 2: dermis, 3: hypodermis) B) Post T2w MSME image of a 350°C burn with H&E (Dashed arrow: burn area, solid arrow: normal area). Thick, dark purple region corresponds to burn. C) THz images of a '+' shaped burn (1) prior to burn, (2) immediately following burn, (3) and 4 hr post burn.

Conclusions: MRI is a suitable method to evaluate the behavior of water molecules in burned tissues and furnishes multiparametric information, specifically T2 proton relaxation times and N(H) measurements, for non-invasive tissue characterization of skin burns. These MR hydration findings can be used to better understand and further reinforce the clinical utility of THz imaging for burn wound guidance.

Nanotechnologies for Image-Guided Therapies

Srinivas Sridhar, Northeastern University

Biocompatible nanomaterials are key components of novel approaches to addressing the major problems of disease diagnosis and therapy. We have developed several nanoplatforms that offer potential for significant improvements in multi-modal imaging and targeted delivery of therapeutics. Theranostic magnetic nanoplatforms combine multiple functionalities including imaging, magnetic targeting to the disease site, delivery of the drug payload through sustained as well as triggered drug release. We have demonstrated in vivo multimodal imaging using MRI, SPECT and FMT using these nanoplatforms.

We have developed a new approach to chemoradiation therapy (CRT), termed Biological In-Situ Image Guided Radiation Therapy, that involves the coating of spacers routinely used during radiation therapy with nanoparticles that release radiosensitizing drugs (e.g. docetaxel DTX for Prostate Cancer), that is synchronized with the radiation therapy schedule, with almost no systemic toxicity. This new nanoparticle approach is an exciting new combinatorial therapy for cancer as well as other diseases where image-guided radiation therapy is currently a preferred choice of treatment.

The talk will also describe other significant developments in this emerging field.

Supported by the National Science Foundation, National Cancer Institute and DoD Prostate Cancer Research Program, and Mazzone Foundation.

Feasibility of Using Simultaneous PET/MR in the Evaluation of Cervical Carcinoma

Perry Grigsby[1, 2], Maria Thomas[1], Katie Fowler[1,2], Jonathan McConathy[2], Agus Priatna[3], Farrokh Dehdashti[1, 2]

[1]Washington University School of Medicine, [2]Mallinckrodt Institute of Radiology, [3]Siemens Healthcare

Purpose: The aim of this pilot study was to evaluate the clinical utility of simultaneous acquisition of PET and MR imaging in patients with cervical cancer and to compare PET/MR images (Siemens Healthcare Biograph mMR) with those obtained with PET/CT.

Materials and Methods: Integrated whole-body PET/MR imaging was acquired for 14 patients with cervical cancer using the Siemens Biograph mMR system installed at the Mallinckrodt Institute of Radiology at Washington University. A prospective institutional study was developed in which PET/MR imaging was acquired following FDG-PET/CT obtained for clinical evaluation. All patients received a single injection of FDG and underwent a PET/CT immediately followed by a PET/MR. PET/CT was performed according to our standard clinical protocol with CT attenuation correction. The PET/MR utilizes avalanche photodiodes in the bore of the 3T magnet for simultaneous image acquisition. mMR PET attenuation correction was performed using a dual echo VIBE Dixon sequence. For each scan, PET imaging parameters were determined, including SUV_{max} and metabolic tumor volume (MTV). Sites of disease were assessed with PET/MR and compared with findings on PET/CT. Three patients had newly diagnosed disease, 3 patients were under treatment with chemo-radiation and 8 patients had completed therapy.

Results: Simultaneous PET/MR image acquisition was feasible in this initial pilot study. Visual interpretation of imaging from both patients with newly diagnosed cervical cancer demonstrated comparable findings for the primary tumor and pelvic lymph nodes. SUV_{max} of the primary lesion was within 20% for all three patients. Similar findings were observed for the three patients who were evaluated for response to treatment. None of the 8 patients who underwent posttherapy imaging demonstrated PET or MR evidence of active disease by either PET/CT or PET/MR imaging.

Conclusion: Simultaneous PET/MR imaging provides a novel method to perform integrated anatomic, metabolic and functional imaging. A major advantage is the synchronous acquisition, which avoids differences in patient position, bladder and rectal filling, and tumor growth. Simultaneous PET/MR may be especially valuable in comparing tumor boundaries between PET and various MR sequences, in radiation treatment planning, in minimizing patient scan time when both PET and MRI are desired, in reducing radiation dose to patients, and in interpreting cases with indeterminate findings by providing co-localization of the two modalities.

This study demonstrates that integrated PET/MR is feasible in patients with cervical cancer with good concordance of imaging findings with standard of care FDG-PET/CT.

Ultrasound-Guided Fast Robotic Catheters for Beating Heart Surgery

Samuel B. Kesner[1], Paul Loschak[1], Nikolay Vasilyev[2], Pedro del Nido[2], and Robert D. Howe[1]
[1]Harvard School of Engineering and Applied Sciences, Cambridge, MA
[2]Boston Children's Hospital, Boston, MA

Purpose: Robotic cardiac catheter surgery coupled with ultrasound guidance has the potential to minimize the risks of open heart surgery by compensating for rapid heart motion [Bebek et. al. 2007, Ginhoux et. al. 2005]. Ultrasound has the ability to visualize structures through blood, allows for real time imaging of soft tissue motion, and is widely accepted clinically. Our lab has created the first ultrasound-guided catheter robot that compensates for heart motion in real time *in vivo* [Kesner et. al. 2010].

Methods: The robotic catheter system consists of the drive system that actuates the catheter, the catheter module that is inserted into the heart, and the 3D ultrasound visual servoing system that tracks the tissue and commands the catheter to move (Fig. 1). The system compensates for the motion of the outer annulus of the mitral valve, which travels along a linear degree of freedom with approx. 20 mm displacement, 210 mm/s velocity, and 3800 mm/s^2 acceleration.

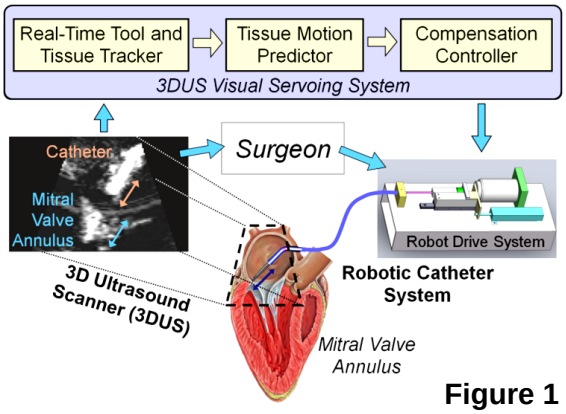

Figure 1

The ultrasound scanner streams 3D images to an image processing computer. A GPU-based Radon transform algorithm finds the catheter axis in real-time. The target tissue is then located by projecting the axis forward through the image volume until tissue is encountered. An extended Kalman filter estimates current tissue location based on a Fourier decomposition of the cardiac cycle to compensate for the 50-100 ms delay in image acquisition and processing.

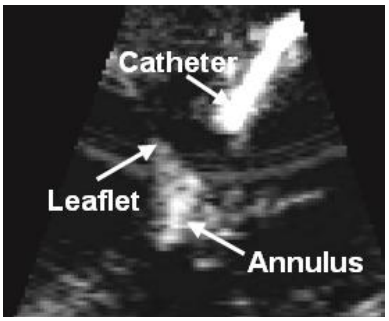

Figure 2

Results: To investigate clinical feasibility, the system was evaluated *in vivo* on a 75 Kg porcine animal model. The 3D ultrasound system (SONOS 7500, Philips Healthcare, Andover, MA, USA) was positioned to visualize the catheter and the mitral valve annulus (Fig. 2). The catheter was then driven to compensate for valve motion and track the moving tissue. Tracking results had RMS errors less than 1.0 mm in all experimental trials (0.77 mm RMS error in Fig. 3). The tracking error was caused by respiration motion not captured in the tissue tracking system, performance limitations of the actuated catheter caused by backlash and friction, and the small beat-to-beat variations in the valve motion.

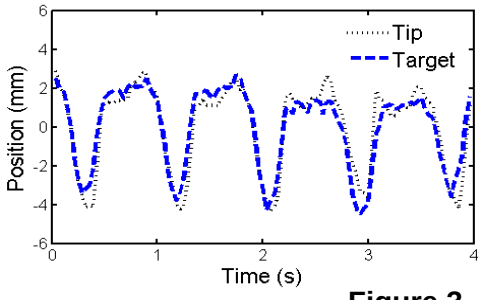

Figure 3

Conclusions: The *in vivo* experiments validated the ultrasound-guided catheter robot's ability to compensate for mitral valve motion. Further studies are now being conducted to expand the system to 3D motion compensation and 3D tissue tracking. This would allow the robotic system to obtain accurate position or force control between the catheter tip and any desired cardiac tissue region exhibiting fast and complicated motion.

Title

MRIgRT facility design: magnetic field decoupling of an MRI-on-rails from a linear accelerator

Authors

T. Tadic, D. Jaffray, T. Stanescu

Purpose

To quantify the interaction between the magnetic fringe field of an MRI scanner and the structural components of a therapy linear accelerator (i.e., linac) for the design of an MRI-on-rails-linac therapy facility.

Methods

The first step consisted of generating a certain coil configuration by means of linear programming and optimization techniques to reproduce the magnetic fringe field lines of the MR magnet, which were provided by the manufacturer. In this approach, a coil space is searched to compute a global solution representing the most optimal ensemble of coils for a pre-defined magnetic field (B0) distribution. In the second step, the coil configuration was inputted in COMSOL Multiphysics (Burlington, MA), a finite element methods based simulation software, as the starting point of the magnetic field decoupling simulations. To generate a realistic MRIgRT facility, all ferromagnetic components were modelled, namely the R-bar structural components existing in the room walls, obtained from architectural drawings, and the main structural components of the linear accelerator (e.g., frame, base). The optimization problem of magnetic decoupling consisted of achieving the minimum distance between the MR magnet and linac while fulfilling two critical requirements: a) minimize the magnetic fringe field at the linac waveguide (less than 10 G) to ensure the linac output is not perturbed by the proximity of the MR magnet, and b) maintain the MR magnet standard field homogeneity over the entire imaging volume, thus avoiding any interference with the neighboring linac. Magnetic field spatial distributions and ppm inhomogeneities maps were used to characterize the field at the linac waveguide and the spatial uniformity of the MR scanner, respectively.

Results

The key components of the MRIgRT facility were simulated including the MR magnet fringe field, the linac components and the linac vaults layout. The magnetic field decoupling constrains imposed on the system design were achieved for both the MR scanner (field homogeneity) and the linac (electron gun and waveguide operation).

Conclusions

The integration of an MRI-on-rails with a therapy linear accelerator can be achieved, one of the challenges being the mutual magnetic decoupling of the MR magnet and linac.

Abdominal Surface Registration in Percutaneous Image-Guided Therapy

Michael Scherer[1], Logan Clements[1], Jim Stefansic[1], Yuman Fong[2]
[1]Pathfinder Therapeutics, Inc. (Nashville, TN)
[2]Memorial Sloan Kettering Cancer Center (New York, NY)

Purpose

Image-guided therapy (IGT) has gained widespread attention and clinical acceptance for use in localizing tumors in abdominal organs for ablation or resection. In an ideal IGT procedure, a 3D map or plan is created from the preoperative diagnostic images, possibly days before the actual procedure and in consultation with a variety of physicians in different disciplines. On the day of the percutaneous procedure, the position of the patient and the medical instruments are accurately localized or "registered" onto these preoperative images in the interventional suite.

Commercial interventional radiology IGT devices (e.g., Philips Traxtal™ system) register the preoperative images to physical (patient) space using skin fiducial markers. The disadvantage of these systems is that the high quality diagnostic images cannot be easily used during the interventional procedure, meaning physicians do not have access to detailed visualizations of lesions and vasculature. The existing technology also requires that the patients be scanned at least twice, which increases their exposure to CT radiation. Therefore, it would be ideal to use the high quality diagnostic CT or MR medical images directly for percutaneous guidance by performing a registration using those images. This abstract summarizes a registration method that matches abdominal surfaces generated from pre-operative diagnostic images to physical surfaces obtained during surgical or interventional procedures, along with initial clinical feasibility.

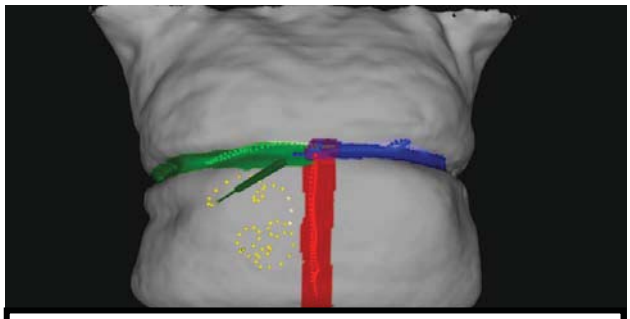

Abdominal surface registration. Pseudo-features were identified as the sternum (purple), left (blue) and right (green) of sternum, and midline in direction of umbilicus (red). In this still frame, pseudo-features have already been swabbed intraoperatively and the abdominal surface is now being marked (yellow points) with the optically tracked probe (green cylinder).

Methods

Standard diagnostic triphasic spiral CT images of the patient's liver were acquired in preparation for a surgical procedure. The Pathfinder Scout™ liver surgical planning software was used to semi-automatically segment the liver, tumors, and vessels, and manually segment the abdominal surface. In addition, "pseudo-features" (see figure above), which can be identified in physical space as part of the surface registration process, were painted on the segmented abdominal surface. Pseudo-features include anatomic structures or regions on the abdominal surface that can be easily identified and accessed during an interventional procedure.

During surgery, the Explorer™ image-guided surgical system was used to acquire physical pseudo-features and abdominal surface data and a registration algorithm (Clements, et al. *Medical Physics* 35:6, pp. 2528-2540) was used to align the physical data to the preoperative imaging data.

Results

The surface registration was qualitatively evaluated by touching external and internal targets through a hand port and comparing to the probe tip location on the images. Registration accuracy of both external and internal targets was deemed accurate by the physician.

Conclusion

The registration method outlined above has been used successfully to match the surface of the liver to preoperative images of this organ for open and laparoscopic image-guided surgery in over 300 cases. In applying this method to interventional procedures, further evaluation is necessary to assess effects of respiration and changes to the abdominal surface between preoperative imaging and image guidance.

New developments in gradient-based tracking for MRI

Erez Nevo, Abraham Roth, Amir Roth, Alexander Zosin, Barry Fetics, Mathew Philip (Robin Medical, Baltimore, MD)

Purpose: The EndoScout tracking system for MRI was introduced into clinical use in 2005. Since then it has been used in hundreds of surgical procedures, almost all on the Signa-SP. In the following we present new developments that were done to facilitate the use of the EndoScout system on close bore scanners.

Methods:

1. Tracking at the edge of the scanner – limited access to the patient in close bore scanners requires the conductance of interventions out of the bore. We expanded the tracking range of the EndoScout to include the outer 40cm range of the bore where the operator can reach easily to the patient.

2. Elimination of the need to acquire gradient commands – some scanners do not have standard outputs of gradient commands, and if there are outputs – scanner vendors hesitate to grant permission to connect. To enable tracking on these scanners, we modified the tracking algorithm to work with estimated gradient commands. This also eliminates the need to cross the penetration panel with copper wires as required in the original configuration of the EndoScout.

3. Guiding device for out-of-bore intervention – we developed a new device to align and insert biopsy needle to the prostate out of the bore, based on images and tracking data that were collected shortly before (Figure 1).

4. Head mounted display (HMD) – we adapted commercial, low cost 3D goggles into MRI compatible HMD with 3D visualization (Figure 2). We also attached an EndoScout tracking sensor to the HMD to track its position and a camera to provide view of the operational field, and generated 3D augmented reality (AR) display including the operational field, MRI image set, and tracking annotation.

Results:

1. Tracking accuracy at the edge of the bore (0.16±0.12mm (mean ± std. dev. of the 3D tracking errors) for N=1040) was similar to tracking accuracy at the center of the bore (0.21±0.11mm, N=1560 locations).

2. Tracking without gradient command measurements were similar to tracking of the same sensor data but with measured gradient fields (Figure 3 shows tracking results for a moving device, regression plots and differences).

3. Working out of the bore with MR images and tracking data recorded shortly before enabled fast and accurate device alignment by setting a rotation and an angulation parameters, followed by needle insertion into phantom.

4. The HMD provides high quality, undistorted display inside the bore of the scanner. Augmented reality visualization showed good agreement between MRI and view inside the bore (Figure 4). HMD reduced SNR by 2% when used near the bore and by 13% when used inside the bore. The HMD was found to be extremely convenient for realtime device guidance inside the bore.

Conclusions:

These new developments provide a versatile guidance system for close bore MRI scanners that can be used to guide interventions inside the bore, at the edge of the bore, or out of the bore. Tracking based on the gradient fields, without actually measure the gradient commands, greatly simplifies the system installation (the only connection going out from the scanner is an optic fiber), provides the same tracking performance as with measured gradients, and eliminates the need to get certificate of compliance from the scanner vendor.

Figures 1 (left) to 4 (right)

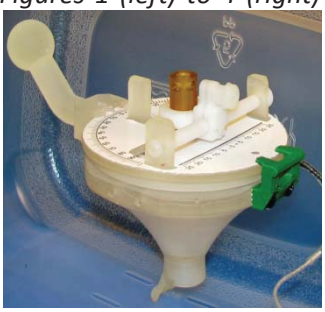

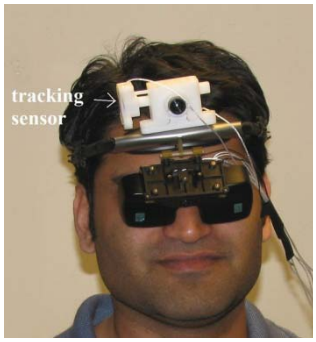

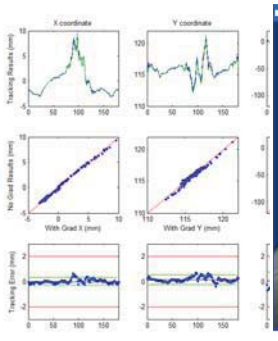

Tracking of 19F labeled Interventional Devices by means of 3D Golden Angle Radial Sampling

Hahn T[1], Kozerke S[1], Schwizer W[2], Fried M[2], Boesiger P[1], Steingoetter A[1,2]
[1] Institute for Biomedical Engineering, University and ETH Zurich, Switzerland
[2] Division of Gastroenterology and Hepatology / DIM, University Hospital Zurich

Purpose: To investigate the in vivo performance and real-time capability of 3D Golden Angle (3DGA) sampling for the tracking of interventional devices by means of fluorine Magnetic Resonance Imaging (19F MRI).

Methods: *19F catheter:* A duodenal Levin tube was modified to include four Perfluoro-15-crown-5-ether filled capsules along the catheter (Fig.a). Capsule volume was 65µl. *Data acquisition:* All experiments were performed on a 3T whole-body MRI system (Achieva, Philips Healthcare). A radial SSFP 3DGA sampling scheme [1-3] was implemented, yielding a relatively uniform coverage of k-space at any time and for any chosen reconstruction window size and allowing for a free choice of the temporal resolution Δt. Scan parameters: TR/TE 3.6/1.8ms (in vivo), TR/TE 3.7/1.8ms (real-time), spatial resolution 4mm, FOV 64x64x64cm^3, non-selective block pulse. *In vivo experiment:* Informed consent was obtained from the subject prior to the study. The catheter was nasally inserted in one healthy volunteer and pulled back during 19F data acquisition. Three different tracking algorithms were implemented: Boundary condition free tracking, i.e. peak-finding on undersampled (dynamic) images; composite image based tracking, i.e. multiplication of dynamic images with composite images, c.f. HYPR [4]; and model based tracking, i.e. incorporation of a priori knowledge. *Real-time experiment:* A gel phantom was built. Radial k-space profiles were transferred to an external PC in real-time. There, 3D 19F images were reconstructed for boundary condition free catheter tracking. Real-time feedback was given by projecting the position, SNR and velocity of the 19F capsules as well as a fitted catheter-guided imaging plane inside the MR room.

Results: *In vivo* simultaneous tracking of multiple identical 19F capsules is feasible up to Δt=252ms (Fig.b). Composite and model based tracking both increase tracking reliability and allow for higher temporal resolutions. Model based tracking allows to uniquely identify each capsule`s trajectory over time. The *real-time* tracking framework was successfully implemented (Fig.c). A mean computation time per dynamic of 196ms was achieved. Tracking reliability was more than 85% for Δt=185ms, 370ms and 740ms as well as for catheter velocities from 3mm/s to 19mm/s.

Conclusions: 3DGA based tracking of multiple 19F capsules is a promising tool for the real-time tracking of interventional devices such as cardiovascular catheters.

References: [1] Chan et al. MRM 2009 [2] Hahn et al. ISMRM 2011 [3] Hahn et al. Radiology 2012 (in press) [4] Wieben et al. ISMRM 2006

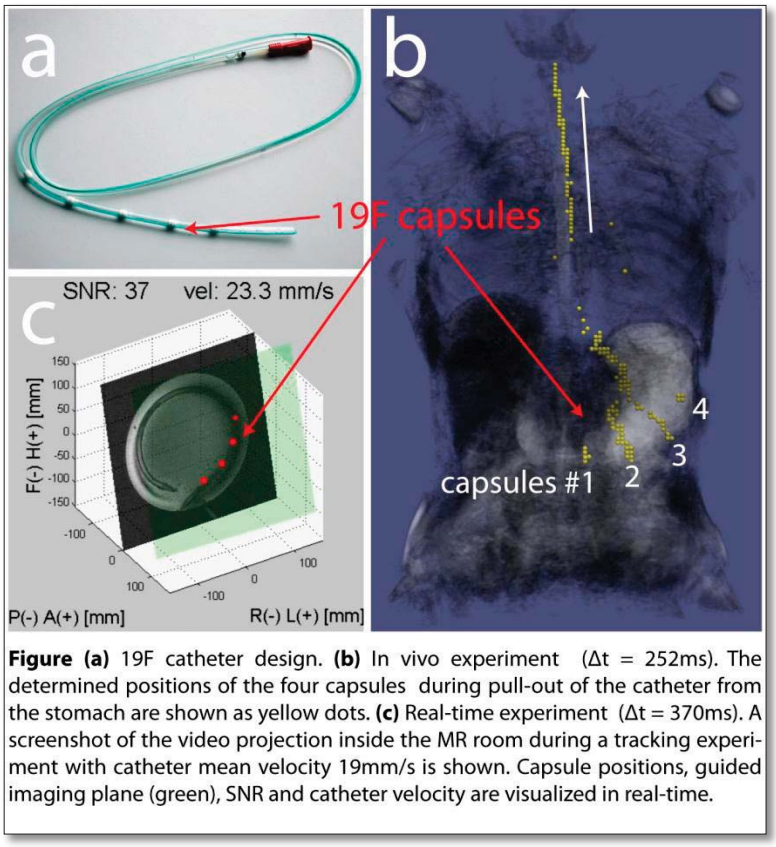

Figure (a) 19F catheter design. **(b)** In vivo experiment (Δt = 252ms). The determined positions of the four capsules during pull-out of the catheter from the stomach are shown as yellow dots. **(c)** Real-time experiment (Δt = 370ms). A screenshot of the video projection inside the MR room during a tracking experiment with catheter mean velocity 19mm/s is shown. Capsule positions, guided imaging plane (green), SNR and catheter velocity are visualized in real-time.

3D SLICER BASED APPROACH FOR PLANNING AND PERFORMING IMAGE GUIDED LASER INDUCED THERMAL THERAPY

Erol Yeniaras, David T. Fuentes, Samuel J. Fahrenholtz, Renjie He, John D. Hazle and R. Jason Stafford
Department of Imaging Physics, The University of Texas MD Anderson Cancer Center, Houston, TX

Purpose:

MR-guided Laser Induced Thermal Therapy (MRgLITT) is an emerging minimally invasive alternative to conventional surgery for brain tumors under investigation [1, 2]. While real-time MR temperature imaging (MRTI) can provide procedural monitoring, because of the need for stereotactic guidance, a need still remains for planning a suitable approach to the procedure to maximize the probability of being able to successfully deliver therapy. We demonstrate a novel approach to prospective 3D treatment planning MRgLITT procedures in brain with a focus on quickly taking into account local boundary conditions so as to illustrate the steady-state heating profile of the laser. The software incorporates the use of MR acquisitions currently used for neurosurgical planning, allowing the user to interactively navigate tissue, simulating effect of applicator trajectory and laser exposure, and then provide a more rigorous computation once the laser is positioned.

Methods:

A loadable 3D Slicer module (LITTPlan), was developed that uses a finite element solver to simulate the induced heating and expected tissue damage based on a dose model and facilitates virtual adjustment of laser applicator(s) position/power relative to 3D anatomy and visible boundary conditions, to evaluate results of different treatment scenarios (Fig. 1). Patient baseline MRI is used to segment tissue in treatment region (e.g., grey/white matter, edema, CSF, bone, air), identify potential convective heat sinks (nearby vessels, ventricles, etc), and estimate tissue perfusion in the region (CBF). The user specifies applicator location(s), target treatment volume and critical structures for segmentation prior to mesh generation as well as laser power settings (Fig. 2).

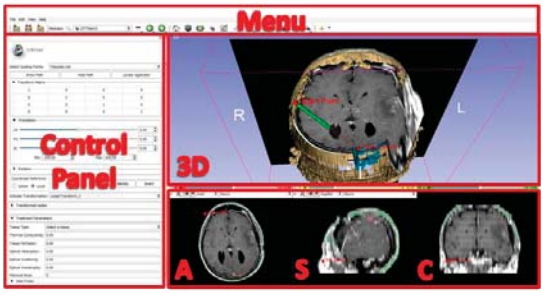

Fig. 1: 3D Slicer interface for monitoring the therapy.

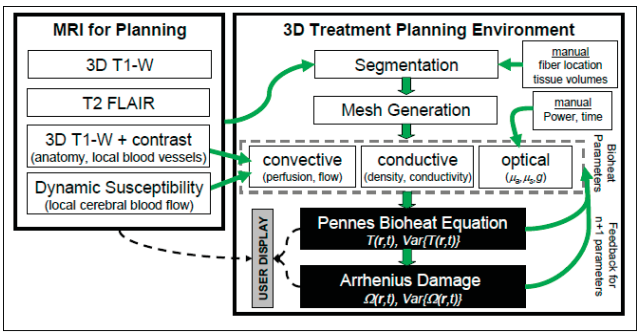

Fig. 2: Flowchart depicting major components proposed for MRI data driven prospective 3D LITT planning.

Due to the lack of specific a priori knowledge of patient specific parameters outside those provided by images, a relatively simple computational model (linear Pennes Bioheat Equation and ODA optical fluence model) was employed for speed. Estimates for initial bioheat parameters were based on literature values and best estimates for the segmented region. Temperature, T(r,t), was calculated and resulting isotherm estimates of damage were registered as overlays on the treatment planning images.

Results: The virtual environment developed is able to provide simultaneous visualization of the MR planning images, segmentations of critical structures, and thermal dose estimates in near real-time. The steady state implementations of the bioheat solvers provides estimates of the thermal dose that qualitatively deform to the expect heat sinks on a portable workstation environment in < 20 seconds.

Conclusions: The presented efforts demonstrate the feasibility of incorporating physics based predictions of the bioheat transfer into an interactive virtual planning environment in near real-time. The three dimensional environment for planning the procedure presents opportunities for patient selection and optimizing treatment approach. Future work includes retrospective quantitative validation of the steady state predicted thermal dose estimates using phantom and retrospective modeling of in vivo animal and human data. Additionally, an uncertainty quantification formalism will be incorporated to provide a confidence interval for the result. The uncertainty (e.g., from probe location, fluence, convective or conductive properties) in the model will be propagated such that uncertainty in both temperature and damage can be quantified and displayed to enhance the interpretation of the simulation.

Acknowledgments: This research is supported in part by the MD Anderson Cancer Center Support Grant CA016672 and the National Institutes of Health (NIH) award 1R21EB010196-01. All opinions, findings, conclusions or recommendations expressed in this work are those of the authors and do not necessarily reflect the views of our sponsors.

References: 1. F. Ulrich, Med. Laser Appl., 2005. 20: p. 119-124.; 2. Schulze, P.C., et al., Acta Neurochirurgica, 2004. 146(8): p. 803-812.

Deformation Compensation Strategies for Image Guided Surgery Using Sparse Data

Michael I. Miga, Ph.D.
Associate Professor of Biomedical Engineering[1], Associate Professor of Radiology and Radiological Sciences[2], Associate Professor of Neurological Surgery[2]
[1]Vanderbilt University, [2]Vanderbilt University Medical Center

With the continued improvements in high performance computing, the ability to translate complex models using large systems of equations from predictive roles to ones that are more integrated within diagnostic and therapeutic applications is becoming a rapid reality. In this talk, I will discuss recent experiences exploiting the use of computationally intense soft-tissue models for the correction of deformations during image-guided surgery. Emphasis will be on applications that place computational models and novel sparse measurement technologies within the surgical feedback loop to change the delivery of treatment. The common thread that ties the work together is that, throughout each experience, the solution requires the extrapolation of cost-effective relevant information from distinctly finite or sparse data while balancing the competing goals between workflow and engineering design, and between application and accuracy.

MRI-guided Fully Actuated Robotic Prostate Biopsy and Brachytherapy

Hao Su[1], Gang Li[1], Weijian Shang[1], Junichi Tokuda[2], Nobuhiko Hata[2],
Clare Tempany[2] and Gregory S. Fischer[1]
[1]Department of Mechanical Engineering, Worcester Polytechnic Institute, Worcester, MA, USA
[2]Department of Radiology, Brigham and Women's Hospital, Boston, MA, USA

Purpose: Needle-based percutaneous interventions, e.g. biopsy and brachytherapy, are the typical procedures for prostate cancer. MRI-guided therapy affords higher precision for interventional procedure, with high contrast tissue anatomic structure to the surgeon. Fully actuated robotic needle placement allows the clinicians to perform this procedure outside the tightly constrained scanner bore, simplifying the time-consuming manual alignment or insertion, decreasing the error due to hand tremor, and avoiding awkward posture.

Methods: A 6 degree-of-freedom (DOF) robot has been developed to perform robotic biopsy and brachytherapy with actuated insertion under the clinician's control. The robot consists of a 3-DOF Cartesian stage and a 3-DOF needle driver, as shown in Fig. 1. The needle driver offers 1 DOF cannula translation, 1 DOF cannula rotation (the 1 DOF cannula rotation can potentially reduce the needle insertion force and needle deflection), and 1 DOF stylet translation. Coordinated motion is implemented between the cannula translation and stylet translation, to perform biopsy and brachytherapy. Phantom experiments of automated prostate biopsy and brachytherapy were performed under MRI-guidance, as shown in Fig. 1. Beans with an approximate diameter of 9mm, were embedded in the gelatin phantom to serve as biopsy targets. An 18G MRI biopsy needle is placed in the gelatin phantom and imaged with the T2-weighted fast spin echo imaging protocol (T2W TSE). A 3×3 pattern of seeds (three seeds per needles) was applied with the robot. Custom made brass seeds and plastic spacers are employed to mimic the radioactive seeds, with length of 5mm for both seed and spacer.

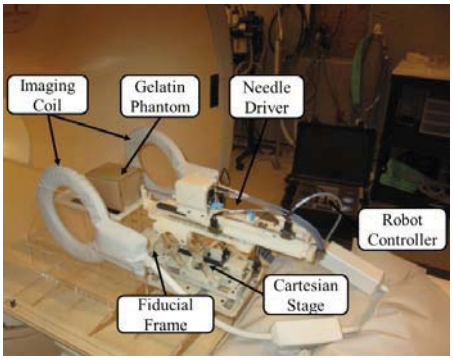

Figure 1. The prostate interventional robot inside 3T MRI scanner showing the phantom experimental setup

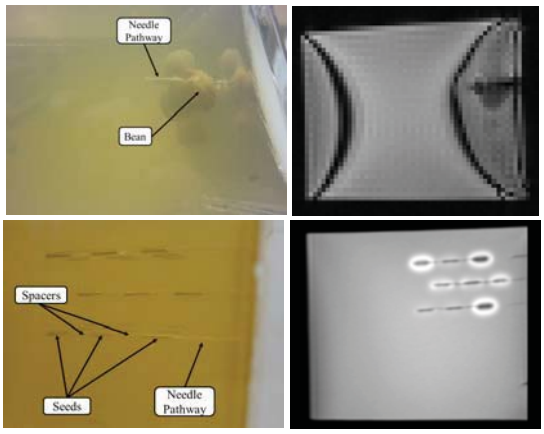

Figure 2. (Top) gelatin phantom with biopsy targets and the real-time MRI image of the target gelatin phantom with the needle in the bean, and (bottom) gelatin phantom with brachytherapy seeds and the MRI image of the target gelatin phantom

Results: The results of brachytherapy seed placement demonstrate an RMS error of 0.98mm with a standard deviation 0.37mm, compared with the proposed seed distribution pattern (as measured using a segmented high resolution CT scan of the phantom with implanted seeds). The errors are caused by the needle deflection, considering the bevel tip of the brachytherapy needle, which could be reduced by rotating the cannula to reduce the insertion force. Moreover, the custom made seeds and spacers are not exactly the same length, that could also introduce some errors.

Conclusions: Phantom experiments validate the capability and flexibility of the system to execute automated prostate biopsy and brachytherapy with only minor modification of the typical clinical workflow. The preliminary results are satisfactory with an RMS seed placement accuracy of approximately 1.25mm. The proposed architecture overcomes a majority of the limitations of manual insertion by allowing the clinician to control the robot from beside the patient but outside the tightly constrained bore.

Patient Image Viewing for Facilitating Interventional Device Placement

Andrew B. Holbrook[1], Pejman Ghanouni[1], Kim Butts Pauly[1]
[1]Department of Radiology, Stanford University, Stanford CA

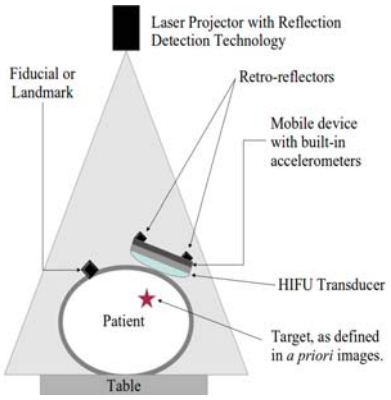

Figure 1: System schematic. A laser projector is positioned above the patient, and the projection space is landmarked to a fiducial on the patient. Retro-reflectors affixed to a device with built-in accelerometers determine the device's position with the projector space. This sensor is in turn attached to the FUS transducer, allowing for images to be displayed of the underlying anatomy.

Purpose: MRgFUS treatments with extracorporeal transducers can be unnecessarily lengthened by iterative device placement and imaging verification. The motivation of this work is to improve MRgFUS workflow by introducing an image-based feedback method for transducer placement before the patient is moved into the MR system.

Methods: A ShowWX+ Pico Projector with RetroTouch technology (Microvision, Inc., Redmond, WA) was calibrated and mounted above a MR750 3T table (GE Healthcare, Waukesha WI). The projector is able to detect reflections from a sensor consisting of reflectors mounted on a mobile device attached to the FUS transducer (Fig. 1). Reflector locations within its projection field are determined from these reflections and the accelerometer data. Patient fiducial markers can also be localized in a similar way, with a smaller reflection tool. No accelerometer is necessary if the reflectors around the fiducial are in a known scan plane. This provides registration with the previously acquired data.

Once the sensor and transducer position are known, three images from a previously acquired dataset (either CT or MR) are displayed on an in-room display right at the patient bed: two transverse and one parallel to the device face, depicted as a square overlay. The sensor is then repositioned until the images are centered on a predefined target.

In an experimental study, a target was selected on a previously acquired dataset of a covered phantom with a single external fiducial, imaged with a 3D sequence (3D axial SPGR, TE/TR 2.1/4.5ms, 25cm FOV, 2mm slice thickness, 62.5 kHz BW, 256x128x164 matrix size, NEX 2). The FUS transducer was skipped for this demonstration and just the sensor was placed according to the methods described above. To illustrate correct placement, bright markers were placed in the location of the sensor, in the same orientation, and the phantom was imaged, and the location analyzed.

Results & Conclusions: Example images from the experiment are shown in Figure 2. The sensor was repositioned until the target area appeared to be underneath. The positioning time took under a minute, including landmarking to the fiducial. With this position, the four bright markers demonstrate that the sensor was directly over the target location.

As the phantom was covered, the only physical reference utilized was the external fiducial. Thus, patient image viewing of previously-collected volume data can potentially reduce placement time of external HIFU transducers and other devices by improving the device placement success. Future work will focus on improving accuracy as well improving the user experience to further reduce treatment preparation time, as well as implementing this work into existing clinical trials where patients undergo a CT scan prior to HIFU ablation.

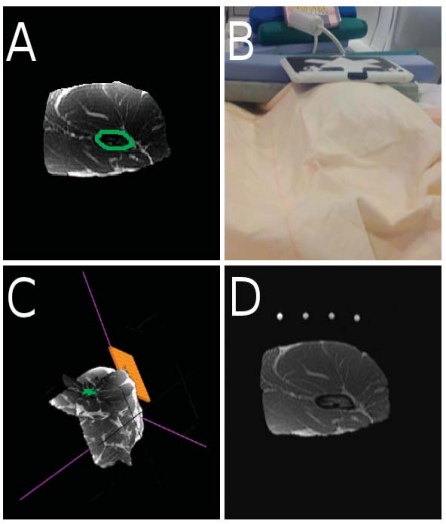

Figure 2: Image viewer work flow. A target can be painted in the a priori images (A). Next, after landmarking, the sensor can be placed inside the projection field (B). The sensor and slices directly underneath are immediately visualized on an in-room display (C). Finally, a phantom with a line of vertical markers was placed in the same location as the sensor, directly over the target and the phantom was re-imaged (D).

Acknowledgements: We acknowledge assistance from Mark Freeman and Selvan Viswanathan from Microvision, and our funding support from NIH R01-CA121163 and P01-CA159992.

Poster Abstracts

Image-Guided Robotically-Steerable CT-Compatible Instrument for Multi-Adjacent-Point Targeting

Meysam Torabi[1]; Andrew Harris[1]; Alex Golden[1]; Rajiv Gupta[2], MD, PhD; Conor Walsh[1], PhD

1. Harvard Biodesign Lab, Harvard School of Engineering and Applied Science, Wyss Institute for Biologically Inspired Engineering at Harvard University.
2. Department of Radiology, Massachusetts General Hospital, Harvard Medical School.

Purpose

The project pursues quantitative and qualitative validation of the performance of a CT-guided compact interventional tool by developing an IGT module in 3D Slicer.

Methods

The robot is particularly designed for multi-adjacent-point targeting for accessing irregularly-shaped surgical sites with single needle-insertion. The robot takes advantage of one rigidly straight cannula and one flexibly curved stylet which due to its super elasticity can be substantially straightened when it is retracted inside the cannula. Cannula rotation, cannula translation and stylet insertion make the robot able to cover a 3D volume. The closed-form inverse kinematics along with a marker-based registration has been developed and is integrated into 3D Slicer. The registered working zone is then aligned on the organ of interest so that the surgeon can interactively clicks on the desired targets via the point-and-click user interface. The paths for multiple targets are then visualized on the medical image. The module is externally connected to Galil library to drive three micro stepper motors via OpenIGTLink for steering the needle through soft tissue. Mechanical design details and analyses of the robot have been documented and published.

Results

Results demonstrated that the integrated system, shown in the figure, achieves targeting errors of less than 2mm and 1mm in ex-vivo bovine tissue and ballistic gelatin respectively.

Conclusions

The instrument operates reliably using a clinically-inspired workflow based on the proposed image-guided system architecture, and is able to achieve conformal targeting maps to cover the volume of interest. We will be in close contact with our clinical collaborators regarding the improvement of the robot and performance of the module.

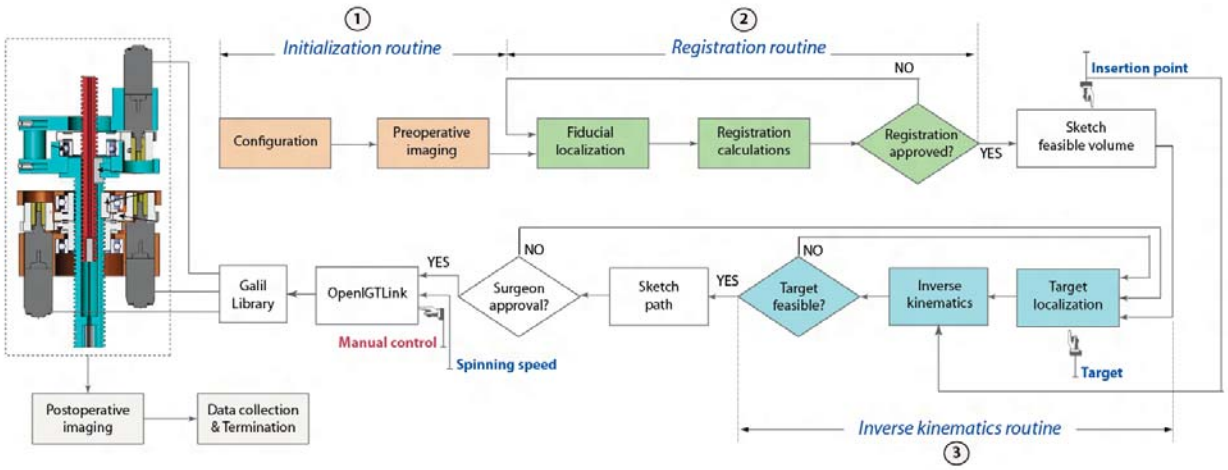

The image-guided system architecture embedded in 3D Slicer

Enhanced 3D Ultrasound Visualization for Guiding Beating Heart Procedures

Laura J. Brattain[1,2], Nikolay V. Vasilyev[3], Pedro J. del Nido[3], and Robert D. Howe[1]
[1]Harvard School of Engineering and Applied Sciences, Cambridge, MA USA 02138
[2]MIT Lincoln Laboratory, Lexington, MA USA 02420
[3]Department of Cardiac Surgery, Boston Children's Hospital, Boston, MA USA 02115

Purpose Real-time 3D ultrasound (3DUS) has distinct advantages for guiding minimally invasive beating heart procedures. It allows for visualization of complex 3D structures at a fast frame rate with good soft tissue contrast and it is portable and avoids the use of ionizing radiation. However, its limited resolution and field of view make it difficult for efficient clinical procedure navigation. Furthermore, volume-rendered images are often inadequate in distinguishing the tissue and tool contact. We developed a real-time visualization prototype system with enhanced displays to enable better 3DUS procedure guidance.

Methods The system consists of a 3DUS scanner imaging at 35Hz and 112 x 48 x 112 voxel per volume (iE33, Philips Healthcare, Andover, MA), a GPU enabled computer for real-time image processing and visualization and an electro-magnetic (EM) tracking system (Ascension Technology Corporation, Burlington, VT) for 3DUS probe and the catheter tip localization (Fig. 1). Using the ECG signal to gate the cardiac phase, the system performs real-time 4DUS volume mosaicing to generate an extended field of view. The catheter tip location is registered to the mosaiced volume, and orthogonal cut planes through the instrument tip are generated and displayed (Fig. 2).

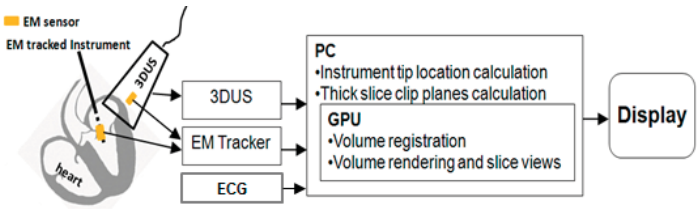

Fig. 1 System Overview

Results Five interventional cardiologists executed tracing and navigation tasks on a porcine heart in water tank under the guidance of 3DUS machine display or enhanced displays. The tasks simulate tool maneuvers in typical minimally invasive beating heart procedures. The user study shows a speed up of up to 50% in task completion time and smoother catheter tip trajectories with the guidance of slice views and slice views combined with mosiacing.

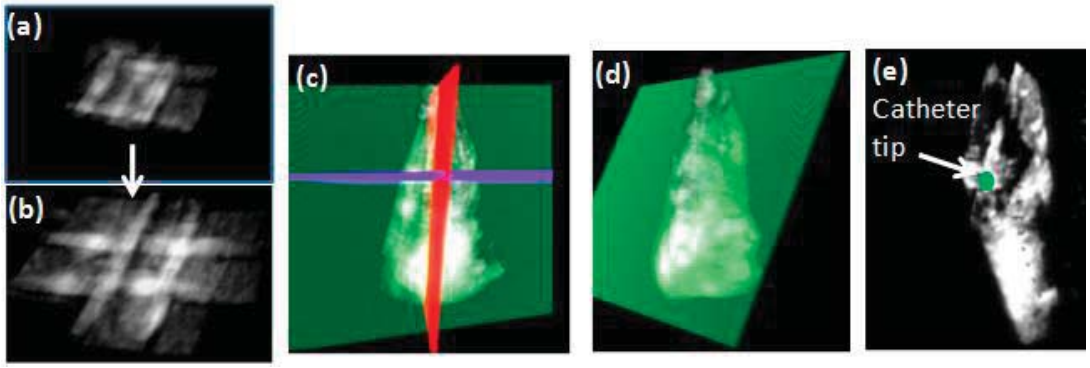

Fig. 2 Enhanced visualization. (a) Single 3DUS volume showing target rectangle. (b) Mosaiced 3DUS volume, note the wider field of view with better context. (c) Automatically generated orthogonal slice views through a catheter tip inside a porcine left atrium. (d) One slice view through the catheter tip. (e) 2D plane containing the catheter tip (in green) shows the details of the tip and tissue contact.

Conclusions A mosaiced volume overcomes 3DUS limited field of view and is applicable to a broad range of procedure guidance. Computer assisted tool tip tracking in slice views facilitates real-time instrument navigation and visual feedback in noisy 3DUS images. Our user study and participants' feedback demonstrate the potential of such enhanced visualization in effective procedure execution.

[1]Harvard University work is sponsored by US National Institutes of Health grant NIH R01 HL073647. MIT Lincoln Laboratory work is sponsored by the Department of the Air Force under Air Force contract #FA8721-05-C-0002. Opinions, interpretations, conclusions and recommendations are those of the authors and are not necessarily endorsed by the United States Government.

Ultrasound Volume Reconstruction: Open-Source Implementation with Hole Filling Functionality

Thomas Vaughan, Andras Lasso, and Gabor Fichtinger
Laboratory for Percutaneous Surgery, Queen's University, Kingston ON, Canada

Purpose: Ultrasound volume reconstruction is the process by which 3D ultrasound volumes are generated from a series of spatially tracked freehand 2D ultrasound images. Unfortunately, due to hand motion or rotational motion, the spacing between images is often irregular. If the grid resolution of the output volume is not low enough, holes can result from an inadequate image density, thereby rendering the volume unusable. The purpose of this work was to implement hole filling in free software for the reconstruction of high resolution ultrasound volumes that do not have holes.

Methods: We collected image data sets using a SonixTouch ultrasound scanner with L14-5 and EC9-5 transducers electromagnetically tracked with GPS extension (Ultrasonix, Richmond, BC, Canada). Images were inserted into volumes using reverse tri-linear interpolation [1]. For each image set, a ground truth volume was generated from a complete, dense set of images. We created test volumes with holes by skipping images during the image insertion phase, and then applying one of two hole filling methods, or no hole filling at all. The first method, the static size kernel method, filled holes with a weighted average of surrounding voxel intensities. The weight corresponded to a 3 x 3 x 3 voxel truncated gaussian spherical kernel centered on the hole voxel. The second method, the variable size kernel method, first attempted the static size kernel method, except if no voxel intensity information was contained in the 3 x 3 x 3 kernel region, a larger kernel was then tried instead of a 3 x 3 x 3 kernel. Progressively larger kernels would be tried in this fashion until either voxel intensity information was found, or some maximum kernel size was reached. All gaussian kernels in all methods were spherical and truncated such that 95% of the weight was retained. The hole filling was implemented in the free and open-source Public Software Library for Ultrasound (www.assembla.com/spaces/plus).

Results: Ultrasound volume reconstruction was performed on two image data sets – one of a spine phantom (using the L14-5 transducer) and one of a prostate phantom (using the EC9-5 transducer). Voxel intensities in holes from test volumes were compared to those from the ground truth to determine a mean absolute error for that test volume. Any unfilled holes were assumed to be completely black in the resulting reconstruction. A percentage error reduction was computed for test volumes that had holes filled compared against test volumes that did not have holes filled. Error reduction for the spine phantom reconstruction was 85.4% when using the static size kernel method, and 86.5% when using the variable size kernel method. Error reduction for the prostate phantom was 73.3% when using the static size kernel method, and 88.0% when using the variable size kernel method.

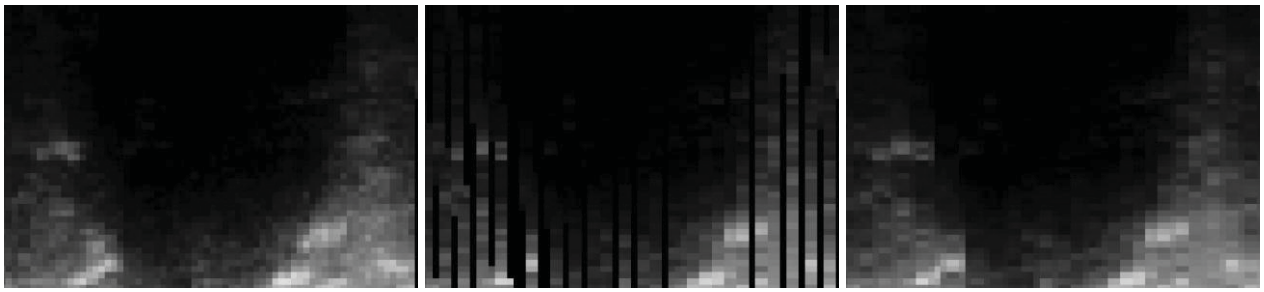

Figure: Spine phantom reconstruction slices; left, ground truth; center, test volume without hole filling; right, test volume with nearest neighbor gaussian kernel hole filling.

Conclusions: High-quality ultrasound volume reconstruction methods were implemented and made available for researchers as part of the free and open-source Public Software Library for Ultrasound. Hole filling was shown to greatly reduce the error in holes of reconstructed ultrasound volumes. Our results suggest that using a variable kernel size when there may be limited voxel information in the nearby region improves the accuracy of the final reconstruction.

[1] - Gobbi D. and Peters T. *Interactive intra-operative 3D ultrasound reconstruction and visualization.* Medical Image Computing and Computer Assisted Intervention 2002. **2489:**156-163, Springer.

Interventional Magnetic Resonance Imaging with an In-room Interactive Touch Device

M. A. Rube[1,2], B. F. Cox[1,2], A. B. Holbrook[3], L. Melzer[1], A. Melzer[1,2]

1. *Institute for Medical Science and Technology, Division of Imaging and Technology, University of Dundee, United Kingdom*
2. *Integrated Interventional Imaging Operating System (IIIOS), Marie Curie Initial Training Networks, Seventh Framework Programme, the People Programme*
3. *Department of Radiology, Stanford University, Stanford, California, United States*

Purpose:
To evaluate the practical aspects of an in-room interactive display and control device for the purposes of enhancing the operator's ability to track an interventional device's trajectory and alternate between slice orientations during near real-time interventions. The device was validated for percutaneous MRI guided needle interventions (biopsy).

Methods:
A phantom was utilized consisting of three dyed gelatine / agar / fat targets within a gelatine matrix. The interactive touch device (fig. 1a) was adapted from a tablet PC (iPad 1, Apple, Cupertino, US) and inserted in a sterile plastic cover. A wireless network connection was established with a modified router (DIR615, D-Link, Taipei, Taiwan) - One antenna was placed in the MR room and one outside providing a stable network connection throughout both areas. A real-time imaging feed was established via VNC connection. MR images were acquired in a closed bore 1.5T MR unit (Signa HDxt, GE Healthcare, Waukesha, US) with 8ch HD torso array coil employing fast gradient echo sequences (FGRE, TR / TE = 4 / 8 ms, FA 60°, FOV 330 x 330, slice 7mm, matrix 256 x 256). Biopsy samples were obtained with a biopsy needle (21G / 150 mm, Radimed, Bochum, Germany). Correct needle positioning was checked visually (fig. 1d) as well as verification of the coloured biopsy sample.

Results:
Fast parameter control (FA, slice, FOV) and slice repositioning (fig. 1b & 1c) while inserting the needle was achieved, facilitating fast device placement. The touch screen could be operated with gloves while covered in drape. No degraded image quality or RF interference could be detected on MR images or on a coherent noise test. No image distortions were observed on the tablet device from the magnetic fields at a distance > 30cm from the end of the bore. No displacement force are torque were present on the device at that distance.

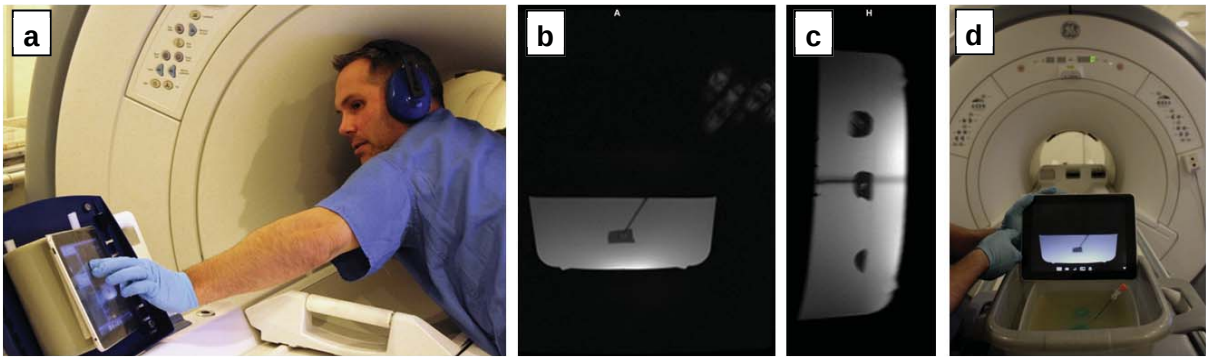

Figure 1 - MR guided needle biopsy: a) Adjustments of imaging slice b) Sagital real-time MR images with needle c) Double oblique orientation d) Successful needle puncture: Touch screen vs. visual inspection

Conclusions:
A concept for full wireless remote control of the MR scanner is being developed to facilitate MR guided interventions. Our in-room interactive device allows the operator up-close images (fig. 1d) and the ability to self-select a desired imaging axis instantaneously to better track needle progress. This is especially attractive in regards to needle path tracking in simultaneous orthogonal views towards the intended target. The close proximity of the touch device allowed precise target acquisition during simulated interventions.

Closed-Loop Commutator Control of an MRI-Powered Actuator

Christos Bergeles[1], Panagiotis Varthomoleos[1], Lei Qin[2], and Pierre E. Dupont[1]
[1]Boston Children's Hospital, Harvard Medical School, [2]Dana-Farber Cancer Research, Harvard Medical School

Purpose

Small motors that are powered, imaged and controlled by MRI scanners offer the potential to greatly expand the scope of MR guided interventions [1]. In this approach, the MRI scanner serves as the motor's stator while ferromagnetic material constrained within components of the actuator serves as the rotor. The rotor motion is transferred through a gear train to a translation stage that carries a needle (see Fig. 1). In all prior work, motor actuation was performed via open-loop control by applying gradients which cause the rotor to rotate [1]. In order to prevent the motor from slipping and also to maximize output torque, and, thus, output needle force, closed-loop control of the applied gradients is required [1].

Methods

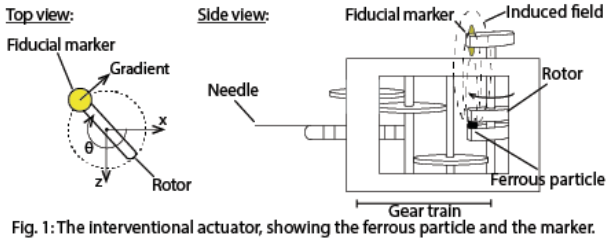

Fig. 1: The interventional actuator, showing the ferrous particle and the marker.

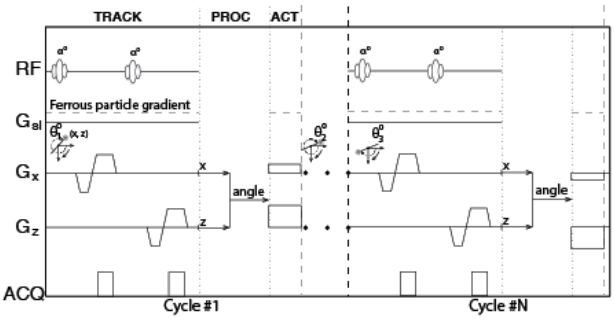

Fig. 2: Tracking (~15ms), processing (~2ms) and actuation (~150ms) sequences.

The goal of closed-loop rotor control is to always apply the field gradients in the direction that maximizes rotor torque as shown in Fig. 1. This necessitates real-time estimation of rotor angle. It is not possible, however, to image the actuator components with traditional scan sequences. Furthermore, the ferromagnetic material in the rotor distorts the surrounding B_0 field and, so, complicates direct imaging of any fiducial marker attached to the rotor. To overcome these challenges, Magnetic-Signature Selective Excitation is employed [2]. This technique, developed for real-time detection of ferrous particles *in vivo*, leverages the fact that water molecules affected by the field of a ferrous particle can be imaged using an RF frequency that corresponds to a higher gyromagnetic ratio, providing information on the location of the ferrous particle. Using simulation and experiment, it is demonstrated that a fiducial marker placed directly above the rotor so that they rotate synchronously (Fig. 1) can be imaged with an RF pulse of constant but reduced frequency (1200 Hz reduction). Any other positioning of the fiducial marker requires rotor-angle dependent radio frequencies.

Results

As shown in Fig. 2, the shifted RF pulse is used to excite the fiducial marker. The marker is localized using single-dimensional projections in the *x* and *z* axes, rotor angle is calculated and a gradient is applied orthogonal to rotor angle so as to generate maximum torque. Angles are estimated with an error of 5°. The estimation is unaffected by the presence of nearby tissue due to the RF frequency shift. Tracking is achieved in ~15ms (TRACK in Fig. 2), and actuation lasts for 150ms (ACT in Fig. 2), giving a high duty cycle of 86%. Processing and communication with the scanner lasts ~2ms (PROC in Fig. 2). Through closed-loop control of the gradient, slipping instabilities reported in [1] are avoided and the maximum output torque is constantly provided. This leads to an output force of ~1.0N, 130% the force achieved in open-loop [1].

Conclusions

Closed-loop control of MR-powered actuators allows the control of both motor position and torque. Such motors offer new design opportunities for MR-guided interventions such as biopsy and brachytherapy.

References

[1] P. Vartholomeos, L. Qin, and P. E. Dupont, "MRI-powered actuators for robotic interventions", Int. Conf. Intelligent Robots and Systems, 4508-4515, 2011.

[2] O. Felfoul, J.-B. Mathieu, G. Beaudoin, and S. Martel, "*In vivo* MR-tracking based on magnetic signature selective excitation", IEEE Trans. Medical Imaging, 27(1), 28-35, 2008.

Magnetic Resonance Imaging for Episcleral Plaque Brachytherapy

J. Esthappan, Y. Hu, C. Bertelsman, J. Garcia-Ramirez, and P. Grigsby

Washington University School of Medicine, Siteman Cancer Center, St. Louis, MO

Purpose: Use of ultrasound (US) and fundus photography is the current imaging standard for determining tumor involvement, location, and dimensions for uveal melanomas. From this information, episcleral brachytherapy isodose plans, based on the Collaborative Ocular Melanoma Study (COMS), are generated on two-dimensional (2D) models of a standard eye with anatomic structures, e.g., macula and optic disk, identified as points of interest in a single plane. We have developed a magnetic resonance (MR) imaging technique for patient-specific tumor and anatomic definition of the eye, and for three-dimensional (3D) COMS-based isodose planning.

Methods: Uveal melanoma patients were prescribed to receive 85 Gy over 96 hours from episcleral plaque brachytherapy using iodine-125 seeds. Plaque size and prescription depth were based on tumor basal dimensions and apex heights as determined by US and fundus photography. From this information, the source strength (uniform activity per seed) was determined. Prior to plaque implantation, patients were imaged on a 1.5-T Philips MR unit, with head coil in place, yielding T2-weighted (T2W) and T1-weighted (T1W) scans. Images were imported into a brachytherapy treatment planning system, initially fused to one another based on scanner coordinates, and then adjusted based on lens and optic nerve to account for movement of the eye between scans. Contouring of the tumor was largely based on the T2W scan, with reference to the standard measurements, but adjusted based on the T1W scan which in most cases provided improved definition of the tumor apex. Optic nerve, globe of the eye, and lens were also contoured on the T2W scan. Anatomic dose points normally defined in a single plane for the 2D plans, e.g., tumor apex, tumor anterior and posterior edges, macula, optic disk, lens, and retina, were re-defined on the MRI scans. Isodoses were computed on the T2W scan, with no inhomogeneity corrections, and point doses as well as dose-volume information were analyzed.

Results: For the T2W turbo spin echo (TSE) sequence, thirty-three 1.5 mm axial slices with no gap were acquired, echo time (TE) was 75 ms, repetition time (TR) was “shortest”, flip angle (FA) was 90°, and number of averages was 3. For the T1W 3D magnetization-prepared rapid acquisition with gradient echo (MPRAGE) sequence, eighty-three 1.2 mm slices were acquired. The TE, TR, FA and the number of averages were 4.0 ms, 8.5 ms, 8° and 1, respectively. For both scanning sequences, the in-plane voxel size was 1 mm × 1 mm, and the in-plane field-of-view was nominally 150 mm × 169 mm and adjusted slightly based on patient anatomy. Total scan time was approximately 4-5 minutes per sequence.

Conclusions: We have developed and clinically implemented an MR imaging technique for patient-specific tumor and anatomic definition of the eye, and for three-dimensional (3D) COMS-based isodose planning. Future work will be devoted towards using more advanced dose calculation methods to account for the effects of the gold backing and the silastic insert in our 3D COMS-based methodology. We believe the implementation of such methods for more accurate dosimetry will be critical for the proper determination of tumor dosing technique and the evaluation of risks associated with treatment-related morbidities.

Compact, Patient-Mounted MRI-guided Robot for Accurate Positioning of Multiple Cryoablation Probes

Faye Wu[1], Meysam Torabi[2], Alex Golden[2] , Michael Werner[2], Atsushi Yamada[3], Prof. Noby Hata[3], Hao Su[4], Greg Cole[4], Prof. Greg Fischer[4], Prof. Dan Frey[1], Prof. Conor Walsh[2], Dr. Kemal Tuncali[3]

1. Robust Design Lab, Mechanical Engineering Department, Massachusetts Institute of Technology
2. Harvard Biodesign Lab, Harvard School of Engineering and Applied Science, Wyss Institute for Biologically Inspired Engineering at Harvard University
3. Department of Radiology, Brigham and Women's Hospital
4. Automation and Interventional Medicine Robotics Research Lab, Worcester Polytechnic Institute

Purpose

To quantitatively validate the performance of a MR image-guided interventional robot that can place multiple probes using a newly-developed IGT module in 3D Slicer.

Methods

A patient-mounted guidance device for faster and more accurate targeting of multiple probes during cryoablation performed in closed bore magnetic resonance (MR) imaging systems was developed. An integrated 3D Slicer module allows for semi-automatic device registration as well as point and click targeting. The module connects to a Java program via OpenIGTLink to actuate and control two piezoelectric motors with closed loop inverse kinematics. Robot movement and order of probe placement are optimized to avoid probe collision. Using encoder feedback and forward kinematics, the position of a phantom probe is visualized in 3D Slicer in real time.

Results

Characterizing the device performance with still images taken before and after movement, the robot achieved sub-degree accuracy (less than 1 mm probe tip displacement), sub-degree repeatability near vertical position, and an incremental step resolution of 0.5 degree. Acceptable image deformation and noise validated the robot’s compatibility in MR environment.

Conclusions

As a proof of concept, this device demonstrates the feasibility of positioning multiple probes for MR image-guided percutaneous intervention. We will continue to develop the hardware and 3D Slicer module to further simplify the probe placement process and reduce targeting error.

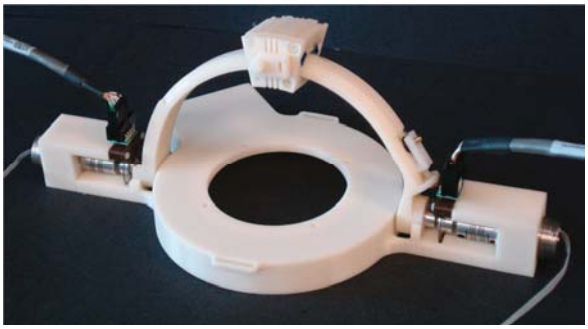

Title: 4D MRI for MRI-guided liver stereotactic body radiation therapy

Authors: T. Stanescu, T. Tadic, D. Jaffray

Motto: *"As a man is, so he sees. As the eye is formed, such are its powers." (William Blake)*

Purpose: To develop a 4D MRI method for the daily setup verification of liver patients treated with MRI-guided radiotherapy (i.e., MRIgRT).

Methods

Radiotherapy plays a pivotal role in the management of various types of cancer, approximately 50% of all cancer cases being treated with this modality. RT aims to accurately deliver lethal doses of x-ray radiation to the tumour target while sparing the adjacent healthy tissues. One of the key ingredients in achieving these objectives is high quality imaging, as it is vital to visualize and monitor the anatomy embedding the disease site. Due to its excellent soft-tissue contrast, MRI has proven to be the preferred imaging modality for the delineation of anatomical structures. The study proposes a novel 4D MRI technique for the daily pre-treatment patient setup verification and offline assessment of treatment delivery. The procedure is designed to be integrated in a workflow customized for an MRIgRT system consisting of a 1.5T Siemens Espree MRI scanner (goal: imaging) moving on rails to interact with a Varian TrueBeam linac (goal: treatment delivery) via a robotic patient table. The MRIgRT system is currently under installation at our institution.

4D MRI technique and benchmarking: The approach consists of multiple 2D cine acquisitions at sequential spatial locations, covering the desired volume of interest. Subsequently, 4D data is generated by means of sorting and binning of the image series as a function of organ motion amplitude/phase (e.g., due to breathing). Patient and volunteer data was acquired on a 3T Siemens Verio (Siemens Medical Systems, Erlangen, Germany) using a TurboFLASH sequence. The image sorting was performed based on sinograms generated by a) subsequently collapsing each image from individual 2D cine series into single pixel column along the sup-inf direction of organ motion and b) stacking these pixel columns into a 2D image map (i.e., sinogram). The pixels embedding information regarding local organ motion display in the sinogram a clearly defined oscillatory pattern. An alternative method investigated for generating the sinograms was to stack the information captured in individual pixel columns from image to image, part of the same series. For full volumetric characterization of motion, the analysis was expanded to all image columns. The amplitude/phase 3D volumes were generated by synchronizing the information resolved at each cine slice location.

Workflow for MRIgRT: Preliminary work was performed for the design of a liver SBRT process maps for the new MRIgRT platform, i.e., MRI on rails-linac. Two scenarios were considered: a) current clinical procedure relying on CT (planning) and 4D CBCT (guided delivery) as well as additional 4D MRI, and b) MRI-only for both planning and verification. The workflows included key steps such as: management of MR image distortions, 4D MRI pre-treatment, automatic segmentation, deformable registration and RT plan ranking. FMEA analysis of the workflow was also considered for the assessment of the proposed processes.

Results: The 4D MRI technique was successfully benchmarked against 2D cine MRI, 4D CT and 4D CBC by using data form liver patients treated with abdominal compression and free breathing. The system-related (i.e., B0 inhomogeneity, gradient non-linearities) and the patient-induced (i.e., susceptibility) distortions were determined and mitigated by means of phantom measurements and numerical simulations, respectively.

Conclusions: The proposed 4D MRI method is feasible for the quantification of tumor/organ motion and the daily patient setup verification of liver patients for an MRIgRT system (MRI on rails-linac). The technique is also expected to be used for the offline assessment of RT dynamic delivery.

Concurrent 12-Lead ECG & MRI Study of Acute Left Ventricular Ischemia Progressing to Death

Zion TH Tse[1], Charles L Dumoulin[2], Ronald Watkins[3], Kim Butts-Pauly[3], Israel Byrd[4], Jeffrey Schweitzer[4], Raymond Y Kwong[5], Gregory F Michaud[5], William G Stevenson[5], Ferenc Jolesz[6], Ehud J Schmidt[6]

[1]Engineering, The University of Georgia, Athens, GA, USA; [2]Radiology, Cincinnati Children's Hospital Medical Center, Cincinnati, OH, USA; [3]Radiology, Stanford University, Stanford, CA, USA; [4]Atrial Fibrillation, St Jude Medical Inc, St. Paul, MN, USA; [5]Cardiology,[6]Radiology, Brigham and Women's Hospital, Boston, MA, USA

Rapid detection of acute myocardial ischemia during MR imaging or MRI-guided therapy may improve acceptance of patients with ischemic histories. Visualizing ischemic episodes using MRI can also enhance the understanding of ischemic progression and improve therapy. Previously, an MR-compatible 12-lead ECG system was utilized to monitor patients with Premature Ventricular Contraction (PVC) and Atrial Fibrillation inside the MRI bore [1]. The system was equipped with MRI noise removal hardware and Magnetohydrodynamic (MHD) voltage-removal software that improved ST segment visualization. The study objective was to detect S-wave to T-wave (ST) ECG elevation and perform MR imaging of a Left Anterior Descending (LAD) balloon occlusion from the onset of ischemia to death in a swine model.

Methods: A 2-mm balloon catheter filled with Gadolinium-doped water was inserted into the swine's distal LAD using X-ray guidance. The swine was moved to a GE 1.5T MRI suite where continuous 12-lead ECG monitoring (Fig.A) and multiphase wall imaging (Fig.B-D) were performed. At t=0 seconds, the balloon was inflated to 20 atmospheres. MRI and simultaneous ECG monitoring were maintained until death around 20 minutes later. The balloon's position was confirmed using post-mortem 3D T1 imaging, and T2 imaging was used to detect edema.

Results and Conclusions: ST elevation was detected 1.5 seconds after onset (Fig.A1), progressing to acute ischemia (Fig.A2-3), bradycardia and death. Ventricular dysfunction and unusual flow vortexes were visualized with serial cine MRI (Fig.C1-4). Epicardial edema was observed adjacent to the balloon (Fig.D). The MR-compatible 12-lead ECG detects acute ischemia, while simultaneous MRI visualizing progression of dysfunction.

Ref.:[1] ZTH Tse, ISMRM '09-'11. Support: NIH U41-RR019703, R43 HL110427-01, AHA 10SDG261039

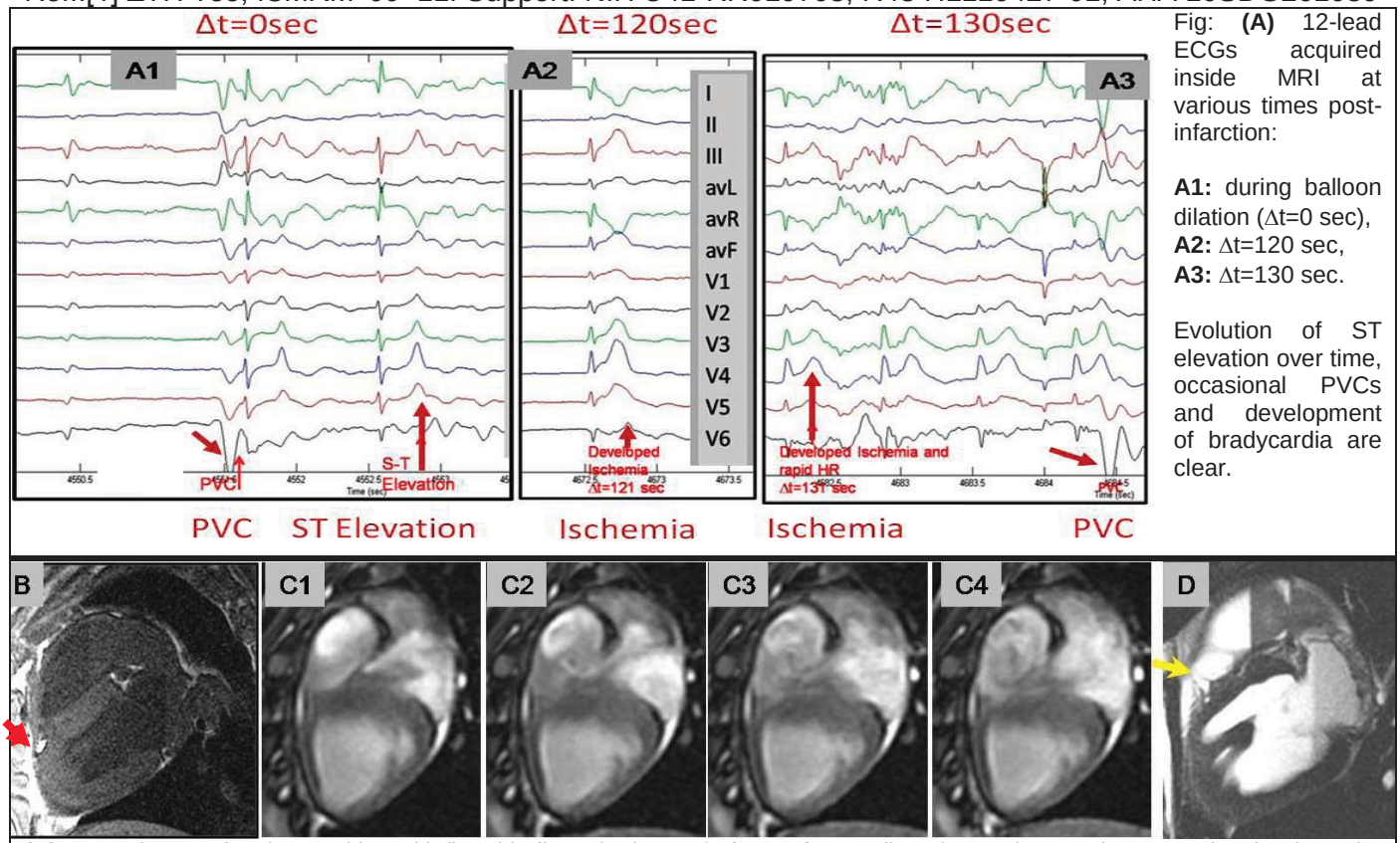

Fig: **(A)** 12-lead ECGs acquired inside MRI at various times post-infarction:

A1: during balloon dilation (Δt=0 sec),
A2: Δt=120 sec,
A3: Δt=130 sec.

Evolution of ST elevation over time, occasional PVCs and development of bradycardia are clear.

(B) 3D T1 image showing position of inflated balloon (red arrow). **(C1-C4)** 4 cardiac phases from a cine scan showing irregular flow patterns in the right ventricle during ischemia progression at Δt=120-140sec. **(D)** Post-mortem T2 image showing epicardial edema proximal to occlusion point (yellow arrow).

Swine Model Validation of Multimodality Cardiac Electrophysiology with an MRI-compatible Voltage-based Electroanatomic Mapping System

Zion TH Tse[1], Charles L Dumoulin[2], Israel Byrd[3], Jeffrey Schweitzer[3], Ronald Watkins[4], Kim Butts-Pauly[4], Raymond Y Kwong[5], Gregory F Michaud[5], William G Stevenson[5], Ferenc Jolesz[6], Ehud J Schmidt[6]
[1]Engineering, The University of Georgia, Athens, GA, USA
[2]Radiology, Cincinnati Children's Hospital Medical Center, Cincinnati, OH, USA
[3]Atrial Fibrillation, St Jude Medical Inc, St. Paul, MN, USA
[4]Radiology, Stanford University, Stanford, CA, USA
[5]Cardiology,[6]Radiology, Brigham and Women's Hospital, Boston, MA, USA

MRI produces images that serve as luminal, edema, and scar maps to assist in the electrophysiological (EP) treatment of ventricular and atrial arrhythmias [1]. An MR-compatible, voltage-based, Electroanatomic Mapping (EAM) system would allow registration-free EP procedures to occur outside of the MRI scanner during X-ray, Intra-Cardiac-Echo (ICE) or EAM guidance. In addition, MR-guided EP procedures might be improved using the system's voltage-based positional tracking during MR imaging, similarly to the benefits provided by MRI-based tracking.

The object of this study was to conduct a multi-catheter EAM (localization and intra-cardiac electrogram measurement) both inside and outside of the MRI scanner.

Methods: An MR-compatible cardiac mapping system was constructed to prevent MR gradient noise from reducing tracking accuracy. The system utilized a modified St. Jude Medical EnSite™ Velocity™ EAM system, electronic switching circuits, RF-filtered electrical lines, modified surface electrode patches, and MR-compatible EP catheters [2]. Trans-septal punctures were made in 5 intubated swine under X-ray/ICE guidance. The swine were moved to a GE 1.5T MRI suite equipped with the mapping system. Prior to the procedure, 3D ECG-gated MR Angiography (MRA) provided navigational roadmaps. Three voltage-tracked EP catheters were navigated simultaneously inside the MRI to acquire EAM of the heart's left and right sides, with a coronary sinus catheter providing a physiological reference (Fig.1). Imaging and voltage tracking were tested simultaneously (Fig.2). The swine were removed from the scanner and EP navigation continued without re-registration.

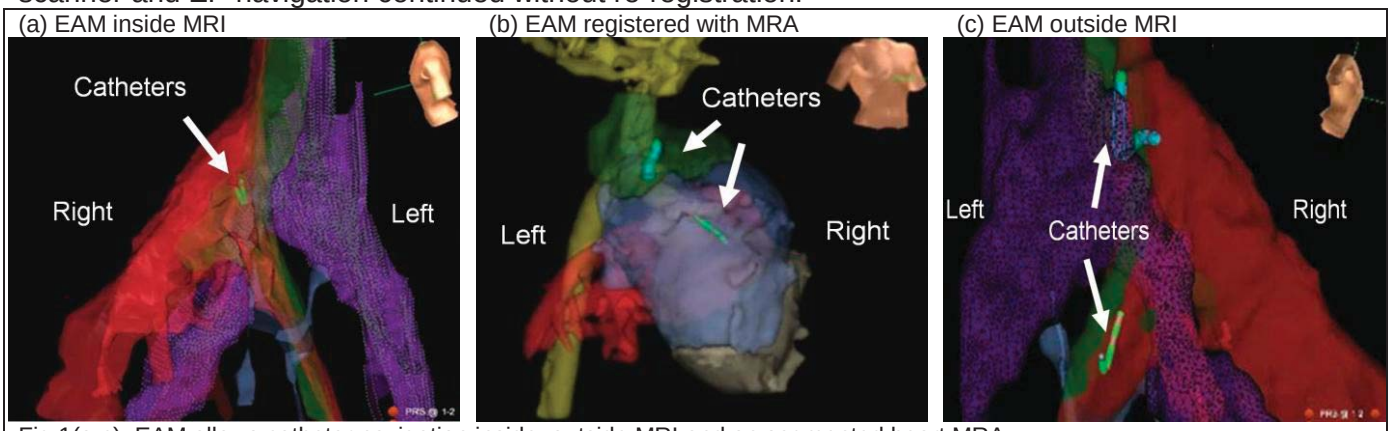

Fig.1(a-c): EAM allows catheter navigation inside, outside MRI and on segmented heart MRA.

Results & Conclusions: EAM and catheter navigation of the swine models were performed both inside and outside the MRI at >20 frames-per-second without re-registration (Fig 1). Positional differences of <3mm were found between the intra/extra MRI changes. Concurrent imaging and tracking (Fig. 2) were successful during sequences longer than 32 ms, capturing tissue during critical procedural stages. MR-compatible voltage tracking enables EP procedures to occur both in and out of the MRI without re-registration.

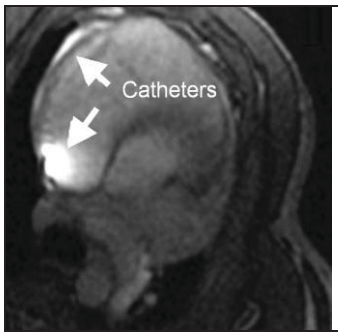

Fig.2 Concurrent MRI and voltage-based catheter tracking, showing catheters in the coronary sinus and the right atrium.

References: [1] CE Saikus JACC Img.'09, [2] ZTH Tse ISMRM'12
Acknowledgement: NIH U41-RR019703, R43 HL110427-01, AHA 10SDG261039

A Performance Evaluation Study of a Motorized Needle Guidance Template for MRI-guided Targeted Prostate Biopsy

Sang-Eun Song, Junichi Tokuda, Kemal Tuncali, Clare Tempany, Nobuhiko Hata

National Center for Image-Guided Therapy, Department of Radiology, Brigham and Women's Hospital, Harvard Medical School, 75 Francis Street, ASB1-L1-050, Boston, MA 02115, USA

Purpose To overcome the problems of limited needle insertion accuracy, prolonged procedural time, and human error in the use of a conventional needle guidance template in MRI-guided prostate interventions, we developed a motorized MRI-compatible needle guidance template that allows automated, gapless needle guidance in a 3-Tesla MRI scanner. To evaluate the motorized template, we conducted a performance evaluation study.

Methods We conducted a phantom experiment in a 3T MRI scanner to compare the needle insertion accuracy of the motorized template to that of a conventional template. We generated 20 random targets on an axial plane and performed needle insertions with each template. After needle insertion, a confirmation image was obtained using 2D turbo spin-echo (TR/TE = 2700/106 ms; acquisition matrix = 280 × 280; flip angle = 48º; field of view = 200 × 200 mm; slice thickness = 3 mm; receiver bandwidth = 252 Hz/pixel). From the confirmation image, a needle susceptibility artifact (signal void) was manually identified to localize the needle position in the phantom. Targeting accuracy was calculated as the distance between the center of the needle artifact and the aimed target in the images.

Phantom targeting test setup showing the motorized template in a 70 cm bore 3T canner.

Results The use of the conventional template with a 5 mm grid resulted in 2.2 mm root-mean-square (RMS) error, and the motorized template without an interval in 0.9 mm RMS error. A previous study reported that the targeting error in MRI-guided prostate biopsy using a conventional needle guidance template with 5 mm hole intervals resulted in a needle placement accuracy of 5.4 mm [1]. In this conventional template, if one of the holes coincides with a target position, the error should be minimal. If a target is at the center of the four neighboring holes, the maximum error, sqrt (2.5^2+2.5^2) = 3.53 mm, is expected.

Conclusions The study demonstrates that use of the motorized template's gapless needle placement results in greater needle insertion accuracy than the conventional needle template with 5 mm hole intervals. The motorized template's RMS error and the standard deviations of targeting errors in the x- and y-directions were equivalent or less than the pixel size of the confirmation image (0.875 mm); thus, the error was hardly noticeable on the confirmation image used in the ongoing MRI-guided prostate biopsy. The automated needle guide that is directly controlled by navigation software also eliminates human error so that the safety of the procedure can be improved.

[1] Tokuda J, Tuncali K, Iordachita I, Song SE, Fedorov A, Oguro S, Lasso A, Fennessy FM, Tempany CM, Hata N. In-bore Setup and Software for 3T MRI-guided Transperineal Prostate Biopsy, Physics in Medicine and Biology, *Accepted*

This project was supported by the National Cancer Institute, the National Center for Research Resources and the National Institute of Biomedical Imaging and Bioengineering of the National Institutes of Health through Grant Numbers 1R01CA111288, R01CA124377, 5R01CA138586, 5P01CA067165, P41EB015898 and P41RR019703; New Energy and Industrial Technology Development Organization Grant; Center for Integration of Medicine and Innovative Technology Grant 11-325.

Evaluation of Commonly Used Devices in the MR Environment

Ramon Martin, Karan Madan, Luigi Nascimben, Department of Anesthesiology, Perioperative and Pain Medicine, Daniel Kacher, Chang-Sheng Mei, Lawrence Panych, Department of Radiology, Brigham and Women's Hospital.

Purpose: The increasing use of Magnetic Resonance (MR) technology for diagnosis in hospitalized patients makes likely the interaction with devices that might not be listed in the Reference Manual for Magnetic Resonance Safety, Implants and Devices.[1] This report stems from a problem encountered with a patient who required a general anesthetic for a MR scan. Because of an unanticipated difficult intubation, a Fast Trach LMA was inserted. An endotracheal tube was placed through the LMA. During the MR scan, a large void was noted in the cervical region. Looking at another package, the endotracheal tube had a reinforcing wire along it's length. Because of this episode, several devices, which have no labels indicating their safety in the MR environment, are not listed in the Reference Manual for Magnetic Resonance Safety, Implants and Devices[1], but are commonly used in hospitalized/anesthetized patients were tested in a Siemens 3Tesla Verio magnet.

Methods: The standard test method for measurement of magnetically induced displacement force on medical devices in the magnetic resonance environment[2] was utilized. The method used for measuring temperature change was based on a standard method for assessing radiofrequency induced heating during magnetic resonance imaging [3].

Results: Table 1. Degrees of Deflection, Force and Temperature Change for Commonly Used Devices

Device	alpha(^{o})	Force=mg(tan alpha)	Temp Change (^{o}C)
Sheridan ETT	5	1.9458	0
LMA Fast Trach ETT	2	1.7475	0
Reinforced ETT	90	3.1769	0
Laser Shield ETT	90	4.9923	0
Laser Flex ETT	0	0	0
Arrow Central Line	30	2.0866	0
Edwards Swan Gantz	0	0	0
Edwards SG CCO	15	5.2146	0
Braun Epidural Cath	12	7.0912	0
Arrow Epidural Cath	0	0	0
Epimed Epidural Cath	90	4.5385	0
Medtronic Atrial Wire	90	4.5385	2
Medtronic Ventric Wire	90	4.4385	2

Conclusion: Of the devices tested, none are listed in the most recent edition of the Reference Manual for Magnetic Resonance Safety, Implants and Devices[1]. Only the Epimed epidural catheter is labeled as not safe for use in the MR environment. Several devices had deflections greater than 45^o, indicating that the magnetically induced deflection force is more than the force on the device due to gravity (weight). Except for the atrial and ventricular pacing wires, there was no change in temperature for these devices.

References:

1. FG Shellock Refernce Manual for Magnetic Resonance Safety. Implants and Devices. 2009 Edition. Los Angeles; Biomedical Research Publishing Group.
2. Standard Test Method for Measurement of Magnetically Induced Displacement Force on Medical Devices in the Magnetic Resonance Environment. West Conshohocken, PA; ASTM Int'l, F2052-06.
3. Standard Test Method for Measurement of Radio Frequency Induced Haeting On or Near Passive Implant During Magnetic Resonance Imaging. West Conshohocken, PA; ASTM Int'l, F2182-09.

Catheter Digitization on T2 MR for Interstitial Gynecologic Brachytherapy using a Hybrid MRI/CT Technique

Antonio Damato[1], Robert Cormack[1,3], Tina Kapur[2,3], Ehud Schmidt[2,3] and Akila Viswanathan[1,3]
[1]Department of Radiation Oncology, Division of Medical Physics and Biophysics, Brigham and Women's Hospital and Dana-Farber Cancer Institute, Boston, MA
[2]Department of Radiology, Brigham and Women's Hospital and Dana-Farber Cancer Institute, Boston, MA
[3]Harvard Medical School, Boston, MA

Purpose: Interstitial high-dose-rate (HDR) brachytherapy (ISB) is indicated for the treatment of advanced and recurrent gynecologic malignancies with significant vaginal and/or sidewall extension. The placement of interstitial catheters in close proximity to tumor tissue during insertion and the flexibility provided by HDR optimization allow for delivery of a high dose to the clinical target volume (CTV) while achieving acceptable sparing of the organs at risk (OARs). Catheter insertion is complicated by the difficulty of accurate and time-efficient identification of the CTV and OARs on a CT scan or ultrasound, and by the difficulty of providing real-time optimization of dwell loading. MRI guidance during ISB removes ambiguity in the delineation of the CTV and OARs, and has been successfully used to improve ISB through geometric assessment of catheter placement and adaptative repositioning or addition of catheters. However, catheters are less visible on MRI than on CT, and catheter digitization can become prohibitively time consuming and potentially inaccurate. We describe a technique for MRI catheter digitization for template-based ISB that does not require MRI dummy-markers and is time efficient and accurate.

Methods: Two patients were planned using this technique. A CT scan of the template and vaginal obturator was available. Catheters were inserted in the slots in the vaginal obturator with the tip exceeding the length of the obturator and standard CT dummies were used. The vaginal obturator was at its maximum insertion in the template. A gel was applied to the template to increase the visibility of 3 registration holes and of the empty catheter holes. A T2 MR with 1.6-mm slice thickness and a bSSSFP MR were acquired sequentially immediately after insertion without moving the patient between scans. The bSSSFP scan was intrinsically registered to the T2 MR and the two scans shared the same DICOM coordinates. The CT scan of the template and obturator was fused to the T2 MR based on template registration holes and empty catheter holes and on the angle of the vaginal obturator. All scans were reformatted to share the DICOM coordinates of the T2 MR and were imported into the Oncentra Brachytherapy Planning System for catheter digitization. Digitization was performed on axial slices and verified in sagittal and coronal slices. Each patient had a confirmatory CT scan after planning, 3-6 hours after extubation.

Results: On the T2 MR, the catheters in tissue were difficult to distinguish from vessels and other artifacts. The bSSSFP MR provided increased visibility of catheters in tissue, as seen with a blooming artifact by the catheter tip that increased the visibility of the catheter end. The fusion of T2 MR and bSSSFP MR sufficed to enable accurate digitization of the catheters in tissue. The catheters attached to the vaginal obturator along the obturator length, and all catheters for approximately the first 1 cm into tissue, were not visible. The CT scan was used to identify catheter location at the level of the template and along the vaginal obturator. Catheters along the vaginal obturator were digitized using CT only for the portion of the scan in which the vaginal obturator was visible in MR. Confirmatory CT showed a < 3 mm digitization discrepancy in the cranial-caudal direction, which is within the acceptable limits of our clinical practice.

Conclusions: We have developed a system to digitize catheters in an interstitial gynecologic application directly on MR, without the use of a patient CT scan or MR-specific dummy markers. This technique proved time efficient and accurate and has been implemented in our clinical practice.

Development of Real-time Intraoperative Image Fusion for Laparoscopic Surgery in Pediatrics

Xin Kang, PhD, Mahdi Azizian, PhD, Emmanuel Wilson, MS, Timothy Kane, MD, Craig Peters, MD, Raj Shekhar, PhD

Sheikh Zayed Institute for Pediatric Surgical Innovation
Children's National Medical Center, Washington DC, USA

Purpose: We present a real-time augmented reality (AR) system that fuses stereoscopic (i.e., 3D) laparoscopic video with laparoscopic ultrasound for guiding laparoscopic surgeries in children. It is generally accepted that overlaying intraoperative ultrasound images on laparoscopic video provides intuitive visualization of the intraoperative anatomy during minimally invasive surgeries. The result shows anatomical details inside soft-tissue organs and avoids having to mentally reconstruct the spatial relationship between an ultrasound image and the corresponding laparoscopic camera view. Although several research groups have studied this basic concept and reported proof-of-concept prototypes, no clinical system exists mainly because current implementations do not integrate seamlessly into the current operating room (OR) workflow and therefore remain insufficiently tested clinically. The goal of our development is to create an OR-ready system and to demonstrate its use in minimally invasive laparoscopic surgeries in pediatrics, and to evaluate its performance in the OR. In our implementation, we have addressed OR compatibility issues such as 3D visualization for superior depth perception, unobservable system latency, minimal OR setup time, and the re-use of highly accurate laboratory calibration results in the OR.

Methods: Our system includes two imaging devices: a stereoscopic vision system (VSII, Visionsense Corp) with pediatric-sized (5 mm) laparoscopes and an ultrasound scanner (flexFocus 700, BK Medical) with a standard (10 mm) laparoscopic transducer. Both systems are FDA approved for clinical use. Optical tracking is adopted in the current implementation to track the two instruments. The tracking information, together with streaming video from the stereoscopic laparoscope and the ultrasound scanner, is used to project the ultrasound image slice onto the temporally aligned 3D laparoscopic image pair on a real-time basis, thus creating two geometrically correct, ultrasound-augmented output video streams (one for the left eye and another for the right) for 3D visualization.

Results: Benefiting from the data-driven architecture and the minimal synchronizations of three streamed data sources, our system features a small latency (approximately 100 ms) in the creation of stereoscopic AR video. To minimize OR setup time and to be able to re-use highly accurate laboratory calibration results in the OR, purpose-designed mechanical fixtures are attached to the 3D laparoscope and the ultrasound probe. These fixtures attach to the instruments uniquely and serve as mounts for dynamic reference frames needed for optical tracking. This strategy maintains a fixed geometric relationship between the dynamic reference frames and the probes before and after sterilization. A 3D monitor is used to display the high-definition stereoscopic AR video with true depth perception. Fig. 1 shows exmaples of ultrasound augmented video images generated by our system in a phantom experiment and an animial study.

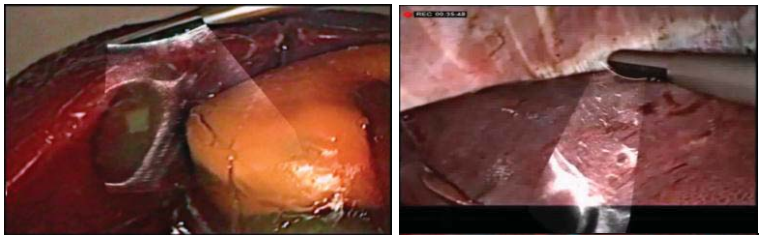

Fig. 1 Snapshots of AR images from a phantom experiment (left) and an animal study (right). Only one of the two channels available for stereoscopic visualization is shown here.

Conclusions: Our work has addressed and is addressing many key issues in developing a real-time, OR-ready, 3D AR visualization system for laparoscopic surgery in children. It has been used successfully in the laboratory and in an animal study. Following additional system refinement, the system will be tested clinically. Augmented reality visualization, especially when supported with true depth perception, promises to greatly enhance the precision of current-generation pediatric laparoscopic surgeries while enabling new ones.

Pituitary Adenoma Segmentation Using the Medical Image Computing Platform *3D Slicer*

Jan Egger, Ph.D., Ph.D.[1,2,3], Tina Kapur, Ph.D.[1], Christopher Nimsky, M.D., Ph.D.[3], Ron Kikinis, M.D.[1]

[1] Dept. of Radiology, Surgical Planning Lab, Brigham and Women's Hospital Boston, MA, USA, [2] Dept. of Mathematics and Computer Science, University of Marburg, Marburg, Germany, [3] Dept. of Neurosurgery, University of Marburg, Marburg, Germany

Purpose – Tumors of the sellar region, mainly pituitary adenomas, represent 10% to 25% of all intracranial neoplasms, with adenomas comprising the largest portion with an estimated prevalence of approximately 17% [1, 2]. These adenomas can be classified according to many criteria including size, histological characteristics, and hormone secretion (hormone active and hormone-inactive). Microadenomas are less than 1 cm in diameter, whereas macroadenomas measure more than 1 cm. Typically for macroadenomas with mass-effect, transsphenoidal surgery is the treatment of choice [3]. By contrast, hormone-inactive microadenomas are closely monitored using endocrine and ophthalmological evaluations as well as magnetic resonance imaging (MRI). Microsurgical excision is performed if the tumor volume increases over time. Image analysis that includes segmentation and registration of these successive scans is beneficial in the accurate measurement of tumor progression.

Methods – We performed segmentation of pituitary adenomas on T1- and T2-weighted images acquired on a *MAGNETOM Sonata* 1.5 T MRI scanner (*Siemens Medical Solutions, Erlangen, Germany*) equipped with a standard head coil. The segmentation method we used is the *GrowCut* implementation [4] in *3D Slicer* (or *Slicer*) which is freely downloadable from the website http://www.slicer.org. *GrowCut* [5] is an interactive segmentation algorithm based on the idea of cellular automata. The algorithm achieves reliable and fast segmentation of moderately difficult objects in 2D and 3D using an iterative labeling procedure resembling competitive region growing. After trial of the various segmentation facilities available in *Slicer*, we determined that the use of *GrowCut* by initializing it on sagittal, axial, and coronal cross-sections provides the most efficient segmentations. In this initialization step, parts of the tumor and parts of the background are marked on the image with the *Slicer* brush tool. The figure above shows a typical initialization of a pituitary adenoma (blue) and the background (brown) on an axial slice.

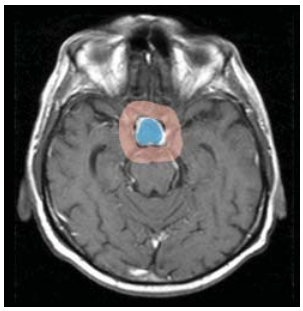

Results – The goal of this study was to evaluate the utility of *Slicer* for segmentation of pituitary adenomas. To evaluate the utility of *Slicer*, ground truth was provided by manual slice-by-slice segmentation of five pituitary adenomas by neurological surgeons with several years of experience in resection of pituitary adenomas. These manual segmentations were compared with the *Slicer* segmentation results of the proposed method via the *Dice Similarity Coefficient (DSC)* [6]. Briefly, the *DSC* measures the relative volume overlap between *M* and *S*, where *M* and *S* are the binary masks from the manual slice-by-slice (*M*) and the *Slicer* (*S*) segmentation. The average *DSC* for all data sets was 81.71%±4.78% and shows that the two are comparable. The figures on the right present segmentation results on a sagittal (upper row) and an axial (lower row) slice for the manual segmentation (middle images, yellow) and the *Slicer* segmentation (right images, magenta).

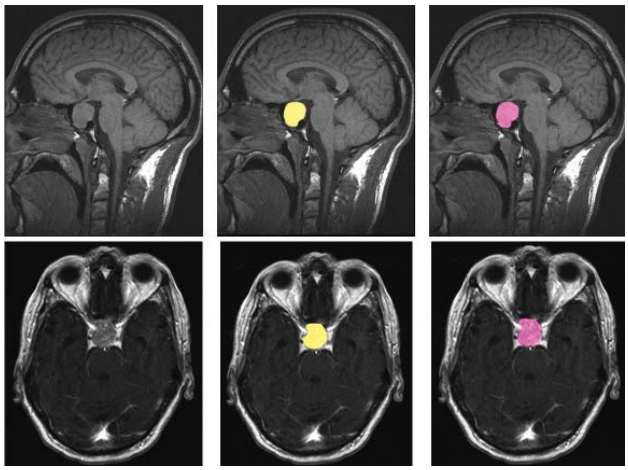

Conclusions – In this contribution, we present segmentation results for pituitary adenoma in MRI data using the medical platform *3D Slicer* and showed that it is valuable to support the time-consuming process of volumetric assessment. The time and user effort required for *GrowCut* segmentation was on an average 50% compared to pure manual segmentation. There are several areas of future work including comparison with graph-based based segmentation methods such as [7, 8].

Acknowledgements

We acknowledge the members of the *Slicer* Community and in particular Steve Pieper for their contributions, and moreover Harini Veeraraghavan and Jim Miller from GE for developing the *GrowCut* module in *Slicer*. Furthermore, the authors would like to thank the physicians Dr. med. Daniela Kuhnt, Dr. med. Barbara Carl, Christoph Kappus and Rivka Colen, M.D. for participating in this study. This work was supported by National Institutes of Health (NIH) grant P41EB015898.

References

[1] http://www.cancer.gov/cancertopics/pdq/treatment/pituitary/HealthProfessional/page1/AllPages#1 (last accessed: July 2012)
[2] M.- A. Weber, et al., Sellar tumors (in German), Der Radiologe; 47(6):492-500. Springer Berlin / Heidelberg, 2007.
[3] M. Buchfelder and S. Schlaffer, Surgical treatment of pituitary tumours, Best Pract Res Clin Endocrinol Metabol; 23(5):677-92, 2009.
[4] GrowCut-Module under 3DSlicer http://www.slicer.org/slicerWiki/index.php/Modules:GrowCutSegmentation-Documentation-3.6
[5] V. Vezhnevets and V. Konouchine, GrowCut - Interactive multi-label N-D image segmentation, in Proc. Graphicon, pp. 150-156, 2005.
[6] K. H. Zou, et al., Statistical Validation of Image Segmentation Quality Based on a Spatial Overlap Index: Scientific Reports, Academic Radiology, 11(2), pp. 178-189, 2004.
[7] J. Egger, et al., Pituitary Adenoma Segmentation, Proc. of International Biosignal Processing Conference, Berlin, Germany, 1-4, 2010.
[8] J. Egger, B. Freisleben, C. Nimsky, T. Kapur, Template-Cut: A Pattern-Based Segmentation Paradigm, Nature - Scientific Reports, Nature Publishing Group (NPG), 2(420), 2012.

Capability of the Medical Image Computing Platform *3D Slicer* for Glioblastoma Multiforme Segmentation in Magnetic Resonance Imaging (MRI) Data

Jan Egger, Ph.D., Ph.D.[a,b,c], Tina Kapur, Ph.D.[a], Andriy Fedorov, Ph.D.[a], Steve Pieper Ph.D.[a,d], James V. Miller, Ph.D.[e], Harini Veeraraghavan, Ph.D.[f], Bernd Freisleben, Ph.D.[c], Alexandra J. Golby, M.D.[a,g], Christopher Nimsky, M.D., Ph.D.[b] and Ron Kikinis, M.D.[a]

[a] Dept. of Radiology, Surgical Planning Lab, Brigham and Women's Hospital Boston, MA, USA, [b] Dept. of Neurosurgery, University of Marburg, Marburg, Germany, [c] Dept. of Mathematics and Computer Science, University of Marburg, Marburg, Germany, [d] Isomics, Inc., Cambridge, MA, USA, [e] Interventional and Therapy Lab, GE Research, Niskayuna, NY, USA, [f] Biomedical Image Analysis Lab, GE Research, Niskayuna, NY, USA, [g] Dept. of Neurosurgery, Brigham and Women's Hospital, Harvard Medical School, Boston, MA, USA

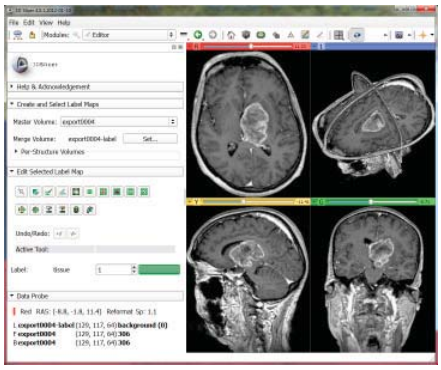

Purpose – Gliomas are the most common primary brain tumors, evolving from the cerebral supportive cells. The World Health Organization (WHO) grading system for gliomas defines grades I-IV, where grade I tumors are the least aggressive and IV are the most aggressive [1]. 70% belong to the group of malignant gliomas (anaplastic astrocytoma grade III, glioblastoma multiforme grade IV). The glioblastoma multiforme, named for its histopathological appearance, is the most frequent malignant primary tumor and is one of the most highly malignant human neoplasms. Volumetric change in grade IV tumors (glioblastoma multiforme (GBM)) over time is a critical factor in treatment decisions by physicians. Typically, the tumor volume is computed on a slice-by-slice basis using MRI patient scans obtained at regular intervals. In this contribution we investigated the capability of the medical image computing platform *3D Slicer* for the segmentation of GBMs.

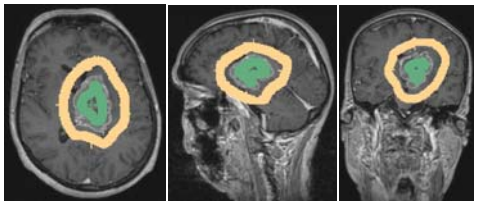

Methods – For this study, we used the *GrowCut* [2] software module in *3D Slicer* [3], which is freely downloadable from the website http://www.slicer.org. The upper image shows the 3D *Slicer* interface with the *Editor* on the left side and a loaded GBM data set on the right side: axial slice (upper left window), sagittal slice (lower left window), coronal slice (lower right window) and the three slices shown in a 3D visualization (upper right window). A typical user initialization of *GrowCut* under *Slicer* for the segmentation of a GBM is presented in the three images on the right side: axial (left image), sagittal (middle image) and coronal (right image). Note: the tumor has been initialized in green and the background has been initialized in yellow.

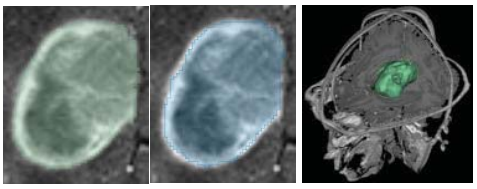

Results – In this study, four physicians segmented GBMs in ten patients, once using the competitive region-growing based *GrowCut* segmentation module of *3D Slicer*, and once purely by drawing boundaries completely manually on a slice-by-slice basis. The time and user effort required for *GrowCut* segmentation was on an average 25% compared to pure manual segmentation. A comparison of *Slicer* based segmentation with manual slice-by-slice segmentation resulting in a *Dice Similarity Coefficient* [4] of 88.43±5.23% and a *Hausdorff Distance* of 2.32±5.23mm shows that the two are comparable. The two left images of this section show a comparison of GBM segmentation results on an axial slice: semi-automatic segmentation under *Slicer* (green, left image) and pure manual segmentation (blue, middle image). The right image presents a 3D segmentation result of *GrowCut* (green). After the initialization of the *GrowCut* algorithm under *Slicer* it took about ten seconds to get the segmentation result on an *Intel Core i7-990 CPU, 12x3.47 GHz, 12 GB RAM, Windows 7 Home Premium x64 Version, Service Pack 1*.

Conclusions – In this study we evaluated the capability of *3D Slicer* for segmentation of GBMs compared to manual slice-by-slice segmentation. As a metric for our evaluation we used the agreement between slice-by-slice and *Slicer* segmentations to show that *Slicer* can be used to produce GBM segmentations that are statistically equivalent to what the physicians achieve manually in fraction of the time (0.25). Areas of future work include a direct comparison of the *Slicer*-based segmentation with a graph-based algorithm [5], and extension to multi-modal images.

Acknowledgements

The authors want to thank the members of the Slicer Community for their contributions and furthermore the physicians Dr. med. Daniela Kuhnt, Dr. med. Barbara Carl, Christoph Kappus and Rivka Colen, M.D. for participating in this study. This work was supported by National Institutes of Health (NIH) grant P41EB015898.

References

[1] P. Kleihues, et al., The WHO classification of tumors of the nervous system, Journal of Neuropathology & Experimental Neurology; 61(3):215-229, 2002.
[2] V. Vezhnevets and V. Konouchine, GrowCut - Interactive multi-label N-D image segmentation, in Proc. Graphicon, pp. 150-156, 2005.
[3] GrowCut-Module under 3DSlicer http://www.slicer.org/slicerWiki/index.php/Modules:GrowCutSegmentation-Documentation-3.6
[4] K. H. Zou, et al., Statistical Validation of Image Segmentation Quality Based on a Spatial Overlap Index: Scientific Reports, Academic Radiology, 11(2), pp. 178-189, 2004.
[5] J. Egger, B. Freisleben, C. Nimsky, and T. Kapur, Template-Cut: A Pattern-Based Segmentation Paradigm, Nature - Scientific Reports, Nature Publishing Group (NPG), 2(420), 2012.

Intraoperative Endoscoping Margin Evaluation for Prostate Resection Robotic Surgery.

Alex Hartov, John Seigne, John Heaney, Yuqing Wan, Ryan Halter.

Abstract

The primary objective of this work is to develop and characterize an intraoperative tool for detecting and identifying prostate cancer at surgical margins using the bioelectrical properties of tissue to distinguish malignant from benign tissues. In this report we present a virtual instrument that makes it possible to display the assessed state of tissues at sampled regions of interest inside the surgical field using augmented reality technology. In a collaboration involving engineers from the Thayer School of Engineering at Dartmouth College and surgeons from the Dartmouth Medical School, we are developing software and hardware systems that will provide 3D and real-time data visualization to the surgeon while operating on a da Vinci robotic surgical station. Taking advantage of the stereoscopic view afforded to the surgeon, we can capture this video stream and reconstruct a 3D profile of the scene as viewed by the surgeon using stereo-vision techniques. Using that same technology, we can create visual overlays exploiting stereopsis which will place color coded patches at points sampled by our custom probe and indicate if the measurements reveal a negative or positive surgical margin. We hope that this method of direct and visually localized feedback to the surgeon will improve surgical outcomes by detecting positive margins in situ and at the time of surgery.

Probabilistic deformation atlases for atlas-based registration and segmentation

John A. Onofrey[1], *Lawrence H. Staib*[1,2,3] and *Xenophon Papademetris*[1,2]
Departments of [1]Biomedical Engineering, [2]Diagnostic Radiology, and [3]Electrical Engineering
Yale University, New Haven, CT, USA

PURPOSE For image-guided interventions that require the delineation of specific structures of interest, automated atlas-based segmentation approaches have been proposed to avoid labor-intensive, manual labeling. Accurate image registration is crucial for accurate segmentation. However, registration is ill-posed due in part to anatomical variations between the subject and the atlas, and to nonrigid deformations, which subsequently lead to inaccuracies. The goal of this work is to develop a framework for creating a probabilistic deformation atlas. Whereas other probabilistic atlases are statistical in terms of the labeling, we propose an atlas with statistics of the deformation. We leverage existing "gold-standard" manual segmentations to create a set of "gold-standard" nonrigid registrations, from which we statistically characterize the nonrigid deformations of the group. The "gold-standard" registrations can additionally be used to create a "gold-standard" mean atlas. We present results using a database of labeled MR brain images.

METHODS The UCLA LONI Probabilistic Brain Atlas (LPBA) database [1] contains 40 normal subjects each with 56 manually-labeled volumes of interest (VOI) and tissue classification labels. We converted the labeled volumes to point-based surfaces. After selecting one subject as an initial reference, we registered the 39 remaining images first using an affine registration to the brain surface and then using an integrated intensity and point registration algorithm [2] with an FFD deformation model [3]. For the intensity component, rather than using the raw MR intensity images, we made use of the tissue label images to avoid intersubject intensity inhomogeneities. To remove any bias toward the initial reference subject, we computed the mean deformation and applied the inverse mean transformation to the initial reference image and surface. We then reran the integrated registrations using this new, bias-corrected reference. We quantified registration accuracy by computing the Dice overlap of the 56 VOIs. We qualitatively compared the registrations by computing mean and standard deviation intensity images of the registered, intensity-normalized, LPBA bias field-corrected, skull-stripped images.

RESULTS Using our nonrigid registration method improved both VOI overlap as well as correlation coefficient similarity measure. The mean Dice overlap improved for all 56 labeled VOIs with standard deviation being reduced in all but 2 VOIs compared to affine registration. The correlation coefficient (mean±std) for the registered images improved from 0.958±0.004 with affine registration to 0.974±0.003 using VOI point-based registration, and to 0.994±0.001 with integrated registration. Qualitatively, our "gold-standard" atlas appears much sharper than previously published atlases [1], indicating good structural correspondences. The figure below illustrates the improved registration by showing mean and standard deviation images at three stages of the registrations process.

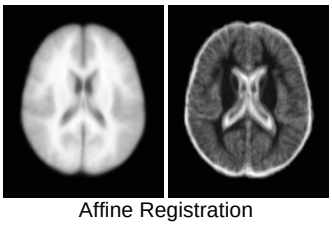
Affine Registration

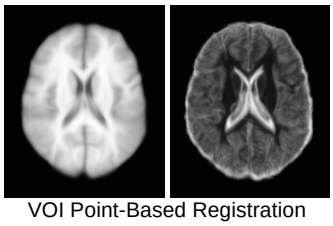
VOI Point-Based Registration

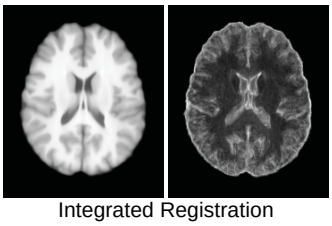
Integrated Registration

CONCLUSIONS Our atlas can be used as a reference image for spatial normalization and as a statistical prior for registration. We aim to use the deformation statistics to constrain future registrations as well as characterize registration uncertainty.

REFERENCES

[1] Shattuck, et al. Construction of a 3D probabilistic atlas of human cortical structures. NeuroImage, 2008.
[2] Papademetris, et al. Integrated Intensity and Point-Feature Nonrigid Registration. MICCAI, 2004.
[3] Rueckert, et al. Nonrigid registration using free-form deformations: application to breast MR images, IEEE Trans. on Medical Imaging, 1999.

Image-based Tracking of Deflected Needle for Complex MR Images in MRI-guided Percutaneous Interventions

Atsushi Yamada, Junichi Tokuda, Nobuhiko Hata

Surgical Navigation and Robotics Laboratory, Brigham and Women's Hospital, Boston, MA, US

Purpose

Needle deflection disturbs placing needle following the planned trajectory in magnetic resonance imaging (MRI) -guided biopsies and ablation therapies. The deviation from the planned trajectory due to the needle deflection may consequently lead to misdiagnosis or mismanaged treatment. In particular, deflected needle around complex textures of soft tissues in real-time imaging plane is potentially prone to lose the tip, leading to not only the inaccuracy of diagnosis and treatment but damages to the tissues and anatomies around the tip of the needle. The contribution of the paper is to develop and validate our method to detect tip of deflected needle in real-time MR images by separating the tip image from complex textures of soft tissues around the needle to track the tip of the deflected needle robustly.

Methods

We developed an image processing method to track the tip of a deflected needle in a real-time MR image robustly that presents complex texture of soft tissues around the needle. The tip of the needle is tracked by line detection assisted by a Lucas-Kanade approach of optical flow method to separate the tip image from complex textures of soft tissues around the needle. The line detection is possible by Hough transformation that predicts the best candidate of the tip of the needle from image artifacts. The Lucas-Kanade approach complements the needle detection to digitize the tip of the needle by computing dynamic information of the needle and deformation of the soft tissues around the needle to limit candidate of the tip of the needle. Two sets of experiments were performed to validate the method. The first set of the study involved a gelatin phantom to measure the accuracy of the needle detection, using real-time MR images of an 18G biopsy needle (DAUM GmbH Biopsienadel, Schwerin, Germany). The phantom was imaged using TrueFISP (TR/TE: 3.96/1.98ms; Matrix size: 128×128; Flip angle: 45 deg.; FOV: 200×200mm^2, In-plane pixel size: 1.6x1.6mm^2; Pixel bandwidth 908 Hz / pixel; acquisition time: approx. 0.5s) on 3T MR scanner (MAGNETOM Verio, Siemens Healthcare, Erlangen, Germany). Accuracy of needle tip detection was measured. The second half of the study used the clinical data collected in MRI-guided prostate biopsy to evaluate the feasibility of the method in the clinical setting. The computation time to process each scanned image for needle tracking also recorded.

Results

The needle tip was successfully detected and tracked both in the phantom study and the clinical study, regardless of deflected directions, and existences of complex tissue textures around the tip of the needle. The errors between the tracked tip position and the physical tip position for each imaging plane in the phantom study was 4.3±0.7mm. Mean computation time was 0.12 s / image.

Conclusions

The study shows that the proposed image-based tracking method has a potential to track the tip of the deflected needle robustly in complex tissue textures without any specific tools in MR-guided biopsies and ablation therapies. The computation time to process each scanned MR image is enough to track the tip of the needle in real-time.

Acknowledgements: This work is supported by NIH grants R01CA124377, R01CA138586, and P41EB015898.

Prostate Central Gland Segmentation Using a Spherical Template Driven Graph Approach

Jan Egger, Ph.D., Ph.D.[1,2,3], Tobias Penzkofer, M.D.[1,4], Tina Kapur, Ph.D.[1], Clare Tempany, M.D.[1]

[1] Dept. of Radiology, Surgical Planning Lab, Brigham and Women's Hospital Boston, MA, USA, [2] Dept. of Mathematics and Computer Science, University of Marburg, Marburg, Germany, [3] Dept. of Neurosurgery, University of Marburg, Marburg, Germany, [4] Dept. of Diagnostic and Interventional Radiology, RWTH Aachen University Hospital, Germany

Purpose – Prostate cancer is the most abundant cancer in men, with over 240,000 expected new cases and around 28,000 deaths in 2012 in the US alone [1]. Accurate risk stratification for each individual cancer is central to a successful treatment strategy, especially because of the high incidence rate of less aggressive prostate cancers, and the high complication rate of radical prostatectomy. Diagnostic prostate magnetic resonance imaging (MRI) and MRI guided prostate biopsies have demonstrated improved diagnostic discrimination rates of the different types of cancer [2]. Our goal is to enhance the state of the art in automated segmentation (i.e. delineation) of organ limits for the prostate, a step that has been shown to facilitate efficient MR-guided biopsy.

Methods – The *Nugget-Cut* scheme [3] was used for prostate center gland segmentation on 5 datasets [4]. It sets up a directed 3D-graph *G(V,E)* in two steps: (I) sending rays through the surface points of a polyhedron and (II) sampling the graph's nodes $n \in V$ along every ray (Figure 1). Additionally, a corresponding set of edges $e \in E$ is generated, which consists of edges between the nodes and edges that connect the nodes to a source *s* and a sink *t*. After graph construction – the center of the polyhedron was defined by the user and located inside the prostate center gland – the minimal cost closed set on the graph is computed via a polynomial time *s-t-cut* [5], which results in the segmentation of the prostate center gland's boundaries and volume. A C++ module was implemented within the medical prototyping platform MeVisLab (see http://www.mevislab.de) for evaluation. Results were compared to an expert segmentation using the Dice Similarity Coefficient (DSC).

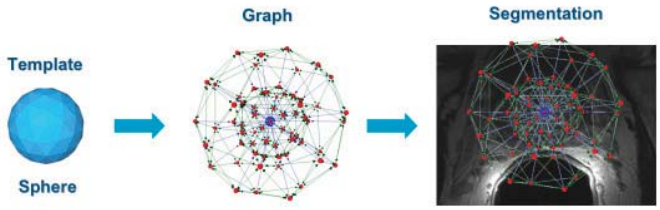

Fig 1. Nugget-Cut Scheme: A template is used as a basic structure for the segmentation graph

Results – A DSC of 85 ± 6.0% overlap was achieved compared to expert segmentation. This is an improvement on recent 80% DSC reported in the literature [6]. In our C++ implementation the overall segmentation: (1) sending rays, (2) graph construction and (3) *mincut* computation, took about one second on *an Intel Core i7 CPU, 4x2.50 GHz, 8 GB RAM*. Figure 2 shows the segmentation result of a prostate central gland (red) on an axial and a sagittal 2D slice with the typical user-defined seed point position on the axial slice (blue arrow) located inside the organ.

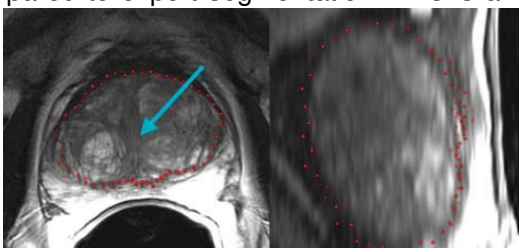
Fig 2. Segmentation results in axial and sagittal reformatting (blue arrow: seed point)

Conclusions – In this abstract, we present segmentation results for the prostate gland in MRI data using a recently developed method. A graph driven method has been used that is based on a spherical template. The algorithm prefers spherically- and elliptically-shaped 3D objects and has already been evaluated with glioblastoma multiforme, pituitary adenoma and cerebral aneurysm data [7]. There are several areas of future work including comparison with level-set based prostate segmentation methods such as [8], extensions for automatic segmentation of structures adjacent to the central prostate gland, such as the peripheral prostatic zone. An immediate next application for MR-guided biopsy is the generation of regions of interest towards automatic registration of preoperative to intraprocedural images.

Acknowledgements

We acknowledge the help of Drs. Fedorov, Tuncali, Fennessy and Tempany for sharing the provided data collection. This work is supported by NIH 8P41EB015898-08 and 5P01CA067165-13. Its contents are solely the responsibility of the authors and do not necessarily represent the official views of the NIH.

References

[1] National Institutes of Health Cancer Topics: Prostate, http://www.cancer.gov/cancertopics/types/prostate
[2] D'Amico AV, Cormack RA & Tempany CM. *MRI-Guided Diagnosis and Treatment of Prostate Cancer.* N Engl J Med. 344:776-777, 2001.
[3] Egger J, et al. *Nugget-Cut: A Segmentation Scheme for Spherically- and Elliptically-Shaped 3D Objects*. In: 32nd Annual Symposium of the German Association for Pattern Recognition (DAGM), LNCS 6376, pp. 383-392, Springer, 2010.
[4] Fedorov A, et al. *Image Registration for Targeted MRI-guided Prostate Transperineal Prostate Biopsy*. J Magn Res Imag, 2012.
[5] Boykov Y & Kolmogorov V. *An Experimental Comparison of Min-Cut/Max-Flow Algorithms for Energy Minimization in Vision*. IEEE Transactions on Pattern Analysis and Machine Intelligence, 26(9), pp. 1124-1137, 2004.
[6] Yin Y, et al. *Fully automated 3D prostate central gland segmentation in MR images: a LOGISMOS based approach*. Proc. SPIE 8314, 83143B, 2012.
[7] Egger J, et al. *Template-Cut: A Pattern-Based Segmentation Paradigm*. Nature - Scientific Reports, Nature Publishing Group, 2(420), 2012.
[8] Tsai A, et al. *A shape-based approach to the segmentation of medical imagery using level sets*. IEEE TMI, 22(2), pp.137-154, 2003.

Graph-Based Vertebra Segmentation Using a Cubic Template

Robert Schwarzenberg [a,b], Tina Kapur, Ph.D.[a], William Wells, Ph.D.[a], Christopher Nimsky, M.D., Ph.D.[c], Bernd Freisleben, Ph.D.[b], Jan Egger, Ph.D., Ph.D.[a,b,c]

[a] Dept. of Radiology, Brigham and Women's Hospital Boston, Harvard Medical School, MA, USA, [b] Dept. of Mathematics and Computer Science, University of Marburg, Marburg, Germany, [c] Dept. of Neurosurgery, University of Marburg, Marburg, Germany

Purpose – The current development of the population's structure leads to a growing part of older patients with a more frequent insistence for surgical treatment like lumbar spinal stenosis (LS), which is the most common cause of spinal surgery in individuals older than 65 years of age [1]. For the assessment of spinal structures such as nerve roots, intervertebral discs and ligamentary constitution, Magnetic Resonance Imaging (MRI)-imaging is in general suitable. However, certain changes of the vertebra due to osteoporosis, fractures or osteophytes, require an evaluation of the bone structures via Computed Tomography (CT)-scans, which include radiation exposure [2]. In this contribution, we want to illustrate the capability of MRI-segmentation to reconstruct the vertebral body without x-ray examination, leading to less pre-operative examinations and therefore affecting radiation exposure costs and time-management.

Methods – The presented approach is an extension from our recent articles [3, 4] to a third dimension and it starts by setting up a directed 3D graph from a user-defined seed point that is located inside the vertebra. To set up the graph, the method samples points along rays, which are distributed on a cube's surface. The sampled points are the nodes $n \epsilon V$ of the graph $G(V,E)$ and $e \epsilon E$ is a corresponding set of edges. Besides, there are (inter-) edges between the nodes and there are edges that connect the nodes to a source s and a sink t. An additional delta value determines the construction of the xy-edges and therefore the smoothness of the segmentation results, like shown in the image on the right side. After the graph has been generated, the minimal cost closed set on the graph is calculated via a polynomial time s-t-cut [5], creating the 3D segmentation of the vertebra.

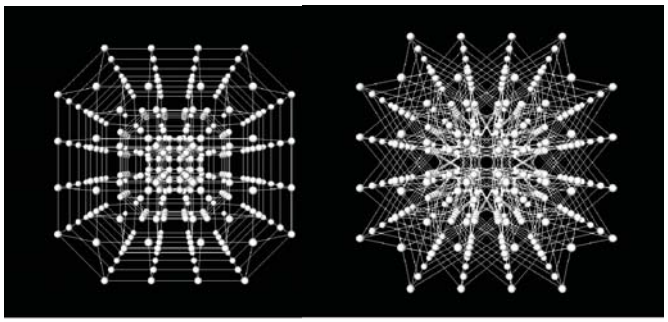

Results – For testing the presented segmentation algorithm we used a C++ implementation within the medical prototyping platform *MeVisLab* (http://www.mevislab.de). The overall segmentation – sending rays, graph construction and *mincut* computation – in our implementation took about twenty seconds on an Intel 2.1 GHz CPU, 4 GB RAM, Windows 7 Home Premium, x64 Version, SP 1. The image on the right side shows a 3D graph that has been constructed around a vertebra inside an MRI dataset (white, with a delta value of zero). Thereby, the center of the graph is located at a user-defined seed point inside the vertebra. The zoomed view in the upper right corner of the figure shows the segmentation result of a vertebra as a triangulated surface (red) and the zoomed view in the lower left corner shows the segmentation result on a sagittal slice (red).

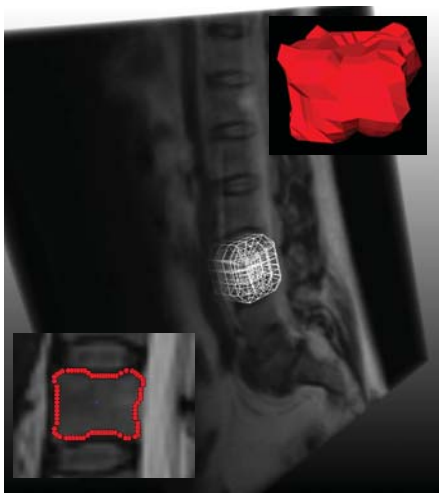

Conclusions – In this contribution, we presented the initial results for a novel 3D vertebra segmentation method. The method is an enhancement of an algorithm we recently developed in a previous work from 2D to 3D. Thus, it is now possible to calculate the volume of a vertebra instead of the area. For vertebra segmentation, the 2D scheme was enhanced, by creating a directed 3D graph within a cubic-shaped template. Thus, the center of the cubic template was user-defined and located inside the vertebra. Then, the minimal cost closed set on the graph has been computed via a polynomial time *s-t-cut*, creating an optimal segmentation of the vertebra's boundary and volume.

Acknowledgements

The authors would like to thank the physician Thomas Dukatz for participating in this study. Moreover, the authors would like to thank Fraunhofer MeVis in Bremen, Germany, for their collaboration and especially Horst K. Hahn for his support. This work is supported by NIH 8P41EB015898-08. Its contents are solely the responsibility of the authors and do not necessarily represent the official views of the NIH.

References

[1] A.F. Joaquim, et al. Degenerative lumbar stenosis: update. Arq Neuropsiquiatr 67(2B): 553-8, 2009.
[2] P.J. Richards, et al. Spine computed tomography doses and cancer induction. Spine (Phila Pa 1976) 35(4): 430-3, 2010.
[3] J. Egger, T. Kapur, T. Dukatz, M. Kolodziej, D. Zukic, B. Freisleben, and C. Nimsky. Square-Cut: A Segmentation Algorithm on the Basis of a Rectangle Shape. In: PLoS ONE, 2012.
[4] J. Egger, B. Freisleben, C. Nimsky, and T. Kapur. Template-Cut: A Pattern-Based Segmentation Paradigm. In: Nature - Scientific Reports, Nature Publishing Group (NPG), 2(420), 2012.
[5] Y. Boykov and V. Kolmogorov. An Experimental Comparison of Min-Cut/Max-Flow Algorithms for Energy Minimization in Vision. IEEE Transactions on Pattern Analysis and Machine Intelligence, 26(9), pp. 1124-1137, 2004.

Segmentation of Pelvic Structures for Gynecologic Brachytherapy

Jan Egger, Ph.D., Ph.D.[a], Neha Agrawal, M.D.[a], Tyler Blevins [a,b], Nabgha Farhat [a,c], Guillaume Pernelle [a], Xiaojun Chen, Ph.D.[a], Yi Gao, Ph.D.[a], William Wells, Ph.D.[a], Tobias Penzkofer, M.D.[a], Tina Kapur, Ph.D.[a**] and Akila Viswanathan, M.D., M.P.H.[a**]

[a] Brigham and Women's Hospital, [b] University of Massachusetts, Amherst, [c] Rutgers University, **Joint Senior Authorship

Purpose – Gynecological cancers, which consist of cervical, endometrial, and vaginal/vulvar cancers, remain the 4th largest cause of death in women in the US since 2010, with reports of 88,750 (5.6% increase) new cases and 29,520 deaths per year in 2012 (6.5% increase) [1]. The standard treatment protocol for these malignancies consists of concurrent chemotherapy and external beam radiation directly followed by brachytherapy. Contouring the cancerous tissue, as well as adjacent organs at risk (OAR), is a routine clinical step. In this contribution, we report on the results of semi-automatic contouring of tumor, the bladder, and the rectosigmoid using the free and open source software package *3D Slicer* (http://www.slicer.org).

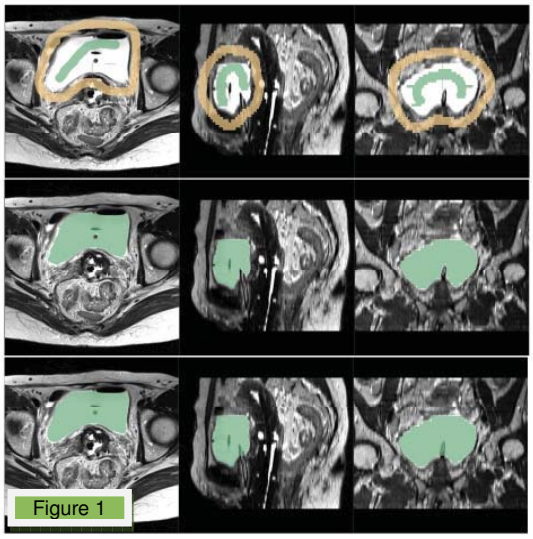

Figure 1

Methods – In this study we used six T2-weighted magnetic resonance imaging (MRI) datasets from a Siemens 3T scanner. A physician carefully manually segmented the tumor, the bladder, and the rectosigmoid in each dataset for reference. We used the *GrowCut* [2] algorithm in *3D Slicer* [3] which is an interactive segmentation algorithm based on the idea of cellular automata to segment each of the structures. In each case, the initialization of *GrowCut* was performed on sagittal, axial, and coronal cross-sections. In this initialization step, parts of the structure to be segmented and parts of the background are marked on the image with the Slicer brush tool (a typical initialization for a bladder is shown in three upper images of Figure 1). The algorithm then automatically computed the contours for the structure.

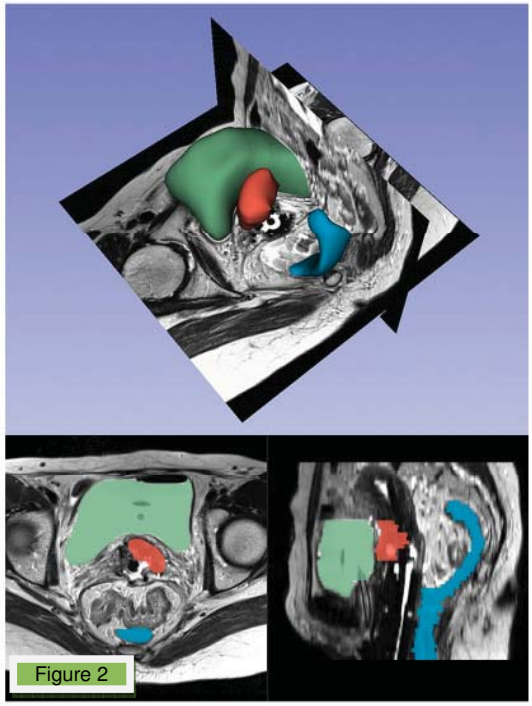

Figure 2

Results – Segmentation of the bladder was successfully performed in all cases, with a Dice Score of 91.94±5.4 compared to expert manual segmentation (second row of Figure 1 shows *GrowCut*, and third row shows manual refinement segmentation). However, *GrowCut* was not able to achieve satisfactory segmentation results for the tumor and the rectosigmoid. Figure 2 shows the results of *GrowCut* segmentation of the bladder rendered together with the tumor and sigmoid from manual segmentation. This is attributable to the heterogeneity in appearance of these structures.

Conclusions – In this contribution, we studied the segmentation of pelvic structures to support the process of automated contouring for gynecologic brachytherapy. Contouring of the bladder was achieved accurately using the *GrowCut* algorithm in *3D Slicer*. However, manual contouring was needed to achieve segmentation results for the tumor and the rectosigmoid. Future work will include the application of additional methods from the literature for these structures [4, 5].

Acknowledgements

This work was supported by NIH grants R03EB013792, P41EB015898, U54EB005149, and members of the AMIGO and Slicer communities.

References

[1] American Cancer Society, *Cancer Statistics 2012*. http://www.cancer.org/acs/groups/content/@epidemiologysurveilance/documents/document/acspc-031941.pdf (accessed July 28, 2012)

[2] V. Vezhnevets & V. Konouchine, GrowCut - Interactive multi-label N-D image segmentation, in Proc. Graphicon, 2005. pp. 150-156.

[3] GrowCut-Module under 3DSlicer http://www.slicer.org/slicerWiki/index.php/Modules:GrowCutSegmentation-Documentation-3.6

[4] J. Egger, et al., Manual Refinement System for Graph-Based Segmentation Results in the Medical Domain, Journal of Medical Systems, Springer Press, Aug. 2011.

[5] J. Egger, B. Freisleben, C. Nimsky & T. Kapur, Template-Cut: A Pattern-Based Segmentation Paradigm, Nature - Scientific Reports, Nature Publishing Group (NPG), 2(420), 2012.

Linear Dynamic System Analysis for Segmenting Breast Carcinomas from DCE-MRI

Jagadeesan Jayender[1,2], Eva Gombos[1,2], Tyler Blevins[1,3], Sona Chikarmane[1,2],
Neha Agrawal[1], Ferenc A. Jolesz[1,2]
[1]Surgical Planning Laboratory, Department of Radiology, Brigham and Women's Hospital,
[2]Harvard Medical School, Boston, MA 02115, USA
[3]University of Massachusetts, Amherst, MA 01003, USA

Purpose: Conventional black-box methods and pharmacokinetic analysis depend on many factors such as MR technique, physiology, arterial input function and tracer delays leading to inaccurate tumor maps. Here, we propose a novel algorithm (abbreviated as LDSTS) to model the time series of a voxel in DCE-MRI using a linear dynamic system and classify the voxel into tumor or healthy class.

Methods: The time-intensity curve of each voxel in the DCE-MRI is modeled using a Linear Dynamic System, as given by equation (1). The state matrix **A** and the output matrix **C** are computed using Kalman filters in the presence of system noise ξ_n and process noise η_n, which are assumed to be white with zero mean. The system is assumed to be a second order system, resulting in a 2x1 **C** matrix, which is used as a feature vector to distinguish between the healthy and tumor voxels in DCE-MRI. The feature vectors are further classified into two groups using a simple k-means clustering algorithm. A color map proportional to the intensity of the difference image over the four time points is computed and overlaid on the priors generated from the k-means algorithm. Twenty two breast examinations of women diagnosed with Invasive Ductal Carcinoma were analyzed. For each breast examination, an expert radiologist delineated the primary area (mass or non-mass like enhancement) of the index tumor and satellite areas using the pre- and first post-contrast DCE-MRI overlaid with each other. A visual inspection of brightly enhanced portions of the DCE-MRI was utilized for delineating the tumor boundaries. In addition, for each case the output of the commercial tumor map, CADstream, was also obtained. The radiologist's segmentation and CADstream output were compared to the output of proposed tumor segmentation algorithm. The accuracy and sensitivity of detecting a biopsy proven lesion was computed, in addition to the Dice Similarity Coefficient (DSC), which measures the amount of overlap.

$$z_{n+1} = Az_n + \xi_n$$
$$x_n = Cz_n + \eta_n \quad (1)$$

Results. The sensitivity of detecting the tumor foci delineated by the expert radiologist by the LDSTS algorithm is 100%. In 2 cases, an additional focus of tumor was also detected, resulting in an accuracy of 88%. The type of enhancement in the additional mass was compared to enhancement in the primary mass and a known normal parenchyma region. The enhancement of the additional mass more closely resembled the enhancement of the primary mass than normal parenchyma, thereby implying that the secondary mass is more likely to correspond to tumor than normal parenchyma tissue. The DSC was measured to be 0.76, thereby showing a good correlation between the LDSTS detected tumor region and the manually segmented region. The LDSTS result was also compared to the tumor maps generated from CADstream, a commercially available software. The results for comparison with the CADstream output were: Sensitivity = 100%, Accuracy = 87.5, DSC = 0.71. The CADstream output was also compared to the radiologist's segmentation. The results were as follows: Accuracy = 85.1%, Sensitivity = 85.1%, DSC = 0.72. The results show that the LDSTS algorithm performs better than the CADstream software in delineating biopsy proven IDCs.

Conclusion. In this preliminary study, the LDSTS algorithm appears to demonstrate higher accuracy and sensitivity in segmenting breast carcinomas from DCE-MRI compared to commercially available software, CADstream.

Acknowledgements: P41EB015898, P41RR019703, BRREF

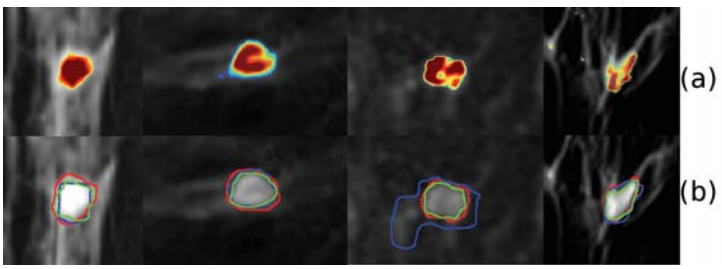

Figure 1. Results of the LDSTS algorithm for four cases, each column is a case. (a) Output of LDSTS algorithm (b) Magnified view of the smoothened tumor outlines defined by LDSTS map (green), Radiologist (red) and Commercial tumor map (blue).

Optimal Trajectory Selection for Segmenting Breast Carcinomas from DCE-MRI using A Statistical Learning Algorithm

Jagadeesan Jayender[1,2], Vivek Narayan[1,3], Sona Chikarmane[1,2], Kirby Vosburgh[1,2], Ferenc A. Jolesz[1,2], Eva Gombos[1,2]

[1]Surgical Planning Laboratory, Department of Radiology, Brigham and Women's Hospital,
[2]Harvard Medical School, Boston, MA 02115, USA
[3]Rensselaer Polytechnic Institute, Troy, NY 12180, USA

Purpose: Segmenting regions of high angiogenic activity co rresponding to malignant tumors from DCE-MRI is a time-consuming task requiring processing of data in 4 dimensions. A segmentation algorithm (SLATS) based on Discrete Hidden Markov Model (dHMM) has been developed to auto-segment breast carcinomas from DCE-MRI without requiring a model. In this abstract, we have trained the dHMMs to learn four trajectories corresponding to the time-intensity curves, derivative (velocity) and second derivative (acceleration) of the time-intensity curves and a composite tuple consisting of the concatenation of the position, velocity and acceleration tuples. We compare the performance of the SLATS algorithm trained for the four observation tuples.

Methods: Our algorithm is based on modeling the observation tuple of each voxel in time and classifying the voxel into healthy and tumor classes. The voxels are approximately clustered based on the magnitude of the FFT into "tissue type" classes using the fuzzy c-means clustering algorithm. A small sample of points from the two classes of voxels is then provided to train two discrete dHMMs corresponding to healthy ($dHMM_1$) and tumor ($dHMM_2$) classes. The ratio of the probability of observing the discrete sequence from $dHMM_1$ and $dHMM_2$ is computed and overlaid with the DCE-MRI as a scalar map to determine the extent of the tumor. The tumor maps generated from the intensity, velocity, acceleration and composite tuples were compared with the delineation of an expert radiologist and the output of a commercial tumor map, CADstream. Twenty-two breast examinations of women diagnosed with Invasive Ductal Cancer and nineteen examinations with Ductal Carcinoma In Situ were analyzed. For each breast examination, an expert radiologist delineated the primary area (mass or non-mass like enhancement) of the index tumor and satellite areas using the pre- and first post contrast images. In addition, for each breast exam we also obtained the output of a commercial software, CADstream and registered the image to the DCE-MRI in 3D Slicer. The result of the SLATS algorithm was quantified in terms of the accuracy and sensitivity of detecting biopsy proven tumors and the overlap in terms of Dice Similarity Coefficient (DSC).

Results: The results of the tum or maps compared to the radiologist's segmentation and CADstream for the ID C cases are shown in Table 1 and 2 and for the DCIS cases in Table 3 and 4 respectively.

	Intensity	Velocity	Acceleration	Composite
Accuracy	85.1%	88.9%	88.4%	92.6%
Sensitivity	92%	96%	92%	100%
DSC	0.63	0.75	0.71	0.72

Table 1. Results of the SLATS compared to rad delineation for IDC cas es

	Intensity	Velocity	Acceleration	Composite
Accuracy	96%	92.3%	92%	88.8%
Sensitivity	100%	100% 95.8%		100%
DSC	0.59	0.71 0.72		0.68

Table 2. Results of the SLATS compared to CADstream output for IDC cases

	Intensity	Velocity	Acceleration	Composite
Accuracy	67.6%	79.3%	68.7%	62.1%
Sensitivity	100%	100%	95.6%	100%
DSC	0.58	0.69	0.56	0.60

Table 3. Results of the SLATS compared to rad delineation for DCIS cases

	Intensity	Velocity	Acceleration	Composite
Accuracy	76%	90.4%	75%	70.3%
Sensitivity	100%	100% 94.7%		100%
DSC	0.44	0.58 0.58		0.49

Table 4. Results of the SLATS compared to CADstream output for DCIS cases

The SLATS algorithm trained for the velo city tuple shows the best perform ance compared to the other observation tuples in terms of the accuracy and sensitivity of detec ting biopsy proven tum ors and the am ount of overlap w ith the radiologist's delineation and CADstream output.

Conclusion: In this prelim inary study, the SLATS algorithm, a model free algorithm, appears to dem onstrate high accuracy and sensitivity in segm enting breast carcinom as from DCE-MRI. The SLATS algorithm trained for the velocity tuple shows the best performance compared to the other observation tuples.

Acknowledgements: P41EB015898, P41RR019703, BRREF

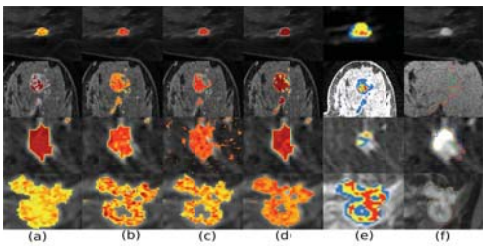

Figure 1. Results of the SLATS algorithm for four cases, each row is a case. (a) Position (b) Velocity (c) Acceleration (d) Composite tuples (e) Commercial tumor map result (f) Magnified view of the smoothened tumor outlines defined by velocity SLATS map (green), Radiologist (red) and Commercial tumor map (blue).

Needle Labeling for Interstitial Gynecological Brachytherapy

Yi Gao[1], Nabgha Farhat[1], Neha Agrawal[1], Guillaume Pernelle[1], Xiaojun Chen[1], Jan Egger[1], Tyler Blevins[1], Sylvain Bouix[1], Allen Tannenbaum[2], William Wells[1], Ron Kikinis[1], Ehud Schmidt[1], Akila Viswanathan[1**] and Tina Kapur[1**]
[1]Brigham and Women's Hospital, [2]Boston University, **Joint Senior Authorship

Purpose – During the process of needle insertion for interstitial gynecologic brachytherapy, the needles may bend secondary to tissue deflection. Variability in tissue resistance may arise from fat, water, bone or muscle coursed through in the path of the needle. In this work we provide a fast and accurate method to extract and display needles from MR images acquired during MR-guided gynecological cancer brachytherapy. Compared to CT, needle artifacts are less easily identifiable in T2w MR, the sequence of choice for visualizing gynecologic cancer. In previous work [1], we introduced the use of a customized SSFP MR sequence to enhance needle artifacts in these procedures, and in this work we provide a post-processing method that reliably and accurately extracts the needles from images acquired using these SSFP MR images.

Methods – The user is asked to provide two pieces of information in order to initiate the needle extraction tool. First, the user is asked to draw a region in one of the transverse slices where all the needles pass through. For example, when a Syed Neblett template is used and is visible in the scan, this region can be the approximate outer boundary of the template. Then, the user is asked to scroll to a superior transverse slice close to the tip of the needles, and identify the cross sections of the needles. The algorithm then takes over to extract the needles in the image. Mathematically, we denote the MR image as a function $I:\Omega\rightarrow R$ where Ω is the field of the view of the image. Accordingly, denote the voxel positions drawn by user for the template as $B = \{b_i \in \Omega;\ i = 1, \ldots, N\}$ and the voxel positions for the needles as $D = \{d_i \in \Omega;\ i = 1, \ldots, M\}$. Then, the Hessian image $H: \Omega\rightarrow S^{3\times3}$ is computed. The eigen system of the 3×3 matrix defines a Conformal Euclidean metric on Ω [2]. A straight line is then computed from each needle label region among $d_{1,\ldots,M}$, to the template region B. By doing this, an optimal line is obtained for each needle, which is regarded as the needle. The algorithm is implemented in C++ language.

Results – This needle extraction tool has been used to segment needles on 6 SSFP MR images. The running time, from user input to final results, is less than one minute to extract up to 20 needles. The figure on the right shows the results of the needle extraction algorithm on three cross-sections (top), and rendered in 3D (below). Results have been visually compared very favorably to manual needle extraction by a physician, and will be quantified in future work.

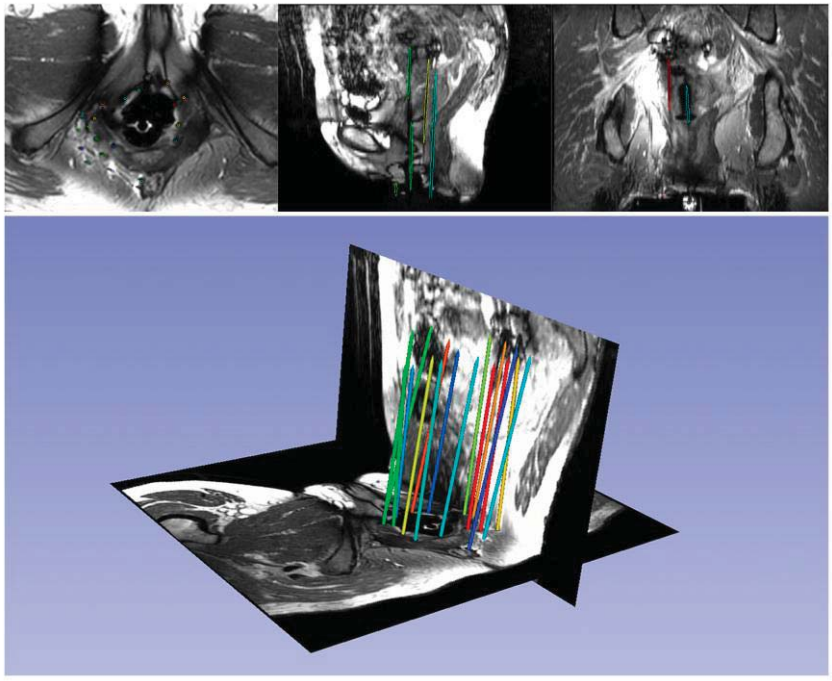

Conclusions – In this work we have a novel algorithm to extract gynecologic brachytherapy needles from SSFP MR imagery. The algorithm requires simple inputs from the user based on which 3D models of the needles are constructed in a time frame that is acceptable for intra-procedural guidance. Future work includes (1) modeling the bending of needles (2) quantitative comparison of results to manual extraction of needles from MR, as well as to CT images.

Acknowledgements
This work was supported by NIH grants R03EB013792, P41EB015898, U54EB005149, and members of the AMIGO and Slicer communities.

References
[1] Kapur, T., Egger, J., Damato, A., Schmidt, E.J. & Viswanathan, A.N., 3-T MR-guided brachytherapy for gynecologic malignancies. Magnetic Resonance Imaging, Elsevier, in Press, 2012.
[2] Kichenassamy, S., *et al.*, Arch. Rational Mechanics and Analysis, 134(3):275–301, 1996.

A Software Prototype for Real-time Ablation Zone Planning Using Distance Transformation Calculated Isosurfaces

Jan Egger, Ph.D., Ph.D.[1,2,3], Tina Kapur, Ph.D.[1], Philipp Bruners, M.D., Ph.D.[4], Tobias Penzkofer, M.D.[1,4]

[1] Dept. of Radiology, Surgical Planning Lab, Brigham and Women's Hospital Boston, MA, USA, [2] Dept. of Mathematics and Computer Science, University of Marburg, Marburg, Germany, [3] Dept. of Neurosurgery, University of Marburg, Marburg, Germany, [4] Dept. of Diagnostic and Interventional Radiology, RWTH Aachen University Hospital, Germany

Purpose – Thermal or electrical ablative techniques are used in a variety of pathologies, such as local tumor control or local pain treatment. Additionally to cryoablation, microwave ablation and radiofrequency ablation, irreversible electroporation (IRE) was recently added to the toolbox of image guided therapy (IGT). For all aforementioned techniques planning and monitoring of the ablation areal is central to the procedure's success [1]. Many published methods include CPU-intensive simulations of ablation techniques [2,3]. We present a method to plan and monitor estimated ablation volumes in real-time.

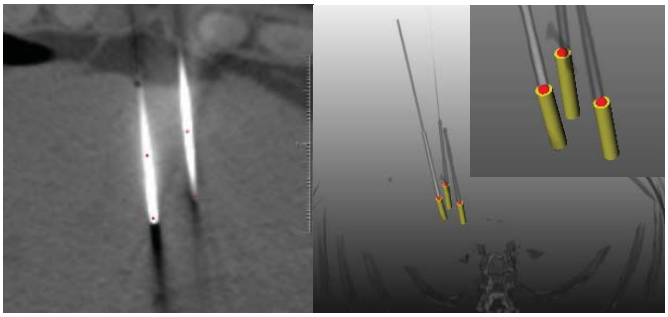

Figure 1. Left: Manually defined seed points at two needle tips. Right: Three cylinders (yellow) generated via six seed points.

Methods – A research software prototype was developed using MeVisLab (http://www.mevislab.de). In a showcase application the electrical field of irreversible electroporation was estimated using Euclidian distance transformations (DTF): a distinct inverse DTF around every manually determined (Figure 1) needle tip was calculated after manually segmenting the needle tips in an intraprocedural CT scan. Subsequently, summation of the distance fields was performed, isosurfaces at three distinct isovalues were calculated (Figure 2) and compared to postprocedural imaging (Figure 3).

Results – The segmentation and isosurface calculation could be performed swiftly with minimal user interaction. A qualitative comparison of the generated isosurfaces with postprocedurally acquired MRI imaging showed reasonable concordance of the predicted and achieved ablation volume in the presented use case of irreversible electroporation (Figure 3).

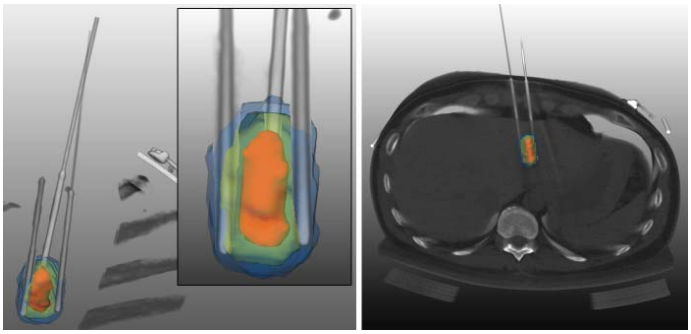

Figure 2. Several isosurfaces around three IRE needles: low energy level (orange), medium energy level (green) and high energy level (blue).

Conclusions – A software prototype was developed for preprocedural planning and intraoperative monitoring of ablative procedures such as IRE. The method needs to be validated against known ablative technologies and parameter sets for different ablation scenarios need to be determined [3,4]. Potential applications of the technique are real-time navigation based ablation volume calculation, real-time monitoring and adjustment of ablation volumes, especially in IRE, cryotherapy and microwave ablation. The value of the more tissue dependent and heat sink prone radiofrequency ablation is however questionable. The easy extensibility towards modified ablation volume calculations could be of further value.

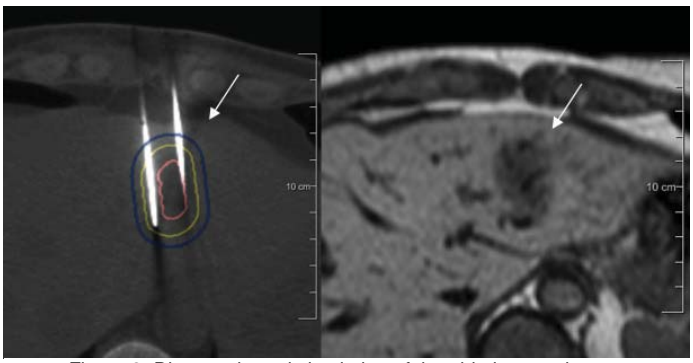

Figure 3. Distance based simulation of the ablation areal on an intraprocedural CT (left) and ablation areal in postprocedure MRI (right).

Acknowledgements

The authors would like to acknowledge Fraunhofer MeVis in Bremen, Germany, for their collaboration and especially Horst K. Hahn for his support. This work was supported by National Institutes of Health (NIH) grant P41EB015898.

References

[1] Y. Zhang, et al. *MR imaging to assess immediate response to irreversible electroporation for targeted ablation of liver tissues: preclinical feasibility studies in a rodent model*. Radiology; 256(2):424-32, 2010.
[2] B. Rubinsky. *Irreversible Electroporation in Medicine*. Technol Cancer Res Treat; 6(4):255-60, 2007.
[3] J.F. Edd & R.V. Davalos. *Mathematical modeling of irreversible electroporation for treatment planning*. Technol Cancer Res Treat; 6(4):275-86, 2007.
[4] K.H. Zou, et al. *Statistical Validation of Image Segmentation Quality Based on a Spatial Overlap Index: Scientific Reports*. Academic Radiology, 11(2), pp. 178-189, 2004.

Title: Subminute nonrigid multimodality image registration for image-guided therapies
Authors: William Plishker[1], Wen Li[2], Nabile Safdar[2], Nobuhiko Hata[3], Raj Shekhar[2]
Affiliations: 1 IGI Technologies, Inc.
2 Sheikh Zayed Institute for Pediatric Surgical Innovation, Children's National Medical Center
3 Brigham and Women's Hospital, Harvard Medical School

Purpose
Image registration is essential to image-guided interventions in which the visualization of the target anatomy as well as navigating interventional devices to it benefits considerably by merging preprocedural images with intraprocedural images. To be clinically practical, it is imperative that image registration be automatic and fast, preferably taking no more than a minute. To be applicable to deformable and moving organs, it is also imperative that the image registration account for nonrigid misalignment. The typically slow speed of automatic nonrigid image registration has thus far prevented its wide-scale clinical adoption.

The recent emergence of powerful graphic processor units (GPUs) presents an opportunity to speed up nonrigid image registration significantly so that it can be applied to interventional procedures. We have implemented single- and multimodality rigid and nonrigid image registration based on maximization of mutual information using the newest GPUs. This implementation was applied to register preprocedural MR images with intraprocedural CT images of patients who underwent percutaneous liver tumor ablation.

Methods
Mutual information-based nonrigid image registration was implemented in two NVIDIA GTX 680 graphic cards installed in a desktop computer (Dell Alienware Aurora R4). The implementation was wrapped as a module of Slicer (version 4.1), open-source software for medical image visualization and processing. The preprocedural MR images were chosen as the floating image to align with the intraprocedural CT (reference) image. After preprocessing (resampling, denoising, and window level rescaling) in the CPU (Intel Core i7-3820@3.60GHz x 8), the images were transferred to the GPUs for registration. The pre- and post-registration images were reviewed using Slicer's visualization tools.

The registration was performed on three clinical MR and CT datasets acquired as part of liver tumor ablation procedures at Brigham and Women's Hospital. Each dataset comprised a contrast-enhanced MR study to diagnose tumors before the procedure and a CT scan for ablation planning in the procedure room. The image and voxel dimensions were different for different cases and no starting alignment information was available for a pair of images to be registered.

Results
The registration took 35–40 seconds, depending on the image dimension. The preprocessing took less than 5 seconds. An experienced radiologist identified corresponding anatomical landmarks on the original MR and CT datasets before registration. Target registration error (TRE), an accuracy metric for image registration, was calculated as the distance between the transformed landmark point on the registered image and the expert identified point on the fixed image. The average TRE for four landmarks and three datasets was 11 mm (~3 voxels). The initial misalignment based on the same landmarks was 71 mm (~21 voxels).

Conclusions
By harnessing the computing power of the most advanced GPUs within Slicer, we were able to perform multimodalilty nonrigid registration of clinical images with acceptable accuracy in less than a minute. In the future, we will test GPU-accelerated registration and the Slicer framework on a larger set of MR-CT images of tumor ablation patients, as well as, other image modality pairs originating from other clinical scenarios. Subminute image registration, rigid or nonrigid, is an enabling technology with potential to add a new level of precision and sophistication to image-guided therapies.

A Novel Iterative Approach for Accounting for Non-Rigid Deformations in Image Guided Liver Surgery Using Sparse Surface Data

D. Caleb Rucker[a], Yifei Wu[a], Thomas S. Pheiffer[a], Amber L. Simpson[a], Michael I. Miga[a,b,c]

[a]Vanderbilt University, Department of Biomedical Engineering, Nashville, TN, USA
[b]Vanderbilt University Medical Center, Department of Radiology & Radiological Sciences, Nashville, TN, USA
[c]Vanderbilt University Medical Center, Department of Neurological Surgery, Nashville, TN, USA

PURPOSE: The translation of image-guided surgery techniques to the abdomen requires accurate registration between the intraoperative physical organ and its preoperative imaged counterpart, and accurate rendering of tool locations in real time. Additionally, it is equally important for the introduced technology to be fast, relatively inexpensive, and to minimally impact surgical workflow. Sparse partial surface measurements such as those provided by a laser range scanner (LRS) are excellent for measuring the surgical field as they are non-contact, very fast, and have minimal impact to workflow when compared to other intraoperative imaging modalities. However, the challenge of extrapolating relevant localization information from distinctly sparse data while balancing the competing goals between workflow and engineering design, and between application and accuracy is challenging. In this work, we present a novel iterative approach to deformation correction for image-guided liver surgery using sparse laser range data.

METHODS: Our proposed iterative non-rigid registration method is based on a nonlinear optimization framework where the objective function is defined by a metric quantifying the fit between the deformed model surface and the intraoperative data. The predicted deformation at each iteration is generated by the solution of a linear elastic finite element model followed by a subsequent rigid body transformation applied to the entire deformed mesh. The set of parameters chosen at each iteration of the algorithm consist of coefficients defining a smooth displacement field which reside on the posterior surface nodes, in addition to six values which define the subsequent rigid body motion. The posterior displacement field is enforced via Dirichlet boundary conditions applied to a linear elastic finite element model of the liver with stress-free conditions on the anterior surface, thus reproducing deformation modes consistent with the typical practice of “packing” support material underneath the liver to stabilize its presentation.

RESULTS: Experimental results with a phantom liver undergoing large deformations demonstrate that this method achieves target registration errors (TRE) with a mean of 4.1 mm in the prediction of a set of 58 locations inside the phantom. The iterative approach also shows a 42% reduction in mean error over the prior non-iterative single-solve method of extrapolating boundary conditions via a surface Laplacian. Figure 1 shows the TRE distribution results comparing the three methods: (1) rigid registration, (2) Laplacian extrapolation, and (3) new posterior surface displacement reconstruction.

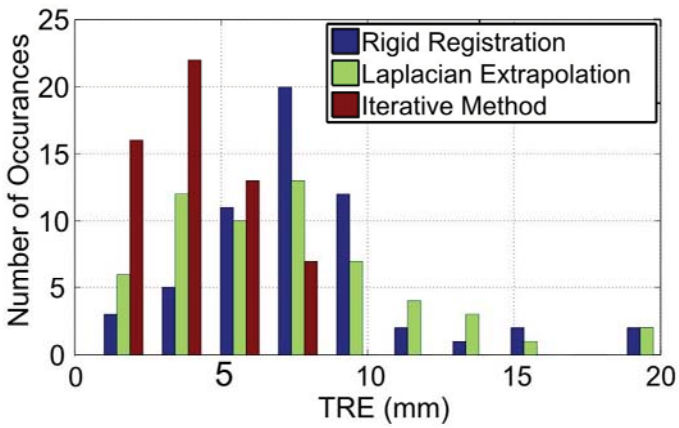

Figure 1. TRE distribution among three methods.

CONCLUSIONS: Careful construction of our phantom experiment was performed to match our experiences under OR conditions. Initial pose rigid registration alignment for our experiment resulted in very similar magnitudes and behaviors of clinically experienced deformation-induced misregistration. The new method dramatically reduced error over a previous realization and is very encouraging for sparse-data driven guidance in the abdomen.

Positive Contrast Ultrashort TE imaging with Ferumoxytol Contrast Agent

Codi Amir Gharagouzloo[1], Saaussan Madi[2], Mukesh Harisinghani[3], Srinvas Sridhar[1]
[1]Nanomedicine S&T Center, Northeastern University, Boston, MA, [2]Bruker BioSpin Corp, Billerica, MA,
[3]Radiology, Massachusetts General Hospital, Boston, MA

Purpose

The purpose of this research is to develop positive contrast imaging techniques exploiting ultrasmall superparamagnetic iron-oxide nanoparticles (USPIONs) as a positive contrast agent (CA). Ferumoxytol is currently the only magnetic USPION nanoplatform that is FDA approved and commercially available, albeit it's approval is for iron deficiency anemia (IDA), and it is therefore an attractive CA for clinical translation. Ferumoxytol is currently being utilized, or has been utilized, in clinical trials with standard T1 and T2 imaging sequences for prostate cancer and gliomas and also in MR angiography[1]. However ultrashort TE (UTE) 3D imaging allows for positive contrast, high SNR and high speed images with TE's in microseconds rather than the typical millisecond regime for negative contrast imaging modalities[2]. In this preliminary work, the utility of Ferumoxytol as a positive CA is tested in nude mice at 4 and 40 hours post injection.

Methods

Ferumoxytol nanopartilces: Ferumoxytol consists of Fe_3O_4 of <10 nm diameter USPIONs that are dextran surface functionalized. They have a long blood circulation half-life of 16 hours. Their hydrodynamic diameter is 26nm. (DLS and TEM data not shown)

UTE 3D imaging: 50x50x80mm FOV images were taken with 195x195x312μm resolution utilizing a 256x256x256 matrix and fat suppression pre-pulses on a Bruker 7T Biospec at the Center for Translational Neuroimaging (CTNI) at Northeastern University.

Experiment: Two nude mice were imaged before and after injection of 150ul of ferumoxytol intravenously via the tail vain. Post injection time-points were 2 and 40 hours, after which time the organs were immediately harvested and frozen at -80°C.

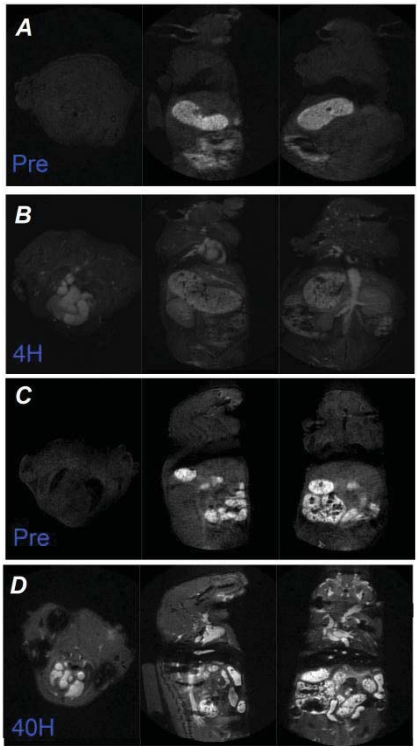

Fig 1. 2D orthogonal images as rendered by Slicer for two nude mice with pre and post contrast injection of 150ul of Ferumoxytol: (A) Pre (B) and 4H post injection; (C) Pre (D) and 40H post injection.

Results

UTE 3D images of nude mice rendered in Slicer: As seen in Figure 1, high SNR (~35) positive contrast imaging elucidates organs and blood vessels in a mouse 4 hours after injection of 150ul of ferumoxytol (Fig. 1B) and intensely brightens organs after uptake and bloodstream clearance at 40H (Fig. 1D). 3D Angiographic type images are shown in Figure 2.

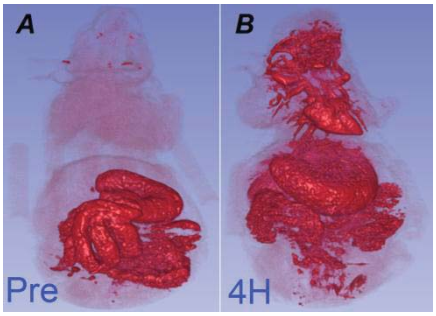

Fig 2. UTE 3D images of a nude mouse pre (A) and (B) 4 hours post injection of 150ul of ferumoxytol rendered with Slicer software.

Conclusions

At an early time-point, clear angiographic information was obtained with UTE 3D imaging and ferumoxytol. Later, high contrast images of organs were obtained for which the probable cause is cellular and macrophage uptake as well as increased contrast due to the clearance of ferumoxytol from the bloodstream. Enhancement may have also been caused by the influence of cellular uptake relaxivity, which has been shown to dramatically change T2 of USPIONs as compared to those in solution[3]. Importantly, unlike other techniques, many pre-contrast regions were completely invisible until addition of CA. Further studies should be completed to explore the uses of ferumoxytol as a positive CA clinically, but preliminary results are promising.

[1] *Ferumoxytol Use as an Intravenous Contrast Agent for Magnetic Resonance Angiography*, Katie L Stabi and Lisa M Bendz, The Annals of Pharmacotherapy, 2011
[2] *Positive contrast imaging with Feraheme - UTE or IRON for clinical application*, Ravi T. Seethamraju et al, WMIC poster, 2011
[3] *Toward absolute quantification of iron oxide nanoparticles as well as cell internalized fraction using multiparametric MRI*, O.M. Girard et al, Contrast Media & Mol. Imaging, 2012

Disclosure of author financial interest or relationships:
We acknowledge partial support from NSF DGE 0965843, HHS/5U54CA151881-02, and the Electronics Materials Research Institute at Northeastern University.

Interactive Real Time Inductively Coupled Catheter Coil Tracking Using a Transmit Array System

Ugur Yilmaz[1,2], Li Pan[3], Ergin Atalar[1,2]

[1]Electrical and Electronics Engineering, Bilkent University, Ankara, Turkey, [2]UMRAM, Bilkent University, Ankara, Turkey, [3]Siemens Corporate Research, Center for Applied Medical Imaging, Baltimore, MD, United States

Purpose: Favorite approach in vascular procedures under MRI is to use active catheters. ICRF (inductively coupled radio frequency) coils; on the other hand, have less RF safety hazards and are easier to be handled since they require no cable connection to MR scanners. In this study, using a transmit array system, we aim to implement a software control on B1 polarization to make real-time interactive ICRF coil tracking possible.

Methods: Anatomic spins are only sensitive to the forward polarization of B1. On the other hand, the polarization of ICRF coil is linear, thus the ICRF coil can also couple to reverse polarized component of B1. Therefore, using reverse and forward polarization modes, one can switch between images with catheter signal only and images that include both catheter and anatomical signal. In order to change the B1 polarization, we used two RF channels of the 8-channel transmit array system on a 3T scanner (MAGNETOM Trio a Tim System, Siemens Healthcare, Erlangen, Germany), connected to the two ports of the body coil. Changing the phase and amplitude of each of the RF channel, the B1 polarization inside the magnet's bore can be altered. Each RF channel is controlled by a corresponding computer, called MPCU, which has a real-time operating system (VXWORKS). Using C socket programming compatible with VXWORKS platform, a server code is implemented and inserted into a work-in-progress tip tracking pulse sequence (BEAT_IRTTT, Siemens Corporate Research, USA). The task of this server is to accept the connection request by the external client software, which we call Interactive RF Polarization Control (IRPC) (Figure 1). The server embedded in sequence manipulates the RF phase and amplitude values according to the received data from IRPC. On the other hand, IRPC (the client software) runs on an external computer that has network connections to the MPCUs. The client software is developed on MATLAB (The MathWorks Inc., Natick, MA).The client software sends connection requests to the desired MPCUs and allows user to change RF phase and amplitude values of each MPCUs via sliders. Interactively changing phase and amplitude values of channels, user sets reverse polarization when real-time acquired images have catheter signal only. Once reverse-polarization mode is achieved, changing to linear and forward polarization is done by checking the forward and linear check-boxes, respectively. Furthermore, once linear polarization is set, the software enables user to uncouple ICRF by letting user sweep the bottom slider, which changes the amplitudes of RF channels in that the direction of linear polarization is changed accordingly.

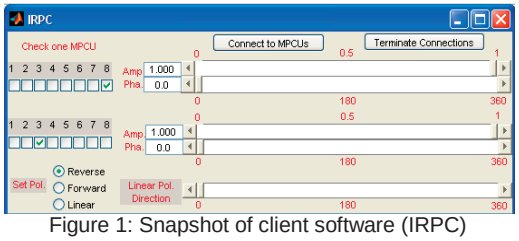

Figure 1: Snapshot of client software (IRPC)

Results: An ICRF coil (10 cm in length) was implemented (tuned to 123 MHz) in a 2.5 mm diameter catheter (Figure 2) and tested inside 2 g/liter copper sulfate solution. Fast GRE mode is selected for the modified sequence. Among all the real-time acquired images, below are the selected three coronal images of the catheter phantom for the following acquisition chains: reverse-polarized, forward polarized and linearly polarized with uncoupled case (Figure 3). The sequence parameters for the conducted experiment were as follows: Fast GRE, FOV: 290x160 mm2, bandwidth: 500 Hz/Px, phase resolution 50%, flip angle: 12 degrees, 5 images/sec.

Figure 2: ICRF Catheter Coil

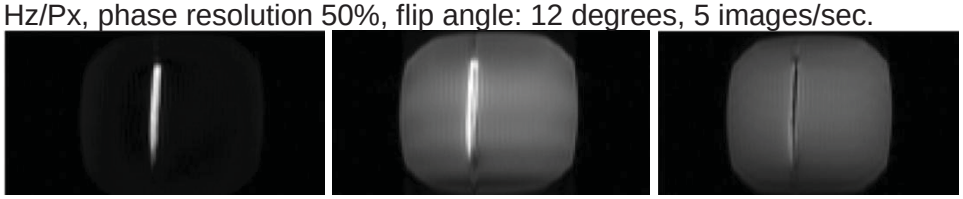

Figure 3: Selected three coronal images of the catheter phantom: reverse mode (left), forward mode (middle), linear uncoupled mode (right)

Conclusions: ICRF catheters are easier to be handled as they have no cable connections to the MR scanner. Therefore, it is important to have real-time interactive control mechanism to track them, and we have shown the possibility of real-time interactive ICRF catheter tracking, based on B1 polarization on the transmit array system. In our interactive control scheme, the user has to sweep the amplitude and phase sliders of each channel until real-time acquired images have strong catheter signals with most possible suppressed anatomic signal at the same time. Nevertheless, our system enables user to switch between the reverse, forward and linear polarization modes very fast (synchronized with image acquisition rate), once reverse polarization is obtained. Moreover, with linear polarization direction sweep, we have achieved interactive real-time ICRF catheter decoupling.

Quantitative Imaging to Establish Distribution Parameters of Timed Release of Drug Eluting Nanoparticles from Implantable Devices for Image Guided Chemobrachytherapy

Rajiv Kumar[1], Stacey Markovic[2], Tej Jadhav[1], Mark Niedre[2], Paul Nguyen[3], Anthony V. D'Amico[3], Mike Makrigiorgos[3], Srinivas Sridhar[1] ,Robert A. Cormack[3]

[1]Department of Physics and [2]Department of Electrical Engineering, Northeastern University

[3]Department of Radiation Oncology, Dana-Farber Cancer Institute and Brigham and Women's Hospital

Introduction: Systemic chemotherapy is often used with radiation therapy in the management of prostate, cervix and lung cancer patients. Advances in radiation therapy have often included image guided procedures and treatment planning to improve the therapeutic ratio. The nascent field of biologic in-situ image guided radiation therapy (BIS-IGRT)[1,2,3,4] offers the potential to deliver planned, localized and sustained delivery of chemotherapy agent, without systemic toxicities, as part of routine minimally invasive image guided radiation therapy procedures. Such image guided chemoradiation therapy requires characterization of the drug distribution produced by implantable drug eluters. This work presents imaging based means to measure temporal and spatial properties of diffusion distributions around spacers coated with dye-loaded nanoparticles.

Methods and Materials: The behavior of ~250nm silica nanoparticles (NP) conjugated to Cyanine 7.5 dye was evaluated with a custom built high-speed near-infrared small animal imaging platform providing 0.1 millimeter spatial resolution with >1Hz image acquisition rate. Samples were trans-illuminated with a pulsed Titanium:Sapphire laser operating at 750 nm and imaged with a high sensitivity, electron multiplied charge coupled device camera (EMCCD). Imaging of agar phantoms was used to compare the diffusion properties of NP to those of free Cyanine 7.5.NP were suspended in a PLGA polymer to create a NP releasing biodegradeable implant in the shape of brachytherapy spacers. A spacer was injected subcutaneously on the left hind flank of a mouse and one was inserted into a xenograft tumor on the opposite flank as part of an approved animal research protocol. The mouse was imaged over 14 days.

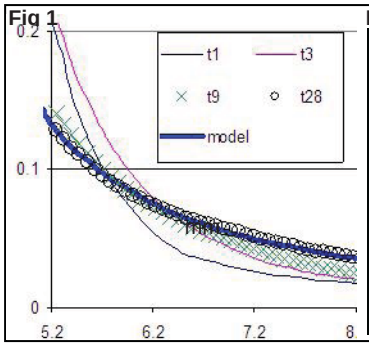

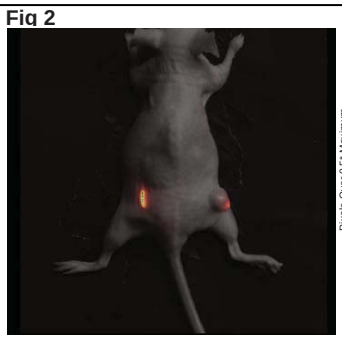

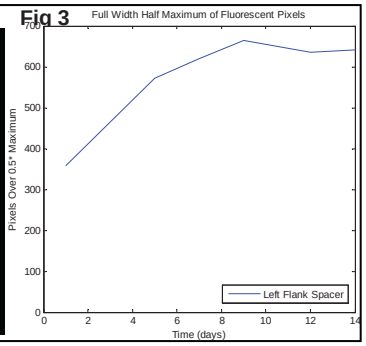

Results: Figure 1 shows NP distribution in agar at multiple time points and a computer fit to one data series. Such curves verify numerical calculations and provide parameterization for chemotherapy treatment planning systems. Figure 2 shows optical imaging of NP releasing spacers implanted in a mouse overlaid with corresponding transmission imaging. The area of high signal increases with time suggesting that NP accumulate in the vicinity of a spacer without diffusing to the rest of the body. Figure 3 shows the time variation of a measure of the region populated by NP. The temporal characteristics of NP accumulation indicate that a BIS-IGRT approach may provide an effective means to improve the therapeutic ratio of brachytherapy.

Conclusion: Quantitative imaging methods can provide the insight necessary to develop an image guided localized sustained chemoradiation therapy approach. Phantom measurements confirm the expected difference in diffusion rates of free dye and NP. These results may validate computational models and establish the computational framework for chemotherapy treatment planning comparable to that seen in brachytherapy treatment planning systems. In-vivo measurements demonstrate that NP remain resident in the vicinity of the implanted eluting spacers with accumulation over times appropriate to improve brachytherapy's therapeutic ratio. Further work is needed to engineer the NP and substrate properties of an implantable spacer to attain the optimal chemotherapy distributions for simultaneous placement during image guided brachytherapy implants.

References:

1) Cormack, R.A., Sridhar, S., Suh, W.W., et al, Biological in situ dose painting for image-guided radiation therapy using drug-loaded implantable devices. Int J Radiat Oncol Biol Phys 76:615-23, 2010.

2) Nagesha, D.K., Tada, D.B., Stambaugh, C.K., et al, Radiosensitizer-eluting nanocoatings on gold fiducials for biological in-situ image-guided radio therapy (BIS-IGRT), Phys Med Biol, 55:6039-52, 2010.

3) Tada, D.B., Singh, S., Nagesha, D., et al, Chitosan film containing poly(D,L-lactic-co-glycolic acid) nanoparticles: a platform for localized dual-drug release. Pharm Res, 27:1738-45, 2010.

4) Cormack, RA, Nguyen P, D'Amico AV, et al, Optimal drug release schedule for in-situ radiosensitization of image guided permanent prostate implants. Proc. SPIE, V.7964, P.79640A Orlando 2011.